Doctoral Dissertation

Christo Rautenbach

An Experimental and
Theoretical Study of
Dense Fluidized Bed
Fluid Dynamics

**Telemark University College**
Faculty of Technology

Christo Rautenbach

An Experimental and Theoretical
Study of Dense Fluidized Bed
Fluid Dynamics

Thesis for the degree of Doctor Philosophiae

Telemark University College
Faculty of Technology

**Telemark University College**

# An Experimental and Theoretical Study of Dense Fluidized Bed Fluid Dynamics

Christo Rautenbach

Thesis submitted to the Telemark University College
for the degree of philosophiae doctor (PhD)

ii

*This is all for and through my God and Savior Jesus the Christ, the Holy Son of the only God, Jehovah-Jireh: The God who provides!*

# Preface

I will first like to acknowledge the help, support and love of my God, Jehovah-Rapha (the Lord our Healer). He has carried me, protected me, guided me and loved me every single day through the course of my studies. He has brought glory to His name and honoured me with life, and life in exceeding abundance! May His name and goodness always be glorified.

I will also like to extend my gratitude to my amazing family for their support and love. They are always there for me and will do anything to help me if I am in need. I truly would not have made this part of my life's journey if it was not for all of you. *Dankie Pa (Fanie), Ma (Susan), Ess-Jee en Ouma (Naomie) vir alles. Die lewe mag dalk party keer 'hard' wees, maar saam met God is ons harder!*

My sincerest gratitude also goes to my supervisor, Prof. Britt. M. Halvorsen. She has guided me with insight and wisdom and has made my studies a very pleasant experience. Through her kindness she has granted me numerous opportunities that few people ever get to experience, like meeting researchers that are leaders in their respective fields. *Takk Britt for alt! Jeg kan skrive bøker av alle de gode du har gjort for meg, men i stedet denne setningen må gjøre.*

Great thank to my co-supervisor, Prof. Morten C. Melaaen, for his very insightful comments and support through all of my studies. I am also pleased to thank Prof. Robert F. Mudde, who granted me the opportunity to use the time-resolved X-ray tomograph located at the Technical University of Delft in the Netherlands.

Last but not least I have to thank all of my friends. It is true that a

person can be known by his friends and with friends like mine I can be proud. Life is all about balance and with my friends this study period was transformed into a growing experience, both mentally and emotionally. *Thank you everyone, I can't name you all because then this thesis will probably double in size! Thank you for all the laughs, adventures, parties and support. You guys are legends and I am honoured to call you my friends.*

# Abstract

The papers presented in the present study aim to elucidate the complex fluid dynamic phenomena in a cold dense phase fluidized bed reactor. Theoretical and experimental studies were conducted with this aim and several advances has been made within the field of fluidization during the course of the present study.

Most of the experiments performed in the present study made use of spherical glass particles of different sizes and size distributions. The glass particles are inert when fluidized with air and thus no chemical nor thermal reactions were simulated or modelled. Three measurement system were employed during the course of the study, a Pressure measurement system (probes and detectors), an Electrical Capacitance Tomography (ECT) system and Time-resolved X-ray tomograph. Both of these tomographs are non-invasive and was used to measure different dynamic properties within fluidized bed reactors.

In the theoretical investigations it was found that a powered addition procedure can be used to correlate the pressure drop in the transition region between a fixed and fluidized bed. The aim of these studies were to quantify and explain the physical meaning of the shifting parameter. The shifting parameter with a value of approximately 15 was found to produce the best correlation with experimental pressure drop data in the transition region between a fixed and fluidized bed. This value was independent of the particle size distribution and particle density. The exact physical meaning is still the subject of ongoing research.

With the tomographic experiments numerous results were obtained. The experimental span of Time-resolved X-ray tomography was found

to influence the outcome of measurements made regarding dynamic parameters. The influence of small particles in a wide particle size distribution was also investigated in various ways. It was found that small particles can generally improve the quality of fluidization but may increase the risk of partial defluidization and segregation. The two tomographic modalities were also compared to allow future studies to make an informed choice when it comes to choosing the appropriate tomograph. In particular the ECT tomograph was found to be adequate for diagnosing the quality of fluidization when making use of various statistical concepts.

Some of the measuring techniques utilised in the present study was finally also used in a study that had direct implication in industrial applications. This industrial application was the gasification of biomass and is an important technology as it can play a role in the fight against global warming. ZrO and plastic particles with a density ratio of 6, were used in the experiments to simulate the bed material and the char-wood particles in a biomass gasifier. The aim of that work was to study the fluidization properties in a cold fluidized bed with different mixtures of particles. The experimental results showed that the minimum fluidization velocities strongly depended on the particle composition in the bed.

In conclusion this study has widened the research communities understanding of fluidized bed reactors by investigating bubble activities and characteristics theoretically and experimentally. The performance of numerous reactors depend on the bubble activity in the dense bed region of a fluidized bed. With the advances made in the present study, the research community has more diagnostic tools and knowledge of non-intrusive measurement systems to understand bubble activity and thus further fluidization technology.

# Contents

# List of Figures

# Nomenclature

Latin letters

| Symbol | Explanation |
|--------|-------------|
| $C_d$ | drag function [-] |
| $d_p$ | particle diameter [m] |
| $F$ | dimensionless drag force [-] |
| $g$ | gravitational acceleration [$m/s^2$] |
| $H_{fb}$ | height of fixed bed [m] |
| $H_{mf}$ | height of bed at minimum fluidization [m] |
| $H_f$ | height of bubbling bed [m] |
| $K$ | permeability [$m^2$] |
| $L$ | distance or length [m] |
| $p_f$ | pressure in the fluidizing fluid [Pa] |
| $P$ | pressure [Pa] |
| $r$ | radial coordinate or distance [m] |
| $R$ | bubble radius [m] |
| $Re$ | Reynolds number [-] |
| $Re_p$ | particle Reynolds number [-] |
| $s$ | shifting-parameter [-] |
| $t$ | time [s] |
| $u_0$ | superficial velocity [m/s] |
| $u_{mb}$ | minimum bubbling velocity [m/s] |
| $u_{mf}$ | minimum fluidization velocity [m/s] |
| $v_g$ | interstitial gas velocity [m/s] |

| **Symbol** | **Explanation** |
|---|---|
| $v_s$ | particle velocity [m/s] |
| $V_{tv}$ | terminal velocity [-] |
| $w$ | weighting factor [-] |

Greek letters

| **Symbol** | **Explanation** |
|---|---|
| $\beta_A$ | Model A gas-solid drag coefficient [kg/m$^3$s] |
| $\varepsilon$ | void fraction [-] |
| $\varepsilon_s$ | solid fraction [-] |
| $\theta$ | inclination angle in spherical coordinates [rad] |
| $\mu_g$ | viscosity [Ns/m$^2$] |
| $\xi$ | dimensionless distance, $r/R$ [-] |
| $\rho_g$ | gas density [kg/m$^3$] |
| $\rho_p$ | particle density [kg/m$^3$] |
| $\phi_s$ | shape factor [-] |

# Part I

# Overview

# Chapter 1

# Introduction

## 1.1 Background

The phenomena of fluidization was described by Kunii and Levenspiel as: "the operation by which solid particles are transformed into a fluidlike state through suspension in a gas or liquid" [1]. With this definition of fluidization it is also clear why the process is called 'fluidization'. The fluidized bed was introduced in the gasification of lignite in as early as the 1920s, and even though the technology started out in the petroleum industry, it is currently being used in a variety of industrial applications [2]. These applications are wide spread from the pharmaceutical industry to the emerging technologies of carbon capture [3].

According to J. R. Grace the world is faced with the need for transformative changes to solve global problems [4]. Most of the greenhouse gases influencing climate change originates from fossil fuels [4]. Fluidized beds can play a role in combating climate change through technologies like Chemical Looping Combustion (CLC), Biomass gasification and resource recovery technologies [4].

Some of the attractive features of fluidized beds are described by Azizpour et al. [5] as the mobility of particles and high heat and mass transfer. Fluidized beds can be operated in a variety of conditions and, depending on the application, the particles used can differ dramatically in

behavioural characteristics when used in a fluidized bed reactor. Thus fluidized beds can exhibit some unwanted behaviour like agglomeration of particles, entrainment of particles, gas bypassing and partial de-fluidization [4]. Knowledge and understanding of fluidized bed fluid dynamics is therefore crucial for operating, designing and furthering fluidization technology. The aim of the present study is to aid in the furthering of fluidized bed technology with both an experimental and theoretical approach.

## 1.2   Objectives

According to Kunii and Levenspiel [1] the most important applications of fluidized beds involves gas-solid fluidized beds [1]. Therefore the present study will only focus on gas-solid fluidized systems under ambient conditions. The present study concentrates on the fluid dynamic behaviour of the gas-solid system without taking chemical or thermal reactions into account. The goal of the study was to gain insight into the complexity of dense phase fluidized beds by means of theoretical and experimental investigations. Such knowledge and measurements are needed as it aids in the monitoring of industrial plant performance, process optimisation and analysis of plant problems [6]. The objectives of the present study can be summarised as:

- predicting the pressure drop as a function of the superficial velocity during regime transition in the fluidization of a fixed bed,

- extending the Buyevich et al. [7] model to obtain the solid fraction distribution around a fluidized bed bubble in two dimensions,

- determine the influence of small particles on bubble size and distribution in a fluidized bed using Electrical Capacitance Tomography (ECT),

- determine the experimental time span required for measuring various dynamic fluidized bed properties using time-resolved X-ray tomography,

- compare ECT and time-resolved X-ray tomography using bubble size and frequency as a metric,

- investigate the use of ECT as fluidization quality diagnostic tool by using statistical methods such as sample skewness and excess kurtosis,

- investigate the diagnosis of bed material size segregation by means of statistical analysis (standard deviation calculations) of ECT data.

## 1.3 Thesis layout

The layout of the present work can be divided into four sections:

1. The theoretical investigation into the physical meaning of the shifting parameter. These investigations utilised various theoretical equations and procedures to elucidate the transition between fixed and fluidized bed. In the studies pressure drop measurements were taken to determine the effect of several parameters on the shifting parameter in the powered addition procedure. These investigations are presented in Paper A and B in Part II of the present study. Chapter 2 also elucidates some theoretical drag model concepts to aid in the understanding of the last mentioned papers.

2. The next section was also theoretical and investigated the solid fraction variation around a bubble rising in a fluidized bed. Paper C in Part II of the present study elaborates on this topic. Increased understanding of the physical phenomena in a fluidized bed is crucial for the modelling, simulation and design of fluidized beds of the future. Simulations were also performed and were used to provide a form of validation of the proposed 2D extended mathematical model.

3. The third section of the present study pertains to experiments. Experiments are needed to validate theoretical models and/or simulations. In this section two state of the art measuring systems

were employed. An Electrical Capacitance Tomography (ECT) and a Time-resolved X-ray tomograph. Both these systems are non-intrusive and allowed 3D investigation of the flow behaviour of the dense phase fluidized beds under consideration. To aid in the visualisation and investigation of the ECT data, a reconstruction program was written in the present study. The program took as input the 2D 'slice' images produced by the ECT tomograph and reconstructed 3D images in such a fashion that the bubble volumes, frequency, shape and location could readily be obtained (refer to Paper D in Part II of the present study). Chapter 3 provides an overview of experimental measuring techniques that can be used in multiphase flow systems related to particles. The reasons why the particular measurement systems used in the present study were chosen is also elaborated in Chapter 3.

The time-resolved X-ray tomography system is a relatively new technology, as first results with such a system was first published by R.F. Mudde in 2010 [8]. As a result the limitations and advantages of the system has not been extensively investigated. Paper E in Part II of the present study investigates the influence of the experimental span of such a system to aid in future usage of such a tomograph.

All measuring systems have advantages and limitations. In Paper F in Part II of the present study the strengths and weaknesses of the two tomographs investigated are summarised to aid future researchers in choosing the right measuring system for their particular application.

In Paper G and H in Part II of the present study the ECT tomograph and some statistical methods are used to diagnose the quality of fluidization. The concepts of Standard deviation, Skewness and Kurtosis are employed with the average solid fraction fluctuations data recorded with the ECT tomograph. These kind of diagnosis techniques aid in the analysis of the complex fluid dynamics in a gas-solid fluidized bed.

4. The final section pertains to industrial applications. All of the theoretical and experimental investigations in academia is ultimately aimed at improving or the better understanding of some real word applications. In Paper I in Part II of the present study the ECT system and pressure measurements were employed to investigate phenomena linked to the gasification of biomass particles. The gasification of biomass is a green technology and is currently the subject of extensive research.

The thesis is thus outlined by the general approach of investigating a problem or phenomena. (i) First by understanding and investigating some theoretical aspects of the phenomena in question (in the case of the present study: Fluidization). (ii) Consider the best measuring technique available for investigating the particular phenomena. (iii) Then acquire some experimental data to quantify and/or diagnose the problem. (v) Then relate the solutions or investigations to the real world or industrial applications to solve problems or optimise operations.

## 1.4 Main contributions

The main contributions of the present study can be summarised as:

- The shifting parameter investigations presented in Paper A and B indicates that the shifting parameter is independent of the particle size distribution and particle density. This knowledge may aid future research in determining the exact physical meaning of the shifting parameter. In these publications a single correlation was also presented for determining the pressure drop in the fluidization of a fixed bed.

- 3D fluidized bed information was measured with two tomographic modalities and is presented in Paper D, E and F. With this information, bubble volume data was used to investigate the influence of small particles on fluidized bed fluid dynamics. It was found that

the small particles in a particle size distribution had the general effect of better quality fluidization. A *MATLAB* program was also developed to reconstruct the obtained 2D ECT data into 3D data.

- The influence of the experimental span on the Time resolved X-ray tomography system was investigated. Three dynamic parameters were investigated: the bubble velocity, bubble frequency and bubble volume. These experiments were performed with both a single central jet and with a porous plate distributor. The contribution of this study, presented in Paper E, will help future researchers in determining an effective experimental span, depending on the dynamic parameter investigated. An effective threshold value was also determined for the data obtained with the Time-resolved X-ray tomography system.

- In Paper G and H statistical diagnoses of fluidized beds were performed using the average solid fraction data obtained with the ECT tomograph. These non-invasive diagnosis techniques aid in better understanding complex fluidized bed dynamics. These techniques were also utilised in investigating the influence of small particles on the overall bed behaviour. Using these methods small particles were also found to improve the quality of fluidization but with the added risk of particle size segregation. Thus using statistical analysis on ECT data proved to be relevant and useful in diagnosing the quality of fluidization.

- In total 9 papers were written during the course of the current PhD study: 3 published journal papers, 3 conference papers and 3 papers submitted to journals that are still in the reviewing process. 5 of these papers were also presented at international conferences.

# Chapter 2

# Theory

Some theoretical aspects of fluidized beds will be discussed in the current chapter to aid in the understanding of the papers that are presented in Part II of the present study.

## 2.1  The fluidized state

Depending on the application either a gas or a liquid can be employed as fluidizing fluid. The behaviour of a fluidized bed can also be mapped into regimes. Some of these regimes are described by Makkawi and Wright [9] as the fixed bed, single bubble, slugging, turbulent and fast fluidization regime. Some of these regimes are schematically depicted in Figure 2.1. The gas or liquid is fed into the fluidized bed through a distributor. Various distributor designs are employed in industry and each distributor has an particular impact on the bubble formation at the bottom of a fluidized bed. Some distributors currently used are the porous plate, perforated plate, nozzel-type tuyere and rotating distributor [1, 10]. In the present study only a porous plate distributor was used in all the experimental endeavours and in Figure 2.1 porous plate distributors are schematically depicted at the bottom of the beds. In Figure 2.1 (a) a fixed bed is illustrated. This is typically the situation when very low fluid flow rate is passed through the bed and the fluid percolates through the voids cre-
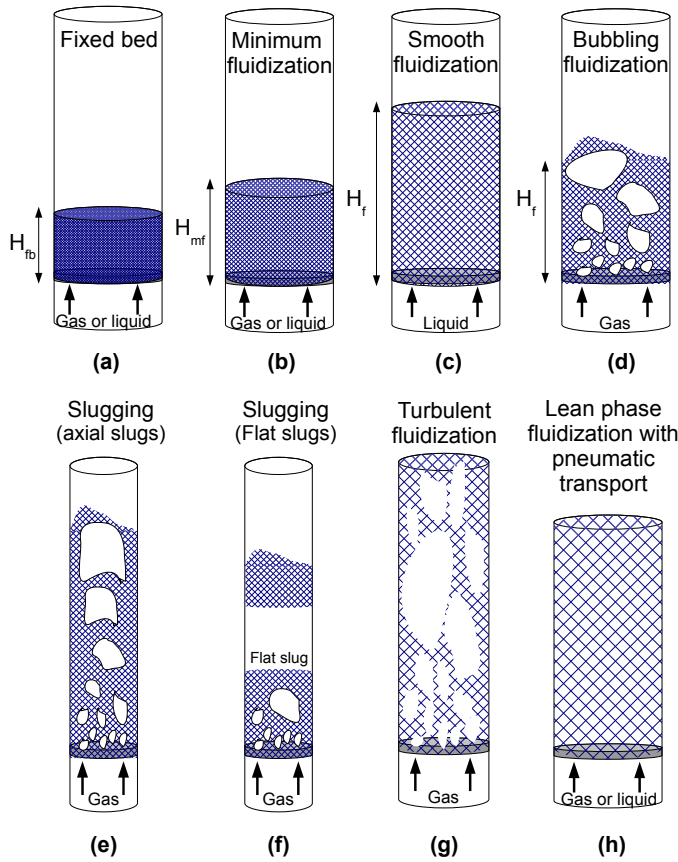
Figure 2.1: Fluidization regimes as depicted by Kunii and Levenspiel [1].

ated by the solid particles. When the superficial velocity is increased the bed can expand to form an expanded bed. At this point the particles have moved apart and some restricted movement and vibrations occur [1]. If the superficial velocity is increased further the upward drag force of the fluid on the particles equals the weight of the particles. If gas-wall drag

and solid stress transmitted by the particles are neglected, the fluidized bed is then said to be at minimum fluidization conditions, as depicted in Figure 2.1 (b) [1, 11].

In Figure 2.1 (c) a smoothly or particulately fluidized bed is illustrated. These beds are usually encountered when working with a liquid as fluidizing fluid [1]. Bed expansion with gas as fluidizing fluid is also typical for Geldart class A particles which are typically small particles. The Geldart classifications will be briefly discussed in Section 2.2 to quantify what is meant with small particles.

When the superficial gas velocity is increased even more a bubbling bed can be observed as depicted in Figure 2.1 (d). The origin of bubbles in a fluidized bed is speculated to be caused by shock waves in the fluidized bed [11]. The shock waves form when porosity waves rise faster than a proposed equilibrium distance [11]. Another explanation was given by Chen et al. [12] who stated that bubbles occur due to instabilities in the state of smooth or homogeneous fluidization. Bubbles provide a means for excess gas to avoid the dense phase and thus reducing instabilities (in the dense phase) to concentrated perturbations (bubbles) [12]. In the 1960s the finding of bubble fluid dynamics in fluidized beds increased the impact of fluidized beds in the chemical engineering sciences [3] and bubbling beds continue to be of great importance due to its mixing capabilities. Generally, small frequent bubbles are desirable as it will cause the gas to move uniformly through the bed while the particles are being distributed well in the fluid stream [13]. In other words, good contact between the fluid and solids. Bubbling beds are not typical for liquid-solid systems but can occur when working with very dense particles and low density liquids [1].

A bed is classified as a dense fluidized bed when the upper limit or surface of the bed is reasonably clearly defined [1].

In Figure 2.1 (e) and (f) two types of slugging beds are presented. A slug is formed in a deep bed that is sufficiently narrow. Usually a bubble is defined as a slug when it occupies more than 50% of the tower diameter [1]. In Figure 2.1 (e) an example is presented where bubbles coalesce to form an axial slug. These slugs are typically formed when working with

smooth fine particles [1]. When the fine particles are rough, wall slugs can form [1]. In Figure 2.1 (f) an example of a flat slug is given. These slugs are typical for large particles. Generally slugging behaviour is viewed to be detrimental to fluidized bed performance but occur commonly in the industry and thus knowledge about this phenomena is needed [12]. Slugging behaviour is not always detrimental and do pose some advantages, such as reduced spread in residence time for both gas and solid phases [12].

When the superficial gas velocity is increased pass the terminal velocity of the particles, the particles are blown out of the bed and the bed surface becomes undefined [1]. Bubbles are replaced by irregularly shaped voids and clusters of particles that move around in turbulent motions [1]. This regime is known as the turbulent fluidization regime and is indicated schematically in Figure 2.1 (g). Due to the high entrainment rates the particles have to be collected and fed back into the bed if steady state operation of the bed is to be achieved [1]. This can be achieved with various forms of cyclones that will feed the particles back into the bed [1].

In Figure 2.1 (h) the superficial gas velocity is increased so far that the particles are blown out of the tower to form the lean or dilute phase. This phase is typically employed as part of a pneumatic transport system where solids are transported with a sufficiently high superficial gas velocity.

## 2.2   Particle classification and properties

Fluidized beds are used in a variety of applications and with the variety of applications comes a variety of particle sizes, shapes, densities and cohesiveness [11]. In an attempt to classify particles that might be used in a fluidized bed reactor, Geldart proposed the diagram presented in Figure 2.2 [14]. This chart is valid for uniformly sized particles that are fluidized with air at ambient conditions [11]. In practise powders consist of particle size distributions, the width of which may vary from broad to narrow distributions. The particle size distribution is very important as it plays an important role in the fluid dynamic behaviour of the fluidized bed (mixing
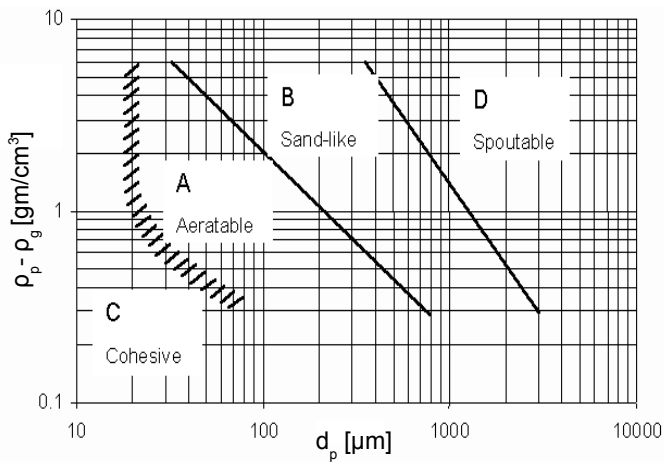
Figure 2.2: Geldart classification of particles. The image is obtained from [14].

and segregation) and influencing the rate of conversion. The gas used in fluidized beds is also not always ambient air and several fluidized beds operate under pressurised conditions [15]. Nevertheless the Geldart chart is still widely used and presents an indication of the behaviour that can be expected for a particular powder. In the case of a powder with a wide particle size distribution, the average particle size can be used along with the average particle density to classify the powder.

The four powder classification groups and their characteristics will be briefly discussed here. The powder classification and expected behaviour play an important role in understanding the rest of the study and will be used throughout most of the papers presented in Part II of the present work.

The particle classifications will be summarised in the following paragraphs based on the description given by Kunii and Levenspiel [1].

***Geldart A particles (Aerated [11]).*** Beds consisting of these particles

are know to expand before bubbles appear.  Thus the minimum fluidiz-
ation velocity ($u_{mf}$) and minimum bubbling velocity ($u_{mb}$) occur at two
distinct superficial velocities, with $u_{mb} > u_{mf}$.  Thus according to the ex-
planation on the origin of bubbles described by Chen, instabilities in the
smooth or homogeneous fluidized state will only occur at superficial ve-
locities higher than minimum fluidization velocity [12].  These powders
are also known to produce a maximum bubble size and is thus character-
ised by the coalesces and splitting of bubbles.  This behaviour was also
observed in the present study when experiments were performed with a
powder bordering the Geldart A particle classification (refer to Paper F).
In small towers these powders can produce axial slugs as described in
Section 2.1.

It should also be noted that small particles help the fluidization qual-
ity (i.e., smaller pressure fluctuations and thus smaller and more fre-
quent bubbles imply better gas-solid contact [16]) by acting as lubric-
ant.  This behaviour was also clearly observed in the experiments per-
formed in Paper F. Kunii and Levenspiel [1] stated that $u_{mb}/u_{mf}$ increases
when the percentage of particles smaller than $45\mu m$ are increased. These
particles are known as fines [16]. Lin and Wey [13] found similar results
and concluded that a wide particle size distribution promotes conversion
and fluidity but increases the likelihood of defluidization and segregation
(refer to Paper D, F, G and H).

***Geldart B particles (Bubbling [11]).***  With this powder $u_{mb}$ and $u_{mf}$
are approximately equal. Thus as soon as the bed is fluidized, bubbles ap-
pear. Therefore Geldart B particles are known to form instabilities in the
homogeneous fluidization state right from the onset of fluidization [12].
The bed expansion is not significant for these powders, given the tower is
operating at ambient conditions [11]. Bubbles tend to start small close to
the distributor and coalesce and grow as they move upward through the
bed. It is interesting to note that bubble sizes, within this powder classi-
fication, is approximately independent of the mean particle size at equal
bed heights [11].

***Geldart C particles (Cohesive [11]).*** These powder are known to be difficult to fluidize and tend to form plugs or rat-holes [11]. The cause for this bad behaviour can be attributed to the interparticle forces (i.e., van der Waals forces [17]) being much greater than the forces exerted by the fluidizing fluid [11].

***Geldart D particles (Granular flow).*** This powder tends to slugging and spouting conditions. Bubbles grow fast and form flat slugs (refer to Section 2.1) while the dense phase is characterised by a high solid fraction. Although these particles are usually not desirable, some industrial application do operate with this particle class. Some examples are agricultural products, the reaction of composite pellets and biomass particles [18].

## 2.3 Drag prediction

Predicting the pressure drop in fluidized beds are important for both industrial applications and for accurate simulations of fluidized bed fluid dynamics. To be able to predict the pressure drop in a fluidized bed, a fluid-solid drag model in required. A trivial way to express this is via the one dimensional model named Model A based on gas momentum balance with a constant cross sectional area, no acceleration, no wall friction and no gravity. Using these assumptions the gas momentum balance is given as

$$ -\varepsilon \frac{\partial P}{\partial x} - \beta_A \left( v_g - v_s \right) = 0, \tag{2.1} $$

where $P$ is the pressure, $\varepsilon$ is the gas volume fraction, $v_g$ the interstitial gas velocity, $v_s$ the particle velocity and $\beta_A$ the Model A gas-solid drag or friction coefficient [11]. Model A indicates that pressure drop in both the gas and solid phase is assumed as oppose to Model B where the pressure drop is only accounted for in the gas phase [11]. Model B is thus obtained when the gas phase pressure drop is subtracted from the mixture

momentum balance [11]. Thus Model B is given by

$$-\frac{\partial P}{\partial x} - \beta_B (v_g - v_s) = 0, \tag{2.2}$$

when the same assumptions as equation (2.1) is assumed. If Model B is used the relation $\beta_B = \beta_A/\varepsilon$ can be utilised [11].

Equation (2.1) is also known as Darcy's law where a drag model has to be employed to determine the drag coefficient $\beta_A$. One of the most well known equations for predicting the pressure drop in a fluidized bed is the Ergun equation and can be expressed as

$$\frac{\Delta P}{\Delta x} = 150\frac{\varepsilon_s^2}{\varepsilon^3}\frac{\mu_g u_0}{(\phi_s d_p)^2} + 1.75\frac{\varepsilon_s \rho_g u_0^2}{\varepsilon^3 \phi_s d_p}, \tag{2.3}$$

with $\varepsilon_s$ the solid volume fraction, $\varepsilon$ the void fraction, $\mu_g$ the gas viscosity, $u_o$ the superficial velocity ($u_o = \varepsilon(v_g - v_s)$), $d_p$ the particle diameter, $\rho_g$ the gas density and $\phi_s$ the sphericity (shape factor) [11, 19]. When equation (2.1) and equation (2.3) are compared it becomes clear that the Ergun equation estimates the drag coefficient as

$$\beta_A = 150\frac{\varepsilon_s^2 \mu_g}{\varepsilon (d_p \phi_s)^2} + 1.75\frac{\rho_g |v_g - v_s| \varepsilon_s}{\phi_s d_p}. \tag{2.4}$$

The Ergun equation is an semi-empirical equation that has been fitted to data collected from air flow through a packed bed of uniform sized particles. According to Syamlal et al. [20] there are two types of experimental data that can be employed to develop a fluid-solid drag model. One method is by using packed bed pressure drop data and the Ergun equation is an example of a correlation developed using this kind of data. Therefore it is logical to assume that the Ergun equation is best suited for fluidized conditions with high solid volume fraction values and Gidaspow [11] recommend that the Ergun equation should be used for $\varepsilon > 0.2$. The other type of data that is used is the terminal velocity data of particles in a fluidized bed [20]. Usually these correlations are expressed as functions of the void fraction and Reynolds number [20]. One example of a drag

correlation derived by using terminal velocity data is given by Syamlal and O'Brien [20] as

$$\frac{\Delta P}{\Delta x} = \frac{3\varepsilon_s \rho_g}{4 d_p V_{tv}^2} C_d \frac{u_0^2}{\varepsilon^2},$$ (2.5)

where $V_{tv}$ is the terminal velocity correlation for the solid phase. These equations can also be used when working with multiple solid phases, usually employed in simulations to approximate a particle size distribution. The terminal velocity correlation can be expressed as

$$V_{tv} = 0.5 \left( A - 0.06\, Re_p + \sqrt{(0.06\, Re_p)^2 + 0.12\, Re_p\, (2B - A) + A^2} \right),$$

where $Re_p$ is the particle Reynolds number of the solid phase [20], expressed as

$$Re_p = \frac{d_p u_0 \rho_g}{\mu_g \varepsilon}.$$ (2.6)

The functions $A$ and $B$ is defined as

$$A = \varepsilon^{4.14},$$ (2.7)

and

$$B = \begin{cases} 0.8\, \varepsilon^{1.28} & \text{if } \varepsilon \leq 0.85 \\ \varepsilon^{2.65} & \text{if } \varepsilon > 0.85. \end{cases}$$ (2.8)

$C_d$ is the drag function of a single sphere. Several expressions exist for correlating $C_d$ and here the expression proposed by Dalla Valle [20] will be employed and is expressed as

$$C_d = \left( 0.63 + \frac{4.8}{\sqrt{\dfrac{Re_p}{V_{tv}}}} \right)^2.$$ (2.9)

By comparing equation (2.1) and equation (2.5) the drag coefficient, $\beta_A$, is given as

$$\beta_A = \frac{3\varepsilon\varepsilon_s \rho_g}{4 d_p V_{tv}^2} C_d \frac{u_0}{\varepsilon},$$ (2.10)

when the Syamlal and O'Brien [20] drag model is employed.

Several drag correlations are presently in use and all of them are attempts to describe the complex momentum transfer between the gas and the particulate phase due to drag. Most of these correlations are empirical or semi-empirical and are thus limited in its applicability in practical applications due to the experimental circumstances used to calibrate the correlation. Nevertheless these correlations have been used with varying success in the simulation and modelling of fluidized bed behaviour.

In the present study three drag correlations were used to investigate the shifting-parameter (as described by Churchill and Usagi [21]) and its apparent usefulness to produce a single equation correlating pressure drop in the fluidization of a fixed bed. The three correlations are the Ergun equation (equation (2.3)), the Syamlal and O'Brien equation (equation (2.5)) and the extended Hill-Koch-Ladd drag correlation [22]. The shifting parameter can be varied in a powered addition procedure to provide an empirical equation for and between limiting correlations or asymptotic solutions. The Ergun equation (equation (2.3)) is actually an example of the powered addition procedure. The first term in the Ergun equation models the laminar flow regime (Darcy regime, $Re \rightarrow 0$) while the second term models the inertial flow regime (Forchheimer regime, $Re \rightarrow 2000$) [19]. These two regimes form the asymptotic solutions while a shifting parameter value of 1 have empirically been found to be the best value. Another drag model employing the powered addition principle in its derivation, is the Representative Unit Cell (RUC) drag model [19, 23]. For more details on this topic please refer to Paper A and B in Part II of the present study. These papers form part of ongoing research in understanding the physical meaning of the shifting-parameter and thus widening our understanding of fluidized bed fluid dynamics.

For completeness the extended Hill-Koch-Ladd drag correlation will also be summarised in the present study. It is applicable to a full range of void fractions and Reynolds numbers and is formed by blending the Hill-Koch-Ladd drag correlation with known limiting forms of the gas-solid drag function [22]. This correlation is based on numerical-experimental data as the Lattice-Boltzmann Method (using first principle calculations),

and was used in the original Hill-Koch-Ladd correlation to determine the drag exerted on a number of randomly dispersed, fixed particles [22]. The friction coefficient, $\beta_A$, used for the extended Hill-Koch-Ladd drag correlation is given by

$$\beta_A = 18 \, \mu_g \varepsilon^2 \varepsilon_s \frac{F}{d_p}, \tag{2.11}$$

where $F$ is the dimensionless drag force [22]. Depending on the operational conditions in the fluidized bed the extended Hill-Koch-Ladd correlation will use different expressions for the dimensionless drag force, $F$. The dimensionless drag force is thus given as

$$F = 1 + 3/8 \, Re \quad \text{if } \varepsilon_s \leq 0.01 \text{ and } Re \leq \frac{F_2 - 1}{3/8 - F_3},$$

$$F = F_0 + F_1 \, Re^2 \quad \text{if } \varepsilon_s > 0.01 \text{ and } Re \leq \frac{F_3 + \sqrt{F_3^2 - 4 \, F_1 (F_0 - F_2)}}{2F_1},$$

$$F = F_2 + F_3 \, Re \quad \text{if} \begin{cases} \varepsilon_s \leq 0.01 \text{ and } Re > \dfrac{F_2 - 1}{3/8 - F_3} \\[2mm] \varepsilon_s > 0.01 \text{ and } Re > \dfrac{F_3 + \sqrt{F_3^2 - 4 \, F_1 (F_0 - F_2)}}{2F_1}, \end{cases}$$

where $Re$ is the Reynolds number defined as

$$Re = \frac{d_p u_0 \rho_g}{\mu_g}.$$

The coefficients of the dimensionless drag force, $F$, is dependent on the solid fraction, $\varepsilon_s$, and is given as

$$F_0 = \begin{cases} (1-w) \left( \dfrac{1 + 3\sqrt{\varepsilon_s/2} + (135/64) \, \varepsilon_s \ln(\varepsilon_s) + 17.14\varepsilon_s}{1 + 0.681\varepsilon_s - 8.48\varepsilon_s^2 + 8.16\varepsilon_s^3} \right) + \\ w \left( 10 \dfrac{\varepsilon_s}{\varepsilon^3} \right) \quad \text{if } 0.01 < \varepsilon_s < 0.4 \\ 10 \dfrac{\varepsilon_s}{\varepsilon^3} \quad \text{if } \varepsilon_s \geq 0.4, \end{cases}$$

$$F_1 = \begin{cases} \sqrt{\dfrac{2}{\varepsilon_s}}/40 & \text{if } 0.01 < \varepsilon_s \leq 0.1 \\ 0.11 + 0.00051 \, e^{(11.6 \, \varepsilon_s)} & \text{if } \varepsilon_s > 0.1, \end{cases}$$

$$F_2 = \begin{cases} (1-w) \left( \dfrac{1 + 3\sqrt{\varepsilon_s/2} + (135/64)\, \varepsilon_s \ln(\varepsilon_s) + 17.89\varepsilon_s}{1 + 0.681\varepsilon_s - 11.03\varepsilon_s^2 + 15.41\varepsilon_s^3} \right) + \\ w \left( 10\dfrac{\varepsilon_s}{\varepsilon^3} \right) & \text{if } \varepsilon_s < 0.4 \\ 10\dfrac{\varepsilon_s}{\varepsilon^3} & \text{if } \varepsilon_s \geq 0.4, \end{cases}$$

$$F_3 = \begin{cases} 0.9351\varepsilon_s + 0.03667 & \text{if } \varepsilon_s < 0.0953 \\ 0.0673 + 0.212\varepsilon_s + 0.0232/\varepsilon^5 & \text{if } \varepsilon_s \geq 0.0953, \end{cases}$$

where $w$ is a weighting factor used to blend the formulas [22] and is given by

$$w = e^{(-10(0.4-\varepsilon_s)/\varepsilon_s)}.$$

For more details regarding this particular model refer to the work done by Benyahia et al. [22].

# Chapter 3

# Measuring techniques overview

In fluidized beds there are various parameters that are of importance to measure. Some of these quantities are the solid volume fraction, solid velocities, solids mass flow, the vertical and horizontal solids distribution, the distribution of the fluidizing gas, e.g. bubbles (related to the quality of fluidization) and temperature concentrations [6]. Because of the variety of parameters that needs to be measured a variety of measuring techniques has been developed. Figure 3.1 will be used to classify these measuring techniques into two main measuring method: Sampling methods and On-line methods. These two groups of methods are ways in which information can be extracted from the two-phase flow system [17]. The following discussion is based on the categorisation and discussion presented by Crowe et al. [17].

*Sampling methods.* These methods are characterised when a number of mechanical samples must be collected from the bulk and analysed. These samples must preferably meet the demands set by the Theory of Sampling (TOS) [24]. Sampling methods can again be subdivided into two categories: *Image analysis* and *Analytic analysis*. Image analysis is typical when a microscope is used while analytic analysis might be using optical methods such as light scattering, light attenuation and diffraction. Mechanical sieving also belongs to this category. For the optical methods
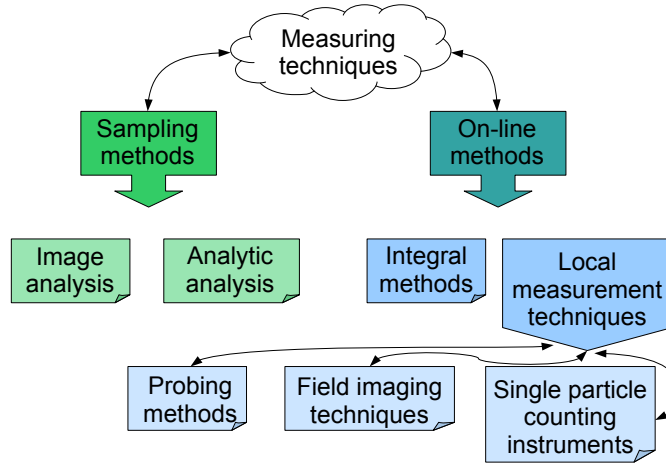
Figure 3.1: Categorisation of measurement techniques that can be used in a two-phase flow system. The categorisation is based on the chart and discussion presented by Crowe et al. [17]

the particles have to be dispersed in either gas or liquid. The result of sampling methods can be summarised as determining the

- characteristic dimensions of particles,

- particle shape factors,

- equivalent particle diameters and

- particle surface area.

*On-line methods.* On-line methods have the added advantage that they are directly applied within the process. On-line methods can again be subdivided into integral methods and local measurement techniques, as illustrated in Figure 3.1.

*Integral methods* are characterised by being time-resolved, spatially averaged properties of an entire cross-section of flow or along a light beam passing through the flow. According to van Ommen and Mudde [25] dense fluidized beds are faced with two major challenges. The first is the high speed at which phenomena change within the system and the second is the opaque nature of the dense bed [25]. Integral methods are some of the measurement systems that can partially overcome both of these major restriction. Examples of integral methods include the tomographs utilised in the present study. Process tomographs are usually fast (fast enough for fluidized bed phenomena, high temporal resolution) and by utilising different types of radiation, electrical fields and current an opaque system can become transparent.

Process tomographic systems and flow meters are also known as cross-correlation techniques because they can determine the transit time of a flowing medium passing sensors located a given distance apart. Thus bubbles can be traced from one sensor to the other and quantities such as the bubble rise velocity can readily be determined. Because Electrical Capacitance Tomography (ECT) and Time-resolved X-ray tomography are cross-correlation techniques and non-intrusive, they were chosen for the experimental investigations in the present study. In Figure 3.2 two measuring planes of the Time-resolved X-ray tomograph are illustrated. This figure is provided to elucidate the cross-correlation concept and to illustrate how bubbles rising in a fluidized bed will pass the two sensing planes. With the X-ray tomography set-up used in the present study, there are three such pairs of measuring planes radiating the fluidized bed simultaneously. In Figure 3.2 only one such pair is illustrated for simplicity. Please refer to Paper E and F for further details. Some other tomographic modalities currently available include Magnetic Resonance Imaging (MRI), Electrical Resistance Tomography (ERT) and $\gamma$-ray transmission tomography.

Light attenuation and laser diffraction can be utilised in system with dilute or disperse flow, but due to the opaque nature of the dense fluidized bed, these techniques can not be used as integral methods in the present study.
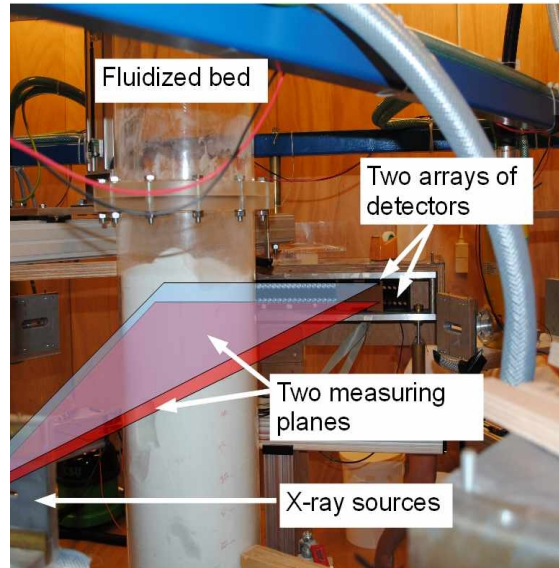
Figure 3.2: Graphical depiction of two measuring planes radiating through an experimental fluidized bed tower.

*Local measurement techniques* are know for high spacial resolution (depending on the method applied). As indicated in Figure 3.1 local measuring techniques can be subdivided into three groups:

- *Probing methods* are known to be intrusive and may thus disturb the process. Probing techniques are also known to be robust and reliable and according to Werther [6], used in routine industrial measurements. Some of the well known probing techniques include isokinetic sampling, pressure probes, heat transfer probes, capacitance probes and optical fiber probes [6, 17, 25]. Optical fiber probes can make use of light attenuation or light reflection and can be used to measure quantities such as bubble velocity in a dense fluidized bed. In dilute or disperse flow it can be employed to measure particle velocity, size and concentration.

- *Field imaging techniques* provides an instantaneous spatial distribution over a finite region. A well know example of this measuring technique is Particle Image Velocimetry (PIV). This method does however require a dilute or dispersed system like most light based techniques.

- *Single particle counting methods* consist of a numerous optical methods like Laser Doppler anemometry (LDA) and phase-Doppler anemometry (PDA). These optical methods can also not be utilised in a dense fluidized bed but there are some other single particle tracing systems that can be used. Positron Emission Particle tracing (PEPT) systems can be employed as such systems work with $\gamma$-rays that can move through a dense fluidized bed [26, 27, 28].

This concludes the overview of measuring systems available for solid-gas two-phase flow. It can be concluded that accurate measurements in a dense fluidized bed is notoriously difficult but due to modern measuring techniques these difficulties are being addressed and partially solved. With an array of measuring techniques available it is important to choose the right measuring system to extract the required data from the process. The constraints and advantages of each measuring system have to be kept in mind before any measurements are made.

In Part II of the study, Papers D, E, F, G, H and I involves some aspect of the cross correlation techniques, ECT and X-ray tomography. These cross-correlation techniques can be classified as integral methods in Figure 3.1. Two thirds of the present study involved measuring systems and even the remaining third of the papers in Part II utilised pressure measurements (classified as probing methods in Figure 3.1). The importance of choosing an adequate measuring system to meet the requirements of the present study is thus clear.

# Chapter 4

# Study overview

In this chapter an overview of the papers presented in Part II of the study is provided. The main concepts and results will be illustrated and for a more in depth study of a particular topic, the reader is advised to refer to the papers presented in Part II. In the present study no scaling has been performed from hot to cold or from pressurised to atmospheric pressure conditions. The present study was not aimed at a particular application and thus no specific scaling could be done. Hot fluidized beds and pressurised fluidized beds can behave significantly different from cold fluidized beds. According to Lin and Wey [13] an increase in temperature has the general effect of increasing the quality of fluidization. Good quality fluidization is expressed as uniformly distributed fluid velocity across the bed [13]. For practical scaling considerations (scaling-up/down) numerous sets of dimensionless number exist in the literature that has to be matched in order to produce the same bed dynamics at different scales [29]. An example of such a set is the given by Glicksman [29] and according to Sierra et al. [29] it is called a full set and is the most extensive set of dimensionless numbers for scaling purposes. A vast number of experimental and numerical studies has been aimed at validating these dimensionless scaling numbers and according to Sierra et al. [29] the major behavioural characteristics, such as the bubbling type, pressure fluctuations amplitude and voidages probability density function, can approximately be scaled even

for large scale-ups/downs. Sierra et al. [29] also mentioned that there
are exceptions where the scaling does not produce reliable results. Usu-
ally the explanation is that additional effects has to be taken into account
such as the interparticle forces [29]. Girimonte and Formisani [30] also
mentioned that thermally induced interparticle forces delay the onset of
steady bubbling conditions in Geldart A particles. Additional dimension-
less numbers can then be defined to address these effects that were not
accounted for in the original scaling models [29].

## 4.1 Theoretical studies

### 4.1.1 Shifting-parameter investigations

In the studies presented in Paper A and B, experiments have been per-
formed in an experimental fluidized bed reactor. The experimental tower
has been equipped with a set of nine pressure sensors located at differ-
ent positions along the height of the tower. The tower has a diameter of
$0.072m$ and a height of $1.5m$. A procedure providing a correlation for data
in the transition region between asymptotic solutions or limiting correla-
tions have been described by Churchill and Usagi [21]. This correlation
can generally be expressed as $y^s\{x\} = y_o^s\{x\} + y_\infty^s\{x\}$, where $y_o\{x\}$ and
$y_\infty\{x\}$ represents the asymptotic solutions for large and small values of the
independent variable $x$ and $s$ is the so called shifting parameter. Changing
the value of $s$ shifts the correlation given by $y\{x\}$ closer to or away from
the asymptotic solutions. This procedure has been proven to give good
correlations in a wide range of applications. The exact physical meaning
of this shifting parameter $s$, is still unknown and Papers A and B is part of
an ongoing investigation into the physical meaning and possible mathem-
atical expression for the shifting parameter. In Paper A the influence of
the particle size distribution was investigated and in Paper B the influence
of the particle density was investigated.

A series of different powders have been used to investigate the influ-
ence of a particular parameter on the shifting parameter, $s$. Up to date no
expression has been stated for this shifting parameter to govern the trans-

ition from fixed to fluidized bed. By keeping all the parameters constant except the investigated variable, the influence of that variable on the shifting parameter could be investigated. Several different drag models were used to serve as a control for investigating the shifting parameter (refer to Section 2.3). The results are given in the form of pressure drop versus superficial velocity data. Experimental data are presented with the drag model correlations and the investigated values of the shifting parameter, *s*. Some of the drag models that were used were the Syamlal O'Brien drag model [20] and the extended Hill-Koch-Ladd drag correlation [22]. The results are evaluated and discussed.

At the point of minimum fluidization the total weight of the packed bed is supported by the upward force created by the gas moving upward through the porous structure. As the superficial velocity is increased from this point the pressure drop remains practically the same [1]. In Paper A and B the pressure drop in the fluidized regime was assumed constant. At this point of equilibrium (minimum fluidization velocity) the pressure-drop is given by

$$\frac{\Delta P}{L} = (1 - \varepsilon)(\rho_p - \rho_f)g, \tag{4.1}$$

with $\rho_p$ the particle density, $\rho_f$ the fluid density and $L = H_{mf}$ the bed height.

In Paper A three different particle size distribution were used: $100 - 200\mu m$, $400 - 600\mu m$ and $750 - 1000\mu m$. All of these powders consisted of spherical glass particles with a approximate density of 2485 $kg/m^3$. In Paper B different percentages of spherical glass particles were mixed with Zirconium Oxide (*ZrO*) to form a particle bed with varying average density. The density of the *ZrO* particles are 3800 $kg/m^3$. In the case of Paper B where the average particle density was varied, the powders had the same approximate particle size distribution. In Figure 4.1 the effect of varying average particle density is illustrated. These powder mixtures where utilised in Paper B and it is clear that a higher average particle density produced a higher pressure drop.

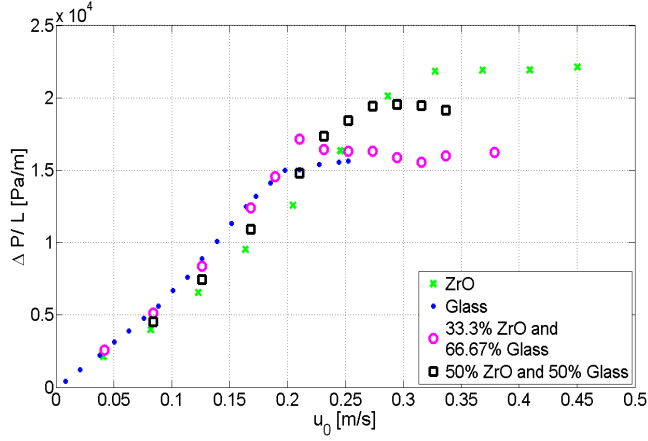Following the procedure described by Churchill and Usagi [21] a total

Figure 4.1: Pressure gradient versus superficial velocity data for several mixtures of glass and *ZrO* particles.

predictive model for the fluidization of a fixed bed can be expressed as

$$\frac{\Delta P}{L} = \left( Drag\ model^{-s} + equation\ (4.1)^{-s} \right)^{-\frac{1}{s}}, \qquad (4.2)$$

were any adequate drag model can be used. The negative powers of $s$ is because the data is a decreasing power of $u_0$.

In Figure 4.2 the effect of changing the shifting parameter is illustrated when employing the Syamlal and O'Brien drag model. A change in the shifting parameter values thus shift correlation (4.2) closer to or away from the two asymptotic solutions.

In both Paper A and B a shifting parameter value of 15 was found to model the transition between fixed and fluidized bed adequately. It can therefore be concluded that the shifting parameter, $s$, is thus not a function of the particle size distribution nor the particle density for the investigated powders of Paper A and B.

The intent of the shifting parameter investigations (Paper A and B) were to describe the transition region between a fixed and fluidized bed. The aim was not to obtain the minimum fluidization velocity but rather to
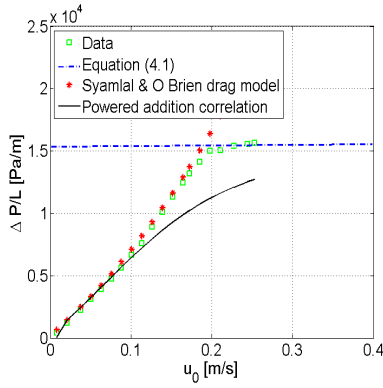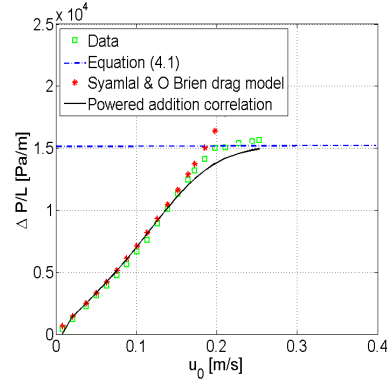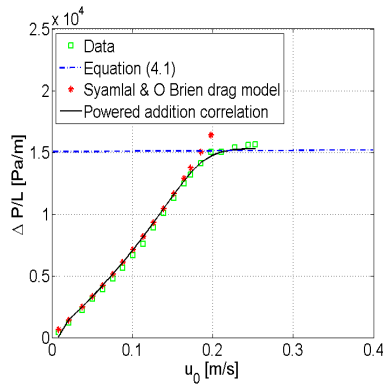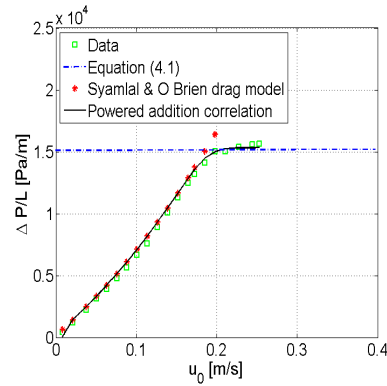
Figure 4.2: The powered addition correlation for a fluidized bed traversing from fixed to fluidized regime with the shifting parameter, *s*, equal to (a) 2, (b) 5, (c) 10 and (d) 15.

produce a single governing equation for the fluidization of a fixed bed that includes accurate prediction of the pressure drop in the transition region.

It is known that the onset of fluidization is gradual for a wide particle

size distribution [1]. The transition between regimes can thus not always be assumed to be abrupt. In the recent work done by Pei et al. [31], experiments were performed with biomass mixtures in a fluidized bed. In particular they performed an experiment with a binary mixture that indicated a clear gradual transition region in the fluidization of the fixed bed [31]. Pei et al. [31] went further to describe this gradual transition in terms of multiple minimum fluidization velocities: the initial fluidization velocity, the minimum fluidization velocity and the full fluidization velocity. Thus the powered addition procedure might be useful in understanding and predicting experimental situations associated with mixtures and wide particle size distributions.

The utility of the produced equation will thus be in predicting the pressure drop anywhere in a fluidized bed, including the transition region of wide particle size distributions. Paper A and B were thus part of investigating the possible parameters that might have an influence on the transition region. From the studies presented in Paper A and B it is thus clear that neither the average particle size nor density had a severe influence on the transition region and that any sufficiently large shifting parameter value will give an adequate solution. In retrospect, much wider particle size distributions must have been investigated to appreciate the possible usefulness of the powered addition procedure in the pressure gradient prediction in the fluidization of a fixed bed.

Equation (5) in Paper A is redundant as only the constant value of the pressure gradient at fluidization conditions are required as the upper limiting condition. This was addressed in Paper B after Paper A has been published.

### 4.1.2   The Buyevich model extension

Bubbles in fluidized beds are one of the major phenomena through which mixing takes place. Better understanding of physical phenomena in and around bubbles in a fluidized bed is important. Knowledge in this regard can help engineers and scientists to design and develop more effective fluidized bed reactors.

In Paper C a model describing the voidage distribution in front and behind a bubble in a fluidized bed was reexamined and extended. The model suggested is not complete or satisfactory. This work is only the initialisation of a research project to model the flow behaviour in and around a bubble in a fluidized bed. This model, originally suggested by Buyevich [7], might be developed into a very useful and convenient predictive tool.
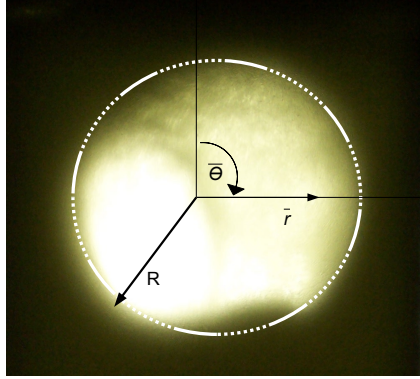


Figure 4.3: Schematic illustration of the proposed model alongside an image of a real fluidized bubble.

In the original work done by Buyevich et al. [7] only the voidage distribution in one dimension was described. Thus only the voidage directly in front of and at the back of the bubble could be predicted. Paper C aimed to use the same basic approach to create a more general model that will be capable of predicting the voidage all around the bubble, in other words, for all values of $r$ and $\theta$ (refer to Figure 4.3). As a starting point of the extended model only two dimensions were considered.

The two dimensional solution was found by solving the total conservation of momentum equation along several different radial lines from the center of the bubble. As an initial control the results were tested with the results published by Buyevich for the voidage along the vertical axis of the bubble [7]. This will be the case with $\theta = 0$.
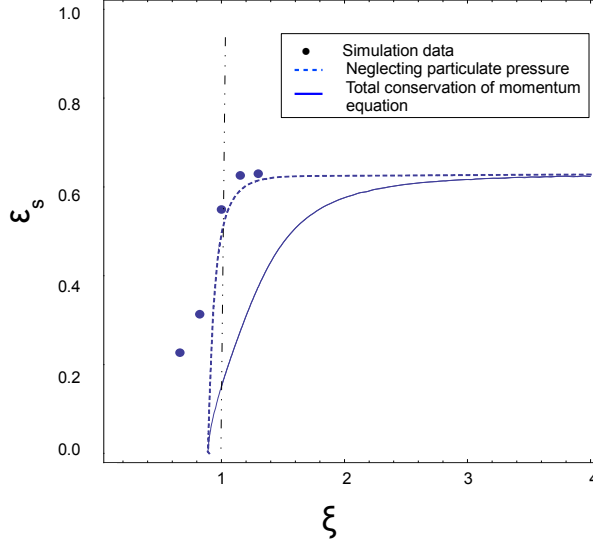
Figure 4.4: Solid fraction distribution along the radial line $\theta = 30^o$.

In an attempt to quantify the results obtained with the model around the bubble, CFD simulations were used to produce data. The simulation data should give some indication of the validity of the model in question. The commercial code *Fluent Ansys 12.1* was used to perform the simulations. The data was extracted at several points along several angles drawn from the estimated center of the bubble at a particular time instance. The comparison between the solid fraction values, $\varepsilon_s$, of the extended 2D model and the simulation data is provided in Figure 4.4 for radial values at $\theta = 30^o$. $\xi$ represents the dimensionless distance and is defined as $\xi = r/R$, with $R$ the bubble radius.

At the present time the extended 2D model gives good results in the area close to the front of the bubble when the particulate pressure is neglected (as illustrated in Figure 4.4). From these results it seems that the current model used to estimate the particulate pressure by Buyevich [32] was not accurate. Buyevich et al. [7] suggested that the particulate pressure is negligible in maintaining the force balance everywhere, with the

possible exemption of a thin boundary layer next to the bubble surface
[7]. This might explain the behaviour observed in Figure 4.4 where the
correlation without the particulate pressure term is in better agreement
with the simulated data. This may be a misleading result as the value
of $\xi$ is strongly connected to what is defined as the bubble boundary. If
the equivalent spherical bubble radius was defined as a smaller value, the
correlation with the particulate pressure term (total conservation of mo-
mentum equation) might have been a better fit. More research is required
with regards to this model and the related particulate pressure prediction
model as suggested by Buyevich et al. [7]. Buyevich et al. [7] stated
that more research is required regarding the particulate pressure and for
future studies more recent publications (such as [33]) might be consulted
for improving the model.

In Paper C the same procedure was followed as that presented in the
work by Buyevich et al. [7] with the exception of solving the conserva-
tion of momentum in the dispersed phase (equation (1) in Paper C) in two
dimensions. Thus all the closure models used was kept in two dimen-
sions, while Buyevich et al. [7] assumed only the radial direction directly
in front and behind the bubble. Thus once all the two dimensional closure
models were inserted into the conservation of momentum in the dispersed
phase, together with all the assumptions, the solid fraction could be ob-
tained for a particular radial distance and polar angle.

In Paper C some unrealistic results were obtained due to the fact that
the solid fraction was predicted as zero. The reason for this result seams
to be because the polar angle direction was left out of the calculation of
the solid fraction. Solving the components of the radial and polar angular
coordinate directions in the conservation of momentum in the dispersed
phase, will both produce values for the solid fraction. When the radial
component becomes zero the polar angular coordinate will obtain a max-
imum and vise versa. Thus by considering both solutions of the solid
fraction, the unrealistic results at a polar coordinate equal to $\pi/2$ can be
avoided.

In Paper C a convective frame of reference, moving with the bubble,
was assumed corresponding to the work done by Buyevich et al. [7].

Buyevich et al. [7] also assumed that the particles were small enough
so that the drag force exerted by the gas will be a linear function of its
relative velocity. This is also known as Darcy's law and can be expressed
as

$$v_r - w_r = -K\frac{\partial p_f}{\partial r}, \tag{4.3}$$

$$v_\theta - w_\theta = -K\frac{\partial p_f}{\partial \theta}, \tag{4.4}$$

in the two dimensional case using polar coordinates [1, 34]. Here $K$ is
known as the permeability constant, $p_f$ is the pressure in the fluidizing
fluid and $v$ in the interstitial velocity. The solid velocities are obtained
from potential flow theory using the velocity potential, as viewed by an
observer moving with the bubble [1]. Using the equations given by Dav-
idson and Harrison [34] describing $p_f$, together with equations (4.4) and
(4.4), expressions for the interstitial velocity of the fluidizing fluid can
be obtained (and thus equation (7)) [34]. To trace the fluid streamlines
a stream function can be used as defined in [1, 34]. The pressure dis-
tribution, $p_f$, was found by satisfying the continuity equation for a in-
compressible fluidizing fluid everywhere around the bubble and also by
satisfying the pressure gradient boundary condition far above and below
the bubble, where the pressure gradient must be constant [34]. This ex-
planation might provide more insightful than the description of a simple
filtration model described by Buyevich et al. [7].

## 4.2   Experimental studies

In the present study 3 experimental techniques were employed: pressure
measurements via pressure probes, Electrical Capacitance Tomography
(ECT) via non-invasive electrodes and Time resolved X-ray tomography
by sending X-ray beams through the fluidised bed. The pressure meas-
urements were mainly employed in the theoretical studies of Paper A, B
and C. These papers were also summarised in Section 4.1. The two tomo-

graphic modalities employed in the present study will be briefly discussed here, together with some main results.

In Figure 4.5 the basic concept of a tomograph and a tomogram is illustrated. Figure 4.5 illustrates a object falling through the measuring
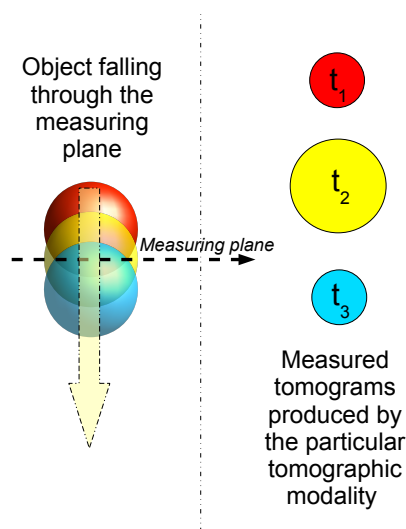


Figure 4.5: Object falling through a measuring plane of a tomograph with a particular measurement frequency. The figure indicates that 3 tomograms are obtained, one at time $t_1$, $t_2$ and $t_3$ respectively.

plane of a tomograph. The red sphere indicates the object at a time $t_1$, the yellow sphere indicates the object at a later time $t_2$ as it is falling downward. The blue sphere indicates the object at a time $t_3$ when the object has almost passed completely through the measuring plane.

For each tomographic modality the measuring plane will be different. For example: with the ECT tomograph the measuring plane will actually be a volume and not a 2D plane through the fluidized bed. Nevertheless the images obtained from a tomograph is called tomograms and usually represents slices through the object of interest. The tomograms can represent various physical quantities and in the case of fluidized beds they

usually represent the solid fraction distribution within the fluidized bed reactor. This was also the case for the two tomographs utilised in the present study.

In Figure 4.5 the tomograms, illustrated on the right, vary in size. The reason for this is linked to $t_1$, $t_2$ and $t_3$. When the sphere has crossed the measuring plane the first measurement was made and a small diameter circle was obtained as tomogram. At $t_2$ the next measurement was made and the object was recorded while its largest diameter was crossing the measuring plane. At $t_3$ the object has nearly passed through the measuring plane and thus a small diameter of the sphere was measured again. If the measurement frequency was increased, more than three tomograms would have been obtained. Therefore depending on the speed of the physical phenomena measured, the sampling speed of the tomograph has to be adjusted. From this it follows that if the tomograph has two measuring planes with a fixed distance between them, the speed of a object moving though both planes can be estimated. When the speed of the moving object or phenomena is known and the sampling speed is fast enough, the tomograms can be stacked and reconstructed to produce a 3D image of the original object. This will be further elucidated in the following sections.

### 4.2.1   ECT experiments

Process tomography has been used to visualise internal flow behaviour of numerous industrial processes [35]. In the past intrusive techniques were used in an attempt to visualise flow processes that would otherwise not be studied visually. The problem with such intrusive measuring techniques is that they alter the normal flow behaviour of the process. Doubts thus arises whether the recorded data is an accurate reflection of how that process would otherwise behave, react or change. In fluidized beds the flow behaviour is of great importance. The better a rector can be understood the better predictions can be made of its behaviour. Better modelling and non-intrusive measurements of bubbling behaviour, mixing and circulation properties can have a drastic impact on optimising fluidized bed reactors.

A two plane ECT system was used in the present study. It consists of two arrays of electrodes and each array contains twelve electrodes. In Figure 4.6 (a) a schematic drawing of the ECT sensor is given. The location and size of the electrodes were designed by Process Tomography Ltd. [36]. The sensor is covered by a grounded screen to protect the electrodes from external noise. Because the sensor operates with a soft field, it is very susceptible to external interference. The non-invasive nature of the sensor can be observed in Figure 4.6 (b). The electrodes are placed on the circumference of the experimental tower and thus does not influence the internal flow behaviour. The ECT tomograph produces a cross-sectional



(a)                                           (b)

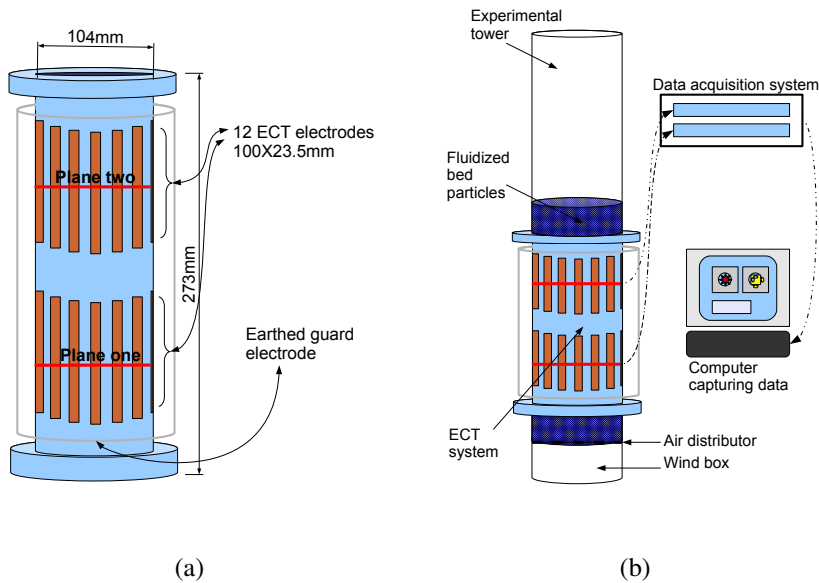Figure 4.6: A not to scale drawing of the two plane ECT tomograph utilised in the present study. (a) The two measuring planes of the system are indicated together with the electrodes and earthed guard screen. (b) The ECT tomograph together with the experimental tower, acquisition system and the computer recording the data.

image (tomogram) showing the distribution of electrical permittivities of

the content of the experimental tower from measurements taken at the
boundary of the vessel [37].  The capacitance reading is taken between
each set of electrodes and thus $n(n-1)/2$ different capacitance values
are recorded in one measurement, where *n* is the number of electrodes.
These measurements are interpreted and illustrated as a colourful image
using a reconstruction algorithm provided by Process Tomography Ltd.
[36].  An example of a tomogram depicting the solid fraction distribution
in a fluidized bed is given in Figure 4.7 (b).  The resolution of the image is
usually relatively low but can be sampled at high sample rates (low spatial
resolution but high temporal resolution).  Off-line image processing can
also improve the quality of the tomogram dramatically [9].

The measuring planes are situated at two different locations.  One at
height of 156.5*mm* and the other at a height of 286.5*mm* above the gas
distributor.  The lower plane will be called plane one and the upper plane,
plane two (refer to Figure 4.6 (a)).  Even though the ECT system calcu-
lates averages, the data that are obtained are viewed as a slice through the
bed at the center of each sensor.  Plane one and plane two are thus located
at the center position of the electrodes (refer to Figure 4.6 (a)).

The obtained image consists of pixels and each pixel represents an av-
erage solid fraction value.  The average is taken over a rectangular volume
equal to 1.1*cm*$^3$ [37].  A 32×32 pixel image is produced and the pixels
that falls outside the circular tower will assume zero values (refer to Fig-
ure 4.7).  Theoretically, the more electrodes used, the smaller the elec-
trodes become and the more dominant the background noise can become.
Thus a trade of has to be made so that the electrode is not too small but
also not too large.  When the electrodes are too large, the resolution of
the produced image will be very low.  The system used in the present
study, with 12 electrodes, can capture up to a 100, 32×32 matrix maps
of solid fractions per second and increasing to 200 frames per second for
an 8 electrode sensor [37].  Practically between 6 and 16 electrodes are
normally used [36].

The two plane ECT tomograph is typically employed to measure the
speed of bubbles in fluidized beds.  If one bubble can be traced from
one plane to the next, the time it takes for the bubble to traverse from

(a)                                    (b)
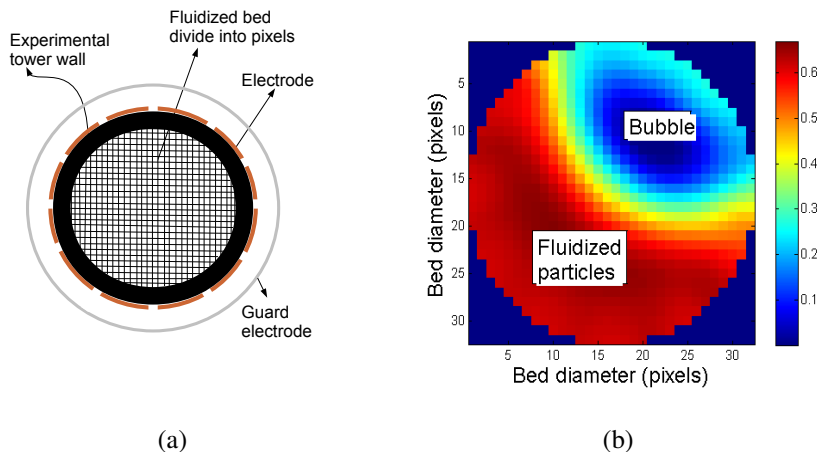
Figure 4.7: (a) A cross-sectional view of the ECT sensor together with the 1024 pixels created by the reconstruction program and (b) a cross-sectional image (tomogram) of the experimental tower indicating the solid fraction values inside the tower at a particular plane. Red indicates particles at minimum fluidization conditions and blue indicates air.

one plane to the other, can be obtained. Using the distance between the two sensing planes the speed of a particular bubble can be determined. In the case of the ECT measurements bubble rise velocities could not be measured. The centers of the electrodes were 13*cm* apart and thus bubbles will coalesce as the bubbles traverse from one measuring plane to the next. Therefore bubble velocity correlations were used to create a spatial 3D image from the collected temporal tomographic data (See Paper D). A reconstruction program was developed in the present study to obtain 3D bubble information from the 2D tomograms produced by the ECT tomograph.

**Statistical diagnosis**

The quality of fluidization can be described in terms of the uniformity of distribution of the fluidizing gas [38]. Several measurement techniques

have been utilised in the past to investigate the quality of fluidization or the gas maldistribution in a fluidized bed. These techniques include pressure probe measurements [39, 13], temperature probe measurements [39], $\gamma$-ray tomography and acoustic measurements [5, 40]. The different measurement techniques have different advantages and disadvantages and can be used to diagnose the quality of fluidization.

Good quality fluidization can be obtained by keeping pressure fluctuation as small and frequent as possible as this will indicate numerous small bubbles [13]. Statistical methods in combination with the fluidization index and the maldistribution factor, have been successfully used to diagnose the fluidization quality in fluidized beds [13, 39, 40]. Since these methods have successfully been used with pressure fluctuation measurements, it appears feasible to do the same analysis with solid fraction fluctuation measurements obtained with the ECT tomograph. Pressure fluctuations are an indirect indication of the solid fraction fluctuation in the bed and by using the ECT tomograph the entire cross-section of the bed is taken into account as oppose to only a probe volume [9]. A pressure probe is usually located at the bed wall and according to Saxena et al. [39] the probe will only register damped pressure fluctuations that reaches the bed wall. Viewing the entire cross-section of the experimental reactor will give a better representation of the dynamic behaviour of the bed. The data obtained with the ECT tomograph can also be viewed as images (tomograms) which can be used to confirm the behaviour deduced from the statistical analysis.

The aim of Paper G was to use statistical methods to diagnose the quality of fluidization for four different mixtures of spherical glass particles and to illustrate the usefulness of the ECT tomograph for this purpose. The influence of small particles on the overall bed fluid dynamics, were also investigated. The analysis was performed on cross-sectional solid fraction data obtained with an ECT tomograph at two bed heights. It was found that small particles had the effect of smaller bubbles and better quality fluidization. These observations were also confirmed when compared with tomograms created from the ECT data. ECT thus provides an added advantage, above some other measurement techniques, by provid-

ing a non-intrusive view of the flow behaviour alongside the other diagnostic techniques. The aim of Paper H was to use the ECT tomograph as a non-invasive and online measuring technique to identify polydispersity due to segregation of different particle sizes with the same material density. Using these statistical methods the ECT tomograph proved to be equally effective at diagnosing the quality of fluidization compared to other popular measurement techniques used in industry.

**Practical application**

The particles in a biomass gasifier are mainly a mixture of wood chips, char particles and bed material. The char particles have a significant lower density than the bed material, and also a wider range of particle sizes and larger mean particle diameter. The difference in particle properties may cause segregation and thereby influence on the fluidization properties and the flow behaviour in the bed. The aim of Paper I was to study the fluidization properties in cold fluidized bed with different mixtures of particles. ZrO and plastic particles with a density ratio of 6 were used in the experiments to simulate the bed material and the char particles in a biomass gasifier. The fluidization properties were studied using pressure sensors and Electrical Capacitance Tomography (ECT). The experimental results show that the minimum fluidization velocities depend on the particle composition in the bed. The minimum fluidization velocity reaches a maximum when 20% plastic particles are added to the ZrO powder and decreases again when the fraction of plastic beads are further increased. The theoretical minimum fluidization velocities for the different mixtures agree well with the experimental data. The standard deviations of the pressure and the ECT measurements showed that the minimum fluidization velocities are higher in the lower part than in the higher part of the bed. This observation is more significant in the mixtures with high fraction of plastic particles. This indicates that the plastic particles move upward in the bed and that mainly ZrO particles are present in the lower part of the bed. This is also visually observed during the experiments. Segregation can give low degree of particle motion in parts of

the bed. Investigation of fluidization behaviour of the different mixtures in this study may be useful as an initial step of analysing the complex system of a bubbling fluidized bed gasifier.

### 4.2.2 Time resolved X-ray tomography experiments

Currently there are several tomographic systems being used in process technological research. These systems include Electrical Capacitance Tomography (ECT), Electrical Resistance Tomography (ERT) and X-ray tomography. Using these measuring techniques an opaque system, like a fluidized bed, can become transparent [8]. X-rays, Gamma rays, Electrical fields and current can move through such systems where light (low energy radiation) cannot. Tomographic techniques can thus also be used with nuclear methods and is generally referred to as nuclear densitometry [8]. Techniques like ECT and Electrical Impedance Tomography (EIT) operates with soft fields. These soft field techniques operates on the principal that a change in the electromagnetic field at one location influences the entire field [8]. The draw back of such techniques is typically that the size of the experimental tower is limited.

Nuclear tomographic techniques or nuclear densitometry relies on hard fields and does not have the same sort of constraints as the soft field measuring systems have. An example of a hard field measuring technique is X-ray tomography. Thus larger tower diameters can be studied without the loss of resolution in the center of the tower. These nuclear measuring techniques have the added disadvantage of being dangerous and expensive compared to other techniques. Special lead insulated room or facilities are required together with advanced safety protocols and regulations. There is always some inherent noise associated with nuclear techniques and because of this the temporal resolution is relatively low compare to some of the other tomographic modalities [8]. The time-resolved X-ray tomography system used in the present study is located at the Technical University of Delft (TU Delft) in the Netherlands. The measurements obtained using this system together with Digital Image Processing (DIP) package produced by the Quantitative Imaging Group from TU Delft,

made it possible to create 3D images of bubbles encountered in a flu-
idized bed. These 3D images also provide information about the recorded
bubbles, such as the bubble volume, frequency and location. In Figure 4.8
(a) a typical 3D image is provided collected over a 1.6*s* time interval. In
Figure 4.8 (b) an image is provided before it was processed into a three
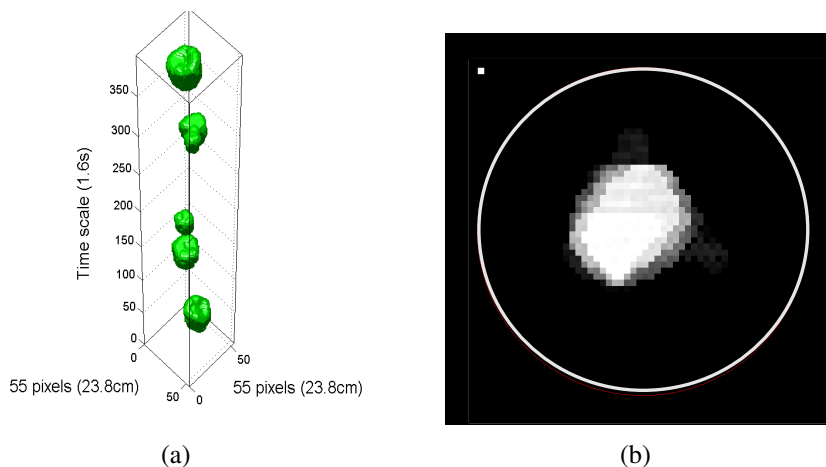dimensional form. These 2D images are staked to create the 3D image
shown in Figure 4.8 (a).

(a)                                          (b)

Figure 4.8: (a) 3D-image of bubbles rising in a fluidized bed with a $55 \times$
55 pixel resolution. (b) A typical 2D greyscale tomogram of a bubble
rising in a fluidized bed. The white line indicates the experimental tower
and at the top left corner the size of a single pixel is illustrated.

In the measurement system used in Paper E and F, three X-ray sources
were used that each created a fan beam through the fluidized bed. Each
fan beam fell onto two array detector consisting of 32 $CdWO_4$ detectors
[8]. The set-up used in the present study is illustrated in Figure 4.9. The
red lines represent the path of radiation detected by each detector respect-
ively. The fluidized bed is located in the middle of the set-up, surroun-
ded by the detectors and sources and its diameter was 23.8*cm*. Figure
4.9 was created by a simulation program developed by Mudde and co-
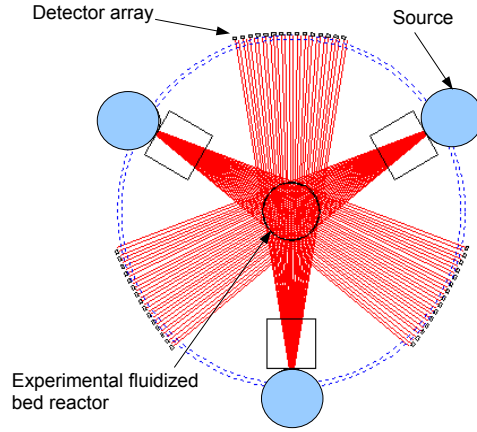workers at TU Delft. The X-ray system can have a sampling frequency of

Figure 4.9: Three X-ray sources that simultaneously radiate an X-ray fan beam through the experimental fluidized bed tower or reactor. Two sets of 32 detectors have been allocated to each source.

$2500 frames/s$ but due to some inherent noise in the X-ray sources the obtained data had to be averaged. This was done by averaging over ten measurements which in turn lowered the sampling frequency to $250 frames/s$. This averaged data can be converted to a line-averaged solid fraction value by using calibration curves [8] (for details regarding calibration refer to Paper E and F).

The TU Delft X-ray tomography system consists of two arrays of detectors $4cm$ apart and both consisting of 32 detectors for each of the 3 sources. The distance from the center of the bed to the detector arrays was $85.8cm$ and the distance from the center of the bed to the sources was $71.6cm$. All of the X-ray beams originate from an approximate point source and diverges from there. Thus the effective distance between the measuring planes can be shown to be equal to $1.86cm$. With these two measuring planes it was possible to determine the bubble rise velocity. Bubble size and velocity are crucial in determining factors such as the

particle residence time, particle entrainment and heat and mass transfer in a fluidized bed [41]. Thus to be able to determine the bubble shape, size and velocity is of paramount importance and the X-ray tomographic system allows researchers to do exactly that.

To be confident in the results obtained from the time-resolved X-ray tomography system it is important to investigate several measuring scenarios and the reliability of the results under typical operating conditions [37]. This was done in Paper E with the focus on the experimental span and its influence on the dynamic parameters of a fluidized bed. Paper E forms part of exploring the capabilities of the time-resolved X-ray tomography system and functions as a user manual for future researchers [37].

Each tomographic modality has its own limitations and advantages and in Paper F two modern tomographic systems were evaluated with respect to their performance on a cold dense fluidized bed. The two tomographic modalities investigated are Electrical Capacitance Tomography (ECT) and time-resolved X-ray tomography. The study was performed on spherical glass particles with various particle size distributions that could mainly be classified as Geldart B or D particles. Two experimental towers were employed, one with a diameter of $10.4cm$ and the other $23.8cm$ while compressed air was used as fluidizing fluid during all of the experiments. Results obtained with both systems were provided in comprehensive figures and tables and some first result were given, obtained with the time-resolved X-ray tomography system. In Figure 4.10 an example is provided of bubble volume data collected with the two tomographs. In Paper F the bubble size measurements of both tomographs are compare with several theoretical correlations via the root mean square error of the predictions (RMSEP). With the results it was also concluded that a small amount of small particles can noticeably alter the fluidization fluid dynamics of a powder. The bubble frequencies were also presented to aid in understanding the fluid dynamic behaviour of the powders investigated. A comprehensive summary of the two tomographic modalities was also provided in Paper F.
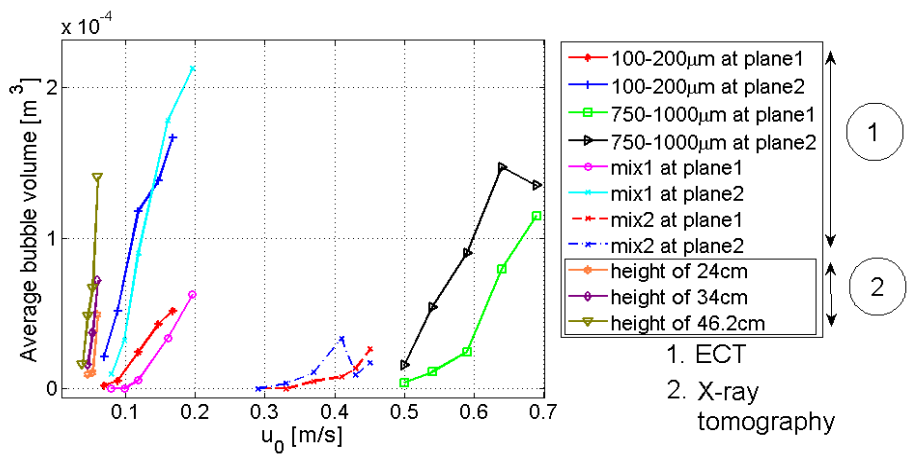
Figure 4.10: Comparison of the ECT- and Time resolved X-ray tomography average bubble volume data as a function of the superficial velocity, $u_0$.

# Chapter 5

# Conclusion and recommendations

The papers presented in the present study aim to elucidate the complex fluid dynamic phenomena in a cold dense phase fluidized bed reactor. Theoretical and experimental studies were conducted with this aim and several advances have been made within the field of fluidization during the course of the present study.

## 5.1   Conclusion

Pressure drop measurements were obtained during the theoretical studies regarding the shifting parameter. These measurements were used to investigate the accuracy of the produced correlations to experimental data. Pressure probes were located at several locations along the column height and the pressure drop was calculated between these locations.

In the experimental studies, Electrical Capacitance Tomography (ECT) and time-resolved X-ray tomography were employed. Various physical phenomena were investigated with these modalities using various particle size distributions.

### 5.1.1   Theoretical studies

- (*Paper A and B*) In the theoretical investigations it was found that
  a powered addition procedure can be used to correlate the pres-
  sure drop in the transition region between a fixed and fluidized bed.
  The aim of these studies were to quantify and explain the physical
  meaning of the shifting parameter. The shifting parameter with a
  value of approximately 15 was found to produce an adequate correl-
  ation with experimental pressure drop data in the transition region
  between a fixed and fluidized bed. This value was independent of
  the particle size distribution and particle density for the parameters
  investigated. Thus an effective correlation is produced to give an
  adequate prediction of pressure drop data for a fluidized bed tra-
  versing from fixed to fluidized regime.

- (*Paper C*) Bubbles in fluidized beds are one of the major phenom-
  ena through which mixing takes place. Better understanding of
  physical phenomena in and around bubbles in a fluidized bed is of
  great importance. Knowledge in this regard can help engineers and
  scientists to design and develop more effective fluidized bed react-
  ors. In the present study a model describing the voidage distribution
  in front and behind a bubble in a fluidized bed was reexamined and
  extended. The model suggested is not complete or satisfactory. This
  work is only the initialisation of a research project to model the flow
  behaviour in and around a bubble in a fluidized bed. This model,
  originally suggested by Buyevich et al. [7], can be developed into a
  useful and convenient predictive tool. At the present time the model
  gives very good results in the area close to the front of the bubble.
  This was established by using data that was acquired using CFD
  simulations. Suspected limitations of the models used to predict
  the relative interstitial velocities might have been the cause of the
  inaccuracy of the model at $\xi = 90^o$. Nevertheless, these problems
  have the possibility of being addressed in the future and thus render
  a very accurate and useful model for predicting the solid fraction
  distribution all around a bubble in a fluidized bed.

### 5.1.2 Experimental studies

With the tomographic experiments numerous results were obtained.

- (*Paper D*) The influence of small particles in powders used in a flu-
  idized bed has been investigated. A range of different powders and
  powder mixtures have been used and these powders were mainly
  from the Geldart group B. The effect of the small particles in powders
  have been studied by means of the bubble behaviour in the fluidized
  bed. Using an ECT (Electrical Capacitance Tomography) tomo-
  graph data were obtained from a fluidized bed in operation and a
  reconstruction program developed for the present study was used to
  calculate characteristics of the bubbles in the bubbling bed. These
  characteristics were the bubble diameter and volume. From the res-
  ults it can be concluded that adding small particles into a powder
  has the effect of smaller average bubble sizes in the fluidized bed.
  This was observed in both the data obtained for the bubble diameter
  and volume. It was also evident that small particles cause a powder
  that is prone to slugging to require much larger superficial velocit-
  ies before signs of slugging set in. Small particles are thus desirable
  in Geldart D particles as it suppresses the slugging behaviour that
  these particles would usually exhibit and instead causes smaller,
  more frequent bubbles that would lead to better mixing of the bed
  content.

- (*Paper E*) Some dynamic parameters of a fluidized bed have been
  investigated as a function of the experimental span. These para-
  meters were the bubble rise velocity, the average bubble volume
  and the bubble frequency. Several different superficial gas velo-
  cities were also used to investigate the effect of the experimental
  span on these particular dynamic parameters. In previous research
  done on this topic, but with an Electrical Capacitance Tomography
  system (ECT system), it was found that a minimum experimental
  span of 60$s$ must be used to obtain reliable results [37]. The dy-
  namic parameters that Makkawi and Wright [37] investigated were

the bubble rise velocity and frequency. For measuring the solid fraction Makkawi and Wright [37] found that 20*s* will produce a reliable result. For the time-resolved X-ray tomograph investigated in the present study different results were obtained. In using a single jet it was found that a measuring span of 40*s* produced reliable results for the bubble rise velocity. In the case of the average bubble volume and bubble frequency a 20*s* experiment produced reliable results with using the single jet. In using the porous plate distributor a measuring span of 45*s* was adequate for determining the bubble rise velocity while 25*s* were sufficient for the average bubble volume and bubble frequency. From using empirical equations it was also estimated that a threshold value of 0.465 will produce results that agree with previously estimated correlations. The present study forms part of exploring the capabilities of the time-resolved X-ray tomograph and functions as a user manual for future researchers [37].

- (*Paper F*) The present study compared two tomographic measurement systems. The two systems used were Electrical Capacitance Tomography (ECT) and time-resolved X-ray tomography. Both tomographs record relevant data on a non-intrusive manner and provided 3D data that could readily be employed to studying fluid dynamic effects in a fluidized bed. Each system has advantages and limitations and depending on the application a choice should be made which system is most fitting. The results obtained from both tomographs were compared with some established bubble size correlations from the open literature. Relatively good agreement was found between the theory and experiments. The powder with the widest particle size distribution had the largest discrepancy with the theory. The conclusion was that the correlations could not account for all of the fluid dynamic effects associated with a wide particle size distribution. These conclusions were also supported by the bubble frequency data presented in the present study.

- (*Paper G*) In the present study the usefulness of an ECT tomograph

as a diagnostic tool in a fluidized bed was illustrated. Using statistical methods the quality of fluidization of a fluidized bed was assessed. Using these statistical methods the ECT tomograph proved to be equally effective at diagnosing the quality of fluidization compared to other popular measurement techniques used in industry. These methods include temperature probes, pressure probes and acoustic or vibration measurements. The ECT tomograph together with the statistical analysis was employed to investigate the influence of small particles on the fluid dynamics of a fluidized bed. It was found that small particles had the effect of smaller bubbles and better quality fluidization. These observations were also confirmed when compare with tomograms created from the ECT data. ECT thus provides an added advantage, above some other measurement techniques, by providing a non intrusive view of the flow behaviour alongside the other diagnostic techniques.

- (*Paper H*) An Electrical Capacitance Tomography (ECT) system has been utilised in the present study to identify the presence of axial and/or radial segregation. The average solid fraction fluctuations was measured at two heights in the fluidized bed. In previous studies it was postulated that the standard deviation of the average solid fractions will produce a linear relationship with the superficial velocity as long as the bed is in the bubbling regime [9]. This was confirmed for Geldart B particles but for Geldart D particles and wide particle size distributions this was not the case. A change in the standard deviation curve gradient usually indicate a regime transition. In the present study it was shown that a change in the gradient of the standard deviation curve can thus also identify the presence of segregation. Using the qualitative images recorded with the ECT tomograph it was possible to observe segregation behaviour in accordance with the standard deviation curves. It was also observed that when doing experiments with multiple steps in the superficial velocity the direction of the steps (increasing or decreasing) are important, especially for powders with a wide particle

size distribution.

Further research might connect the particular segregation phenomena (axial or radial segregation) with the behaviour of the standard deviation curves. This might be achieved by employing novel core sampling techniques, as illustrated by Wormsbecker et al. [42], along with non-invasive measurements like the ECT tomograph.

- (*Paper I*) Experiments are performed with ZrO and plastic beads with density 5850 and $964kg/m^3$ respectively. These particles have about the same density ratio as the char and bed material in a fluidized bed gasifier. The experimental results can therefore give an indication of how mixtures of particles with different densities and particle size and shape may influence on the flow behaviour in an actual gasifier. The fluidization properties and segregation tendencies are investigated for the pure ZrO and plastic particles and for mixtures of ZrO and 10, 20, 30 and 40 vol% plastic particles. The flow behaviour for the different cases is studied by using pressure sensors and Electrical Capacitance Tomography (ECT). Average pressure drop over the bed is used to determine the minimum fluidization velocities ($u_{mf}$) for the different cases. The experimental results showed that the minimum fluidization velocities strongly depended on the particle composition in the bed. Experimental results from pressure sensors and ECT show the same tendency of segregation for mixtures of particles. The ECT gives somewhat higher $u_{mf}$ values than the pressure sensors. All the experiments show that the bubble activity increases with height in the bed when the superficial velocity is increased above the $u_{mf}$.

## 5.2   Recommendations for future studies

Shifting parameter investigations:

- In future studies the shifting parameter and its dependence on other physical properties can be investigated. If the physical meaning of

the shifting parameter can be explained and/or defined it will further the research communities understanding of the transition regions in various physical phenomena, such as the fluidization of a fixed bed.

- In particular the influence of the particle size distribution width on the shifting parameter can be investigated as a wide particle size distribution might be the main cause of a gradual transition between a fixed and fluidized bed [31].

Bubble model extension:

- The Buyevich model that was extended in two dimensions in the presented study can be further developed. Better modelling and understanding of this model can aid in understanding particle behaviour in a dense particle cloud.

- Both polar coordinate components can be taken into account to avoid the unrealistic results obtained at a polar angle equal to $\pi/2$.

- Other closure models can be employed for the various parameter involved in the conservation of momentum equation of the dispersed phase. This might change the outcome of the model and/or further the understanding of the physical phenomena.

X-ray tomography:

- The influence of the measurement height on the experimental span can be investigated.

Statistical fluidized bed diagnosis:

- The statistical methods employed in the present study can be developed further to provide a clear and concise guideline for diagnosing a fluidized bed via statistical methods and ECT. This noninvasive means of diagnosing a fluidized bed might prove to be of great value in preventing unscheduled industrial shutdowns and therefore optimising productivity.

- The segregation behaviour reported in the present study can be investigated by taking particle samples from the fluidized bed at several locations. This might be an effective way to validate the suspected segregation behaviour.

- The segregation experiment can be done with a longer experimental span per experiment. This might change the segregation behaviour of the bed. Results of such experiments will elucidate the results presented in the present study.

Verify scaling models:

- By using scaling models the results of this thesis might be applied and/or investigated in larger scale fluidized beds.

In conclusion this study has widened the research communities understanding of fluidized bed reactors and set the platform for further studies in the fascinating phenomena known as fluidization.

# Bibliography

[1] D. Kunii and O. Levenspiel. *Fluidization Engineering*. Butterworth-Heinemann, second edition, 1991.

[2] V. Mathiesen. *An experimental and computational study of multiphase flow behavior in circulating fluidized beds*. PhD thesis, NTNU and Telemark University College, Kjolnes ring, N-3914, Porsgrunn, Norway, 1997.

[3] M. Horio. Fluidization-past and future. In S.D. Kim, Y. Kang, J.K. Lee, and Y.C. Seo, editors, *Fluidization XIII*, pages 25–32, Korea, May 2010. ECI.

[4] J.R. Grace. A perspective on development of novel fluidized bed processes for a more sustainable global future. In S.D. Kim, Y. Kang, J.K. Lee, and Y.C. Seo, editors, *Fluidization XIII*, pages 1–8, South Korea, 5 2010. ECI.

[5] H. Azizpour, R. Sotudeh-Gharebagh, R. Zarghami, M. Abbasi, N. Mostoufi, and M.J. Mahjoob. Characterization of gas-solid fluidized bed hydrodynamics by vibration signal analysis. *International Journal of Multiphase Flow*, 37:788–793, 2011.

[6] J. Werther. Measurement techniques in fluidized beds. *Powder Technology*, 102:15–36, 1999.

[7] Y.A. Buyevich, J.G. Yates, D.J. Cheesman, and K.T. Wu. A model for the distribution of voidage around bubbles in a fluidized bed. *Chemical Engineering Science*, 50(19):3155–3162, 1995.

[8] R.F. Mudde. Time-resolved x-ray tomography of a fluidized bed. *Powder Technology*, 199:55–59, 2010.

[9] Y.T. Makkawi and P.C. Wright. Fluidization regimes in a conventional fluidized bed characterised by means of electrical capacitance tomography. *Chemical Engineering Science*, 57:2411–2437, 2002.

[10] A. Acosta-Iborra, F. Hernandez-Jimenez, C. Sobrino, and M. de Vega. Experimental and computational study on the bubble behavior in a 3-d fluidized bed with vertical-axis, rotating distributor. In S.D. Kim, Y. Kang, J.K. Lee, and Y.C. Seo, editors, *Fluidization XIII*, pages 351–358, Korea, May 2010. ECI.

[11] D. Gidaspow. *Multiphase Flow and Fluidization, Continuum and Kinetic Theory Descriptions*. Academic Press, Harcourt Brace & Company, 525 B Street, Suite 1900, San Diego, California 92101-4495, 1994.

[12] Z. Chen, L.G. Gibilaro, and P.U. Foscolo. Fluid pressure loss in slugging fluidised beds. *Chemical Engineering Science*, 52(1):55–62, 1997.

[13] C.L. Lin and M.Y. Wey. Statistical and power spectral analysis of quality of fluidization for different particle size distributions at high temperature. *Advanced Powder Technology*, 15(1):79–96, 2004.

[14] A.C. Hoffmann. Manipulating fluidized beds by using internals; fluidization with baffles. Technical report, Stratingh Institute for Chemistry and Chemical Engineering, University of Groningen, Nijenborgh 4, 9747 AG Groningen, The Netherlands. http://web.ift.uib.no/mps/papershtml/npt00/npt99.html.

[15] J. Adanez, A. Abad, F. Garcia-Labiano, P. Gayan, and L.F. de Diego. Progress in chemical-looping combustion and reforming technologies. *Progress in Energy and Combustion Science*, 38(2):215–282, April 2012.

[16] S.R. Dahl and C.M. Hrenya. Size segregation in gas-solid fluidized beds with continuous size distributions. *Chemical Engineering Science*, 60(23):6658–6673, December 2005.

[17] C. Crowe, M. Sommerfeld, and Y. Tsuji. *Multiphase flows with droplets and particles*. CRC Press LLC, 2000 Corporate Blvd., N.W., Boca Raton, Florida 33431, 1998.

[18] H. Cui and J.R. Grace. Spouting of biomass particles: A review. *Bioresource Technology*, 99(10):4008–, 4020 2008.

[19] C. Rautenbach. Modelling of flow through porous packing elements of a co2 absorption tower. Master's thesis, Stellenbosch University, Stellenbosch, South Africa, 2009.

[20] M. Syamlal, W. Rogers, and T.J. O'Brien. *MFIX Documentation Theory guide*. U.S. Department of Energy, Office of Fossil Energy, Morgantown Energy Technology Center, Morgantown, West Virginia, December 1993.

[21] S.W. Churchill and R. Usagi. A standardized procedure for the production of correlations in the form of a common empirical equation. *Ind. Eng. Chem., Fundam.*, 13(1):39–44, 1974.

[22] S. Benyahia, M. Syamlal, and T.J. O'Brien. Extension of hill-koch-ladd drag correlation over all ranges of reynolds number and solids volume fraction. *Powder Technology*, 162:166–174, 2006.

[23] S. Woudberg, J.P. Du Plessis, and G.J.F. Smit. Non-newtonian purely viscous flow through isotropic granular porous media. *Chemical Engineering Science*, 61(13):4299–4308, July 2006.

[24] K.H. Esbensen and L.P. Julius. Representative sampling, data qual-
     ity, validation - a necessary trinity in chemometrics. *Comprehensive
     Chemometrics*, 4:1–20, 2009.

[25] J.R. van Ommen and R.F. Mudde. Measuring the gas-solid distribu-
     tion in fluidized beds - a review. *International Journal of Chemical
     Reactor Engineering*, 6(R3):1–29, 2008.

[26] C.W. Chan, J.P.K. Seville, and J. Baeyens. The transport disengage-
     ment height (tdh) in a bubbling fluidized bed (bfb). In S.D. Kim,
     Y. Kang, J.K. Lee, and Y.C. Seo, editors, *Fluidization XIII*, pages
     225–232, Korea, May 2010. ECI.

[27] X. Fan, D. Parker, Z. Yang, J. Seville, and J. Baeyens. The effect of
     bed materials on the solid/bubble motion in a fluidized bed. *Chem-
     ical Engineering Science*, 63:943–950, 2008.

[28] M. Stein, Y. Ding, J. Seville, and D. Parker. Solid motion in bubbling
     gas fluidized beds. *Chemical Engineering Science*, 55:5291–5300,
     2000.

[29] C. Sierra, F. Bonniol, R. Occelli, and L. Tadrist. Practical scal-
     ing considerations for dense gas fluidized beds interacting with the
     air-supply system. *Chemical Engineering Science*, 64:3717–3720,
     2009.

[30] R. Girimonte and B. Formisani. The minimum bubbling velocity of
     fluidized beds operating at high temperature. *Powder Technology*,
     189:74–81, 2009.

[31] P. Pei, K. Zhang, B. Yu, J. Gao, G. Wu, and D. Wen. Dynamic char-
     acteristics of binary mixtures in a two-jet fluidized bed. *Chemical
     Engineering Science*, 66(8):1702–1714, April 2011.

[32] Y.A. Buyevich. Fluid dynamics of coarse dispersions. *Chemical
     Engineering Science*, 49(8):1217–1228, 1994.

[33] Y.A. Buyevich. Particulate pressure in monodisperse fluidized beds. *Chemical Engineering Science*, 52(1):123–140, 1997.

[34] J.F. Davidson and D. Harrison. *Fluidized particles*. Cambridge University Press, Cambrige, U.K., 1963.

[35] C. Qiu, B.S. Hoyle, and F.J.W. Podd. Engineering and application of dual-modality process tomography system. *Flow Measurement and Instrumentation*, 18:247–254, 2007.

[36] Process tomography Ltd., 86 Water Lane, Wilmslow, Cheshire. SK9 5BB, UK. *PTL300-TP-G ECT system, Operation manual*, 07 2003.

[37] Y.T. Makkawi and P.C. Wright. Electrical capacitance tomography for conventional fluidized bed measurements-remarks on the measuring technique. *Powder Technology*, 148:142–157, 2004.

[38] A.K. Patel, S.S. Waje, B.N. Thorat, and A.S. Mujumdar. Tomographic diagnosis of gas maldistribution in gas-solid fluidized beds. *Powder Technology*, 185:239–250, 2008.

[39] S.C. Saxena, N.S. Rao, and V.N. Tanjore. Diagnostic procedures for establishing the quality of fluidization of gas-solid systems. *Experimental Thermal and Fluid Science*, 6:56–73, 1993.

[40] N. Salehi-Nik, R. Sotudeh-Gharebagh, N. Mostoufi, R. Zarghami, and M.J. Mahjoob. Determination of hydrodynamic behaviour of gas-solid fluidized beds using statistical analysis of acoustic emissions. *International Journal of Multiphase flow*, 35:1011–1016, 2009.

[41] S. Karimipour and T. Pugsley. A critical evaluation of literature correlations for predicting bubble size and velocity in gas-solid fluidized beds. *Powder Technology*, 205:1–14, 2011.

[42] M. Wormsbecker, A. Adams, T. Pugsley, and C. Winters. Segregation by size difference in a conical fluidized bed of pharmaceutical granulate. *Powder Technology*, 153:72–80, 2005.

[43] T. Pugsley, H. Tanfara, S. Malcus, H. Cui, J. Chaouki, and C. Winters. Verification of fluidized bed electrical capacitance tomography measurements with a fiber optic probe. *Chemical Engineering Science*, 58:3923–3934, 2003.

# Part II

# Published and Submitted Papers

# Paper A

# Investigation of the shifting-parameter as a function of particle size distribution in a fluidized bed traversing from a fixed to fluidized bed.

# Investigation of the shifting-parameter as a function of particle size distribution in a fluidized bed traversing from a fixed to fluidized bed.

C. Rautenbach, M.C. Melaaen & B.M. Halvorsen
Institute for Process, Energy and Environmental Technology
Telemark University College
Norway
T: +47 3557 5222; E: christo.rautenbach@hit.no

**ABSTRACT**

Accurate predictions of pressure drops in fluidized beds are of great importance in the industry. Up to date no satisfactory correlation exists to predict the pressure drop in a fluidized bed as the bed is traversing from one regime to another. In the present study the powered addition correlation [1] is investigated for this particular application. It has been found that this correlation is well suited for the investigated application.

**INTRODUCTION**

In the present study experiments have been performed in an experimental fluidized bed reactor. The experimental tower has been equipped with a set of nine pressure sensors located at different positions along the height of the tower. The tower has a diameter of $0.072m$ and a height of $1.5m$. A procedure providing a correlation for data in the transition region between asymptotic solutions or limiting correlations have been described by Churchill and Usagi [1]. This correlation can generally be expressed as $y^s\{x\} = y_o^s\{x\} + y_\infty^s\{x\}$, where $y_o\{x\}$ and $y_\infty\{x\}$ represents the asymptotic solutions for large and small values of the independent variable $x$ and $s$ is the so called shifting parameter. Changing the value of $s$ shifts the correlation given by $y\{x\}$ closer to or away from the asymptotic solutions. This procedure has been proven to give good correlations in a wide range of applications. The exact physical meaning of this shifting parameter *s*, is still unknown and the present study is part of an ongoing investigation into the physical meaning and possible mathematical expression for the shifting parameter. In the present study only one possible parameter influencing the shifting parameter is investigated, namely different particle size distributions.

A series of different powders have been used to investigate the influence of a particular parameters on the shifting parameter, *s*. Up to date no expression has been stated for this shifting parameter to govern the transition from fixed to fluidized bed. In the present study spherical glass particles have been used with different particle size distributions. By keeping all the parameters constant except the particle size distribution, the influence of the particle size distribution on the shifting parameter could be investigated. Several different drag models were used to serve as a control

for investigating the shifting parameter. The results are given in the form of pressure drop data versus superficial velocity data. Experimental data are presented with the drag model correlations and the investigated values of the shifting parameter, *s*. Some of the drag models that were used were the Syamlal O'Brien drag model [2] and the extended Hill-Koch-Ladd drag correlation [3]. The results are evaluated and discussed.

**PROPERTIES OF THE EXPERIMENTAL BEDS**

At the point of minimum fluidization the total weight of the packed bed is supported by the upward force created by the gas moving upward through the porous structure. As the superficial velocity is increase from this point the pressure drop remains practically the same [4]. The explanation for the slight increase of pressure drop with an increase of superficial velocity may be attributed to wall effects, more specifically, slugging [5]. In the present study the pressure drop in the fluidized regime will be assumed constant. At this point of equilibrium (minimum fluidization velocity) the pressure-drop is given by

$$\Delta p = (1 - \epsilon)(\rho_p - \rho_f)Lg, \tag{1}$$

with $\rho_p$ the particle's density, $\rho_f$ the fluid density and $L$ the bed height. In the present study spherical glass particles were used with a density of $2485\ kg/m^3$. The three different size distribution that were used are $100 - 200\mu m$, $400 - 600\mu m$ and $750 - 1000\mu m$. The relevant parameters of the powders are given in Table 1.

| Powder size distributions | $100 - 200\mu m$ | $400 - 600\mu m$ | $750 - 1000\mu m$ |
|---|---|---|---|
| $\epsilon$ | 0.39 | 0.37 | 0.36 |
| $(1 - \epsilon)(\rho_p - \rho_f)g\ [N/m^3]$ | 14848 | 15334 | 15578 |

Table 1: Relevant parameters of the powders used in the present study.

All of the data is at the point of minimum fluidization except the $750 - 1000\mu m$ powder. Because of a lack of experimental data in the fully fluidized regime data were used when the bed was fluidized for the first time. The only practical effect of this was that the porosity was lower than it would have been if the bed has been fluidized before. By using the correct data this should pose no problem in the accuracy of what the drag models predict.

**POWERED ADDITION AND THE ASYMPTOTIC FUNCTIONS**

In the work done by Chrurchill and Usagi [1] they proposed the use of a general empirical equation for correlating behavior between two asymptotic solutions or limiting correlations. In the present study the lower limiting condition will be the fixed bed regime. Different drag models will be used to model this regime. The upper limiting condition will be described by the constant pressure-drop given when the upward force created by the upward moving gas is equal to the weight of the bed. It can be shown that this constant pressure drop for the fluidized regime is given by $(1 - \epsilon)(\rho_p - \rho_f)g$, as mentioned earlier. A problem arises for large values of the independent variable as a

constant value is not a upper bound [1]. Through numerous graphical representation Churchill and Usagi [1] suggested equation (2) to give a linear relationship on a *log-log* plot and can be written as

$$F(q) = \frac{H(q)}{H(\infty) - H(q)},\tag{2}$$

where $H(q)$ is the asymptotic function desired for large values of the independent variable and $H(\infty)$ is the constant value to which the asymptote will tend to. Thus using equation (2) a function can be determined for $H(q)$ that would be a asymptotic limiting condition for large values of the independent variable, $q$.

   To determine this function $H(q)$ the data points which the function should approximate is used in equation (2). This data points are the pressure drop data in the fluidized regime. It follows that $(1 - \epsilon)(\rho_p - \rho_f)g$ will be taken as the value of $H(\infty)$.

   The $400 - 600 \mu m$ powder will be used to serve as an example of how the function $H(q)$ is deduced. Using the data from Table 1 and the data acquired at the TUC in Norway values of the function $F(q)$ were determined. In Figure 1 (a) the positive values of $F(q)$ is given. It is clear from Figure 1 (a) that there is only three data points while the fluidized region in Figure 1 (b) has at least six data points. The missing three data points can be attributed to the prediction that $(1 - \epsilon)(\rho_p - \rho_f)g$ gives. For the $400 - 600 \mu\ m$ powder the theoretical prediction of equation (1) is lower than some of the data points and as the *log* of a negative value does not exist the negative values of $F(q)$ can not be plotted in Figure 1. As only two data points are required to get a linear approximation the remaining three data points are enough to produce a linear approximation. In Figure 1 (b) an example of $F(q)$ is given if the theoretical prediction of equation (1) was higher than all of the data points. The result would have been more data point and thus a more defined linear relationship.

   With an approximate linear equation for $F(q)$ on a *log-log* scale, a function for the upper bound for large values of the independent variable, $q$, can now be determined. The general function for $H(q)$ can be expressed as

$$H(q) = \frac{H(\infty)}{\frac{1}{F_o}\left(\frac{q_o}{q}\right)^m + 1},\tag{3}$$

with $m$ being the gradient of the linear approximation of $F(q)$ on a *log-log* scale and $F_o$ and $q_o$ any point on the approximated linear curve. For the $400 - 600 \mu m$ powder the upper bound for large values of $q$ is given by

$$H(q) = \frac{15334}{\frac{1}{24.19}\left(\frac{0.199}{q}\right)^{11} + 1},\tag{4}$$

where the point $(0.199, 24.19)$ were chosen as the arbitrary point on the linear approximation of $F(q)$. This function is not a good function for being representative of the behavior of the fully fluidized bed at high values of $q$. After several graphical investigations a new adequate function was formulated. It can be expressed as

$$H(q) = \frac{15334}{\frac{1}{F_o}\left(\frac{0.1q_o}{q}\right)^m + 1},\tag{5}$$
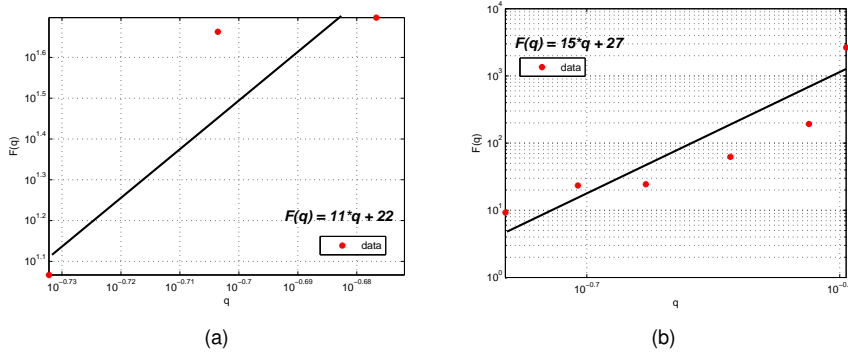
Figure 1: (a) Linear approximation to equation (3) on a *log-log* scaling. (b) Linear approximation to equation (3) on a *log-log* scaling if the calculated value of equation (1) was higher than all the data point values in the fully fluidized regime.

where the only difference to equation (3) is the addition of the factor in front of the $q_o$. The simple reasoning behind this factor lies in the characteristics of the investigated powders. Because two out of the three investigated powders' point of minimum fluidization were above $0.1m/s$ the function $H(q)$ was not adequate. If the minimum fluidization velocity was below $0.1m/s$ the function would produce a result that would give an accurate prediction in the fully fluidized regime (like the $100 - 200\mu m$ powder). Thus by inserting the factor of $0.1$ in equation (5) the equation is assured of giving a usable function for all the powders investigated in the present study. It should be noted that this function, equation (5), is completely empirical. It is only constructed to produce a asymptotic function that would give the value of equation (1) for large values of $q$. This function is only created to be in accordance with the powered addition procedure described by Churchill and Usagi [1].

The general applicability of this function should also still be investigated. In other words, it should be tested for powders with different densities, different particle size distribution than the ones investigated in the present work and different particel shapes, to name but a few. It should be bore in mind that for different powders the factor in front of the $q_o$ in equation (5) might have to be addapted. The higher the superficial velocity value at which the bed is fluidized the smaller factor is added in front of $q_o$. This might seem very empirical, but this is only an estimate to equation (1) and thus keeps the whole theoretical basis of the equation that it is representing. Following the procedure described by Churchill and Usagi [1] a total predictive model for fluidized beds, traversing from a fixed to fluidized regime, can be expressed as

$$\frac{\Delta p}{L} = \left(Drag\ model^{-s} + H(q)^{-s}\right)^{-\frac{1}{s}},\qquad(6)$$

were any adequate drag model can be used. The negative powers of $s$ is because the data is a decreasing power of $q$.

**Drag model investigation along with the shifting parameter, $s$.**

Most drag model need some sort of definition of an average particle size. This is still a source of on going research as it is no trivial task to estimate a good representative particle size diameter. Sieving analysis was performed on the powders used in the present study. This was done to establish the particles size distribution of the powders but also to determine an effective particle size. Several definitions exist for an effective particle size in a powder with a particle size distribution. In the present study the surface-volume mean diameter will be used [4] along with the minimum and maximum particle diameter of each powder. The surface-volume mean diameter can be expressed as

$$\bar{d}_{sv} = \frac{1}{\sum_i x_i/d_i},\tag{7}$$

with $d_i$ the nominal diameter and $x_i$ the mass fraction of the total mass of the corresponding nominal size particles. Thus $\sum_i x_i$ will be equal to 1.
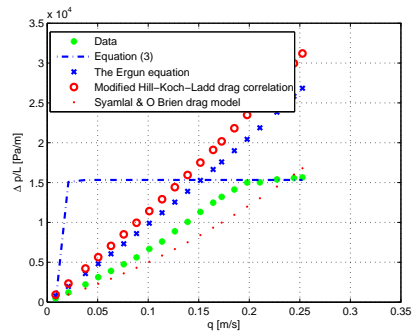
For the $400 - 600\mu m$ powder a surface-volume mean diameter ($\bar{d}_{sv}$) of $482.9$ were calculated and the correlations of the different drag models using this value is given in Figure 2 (b).

In Figure 2 (a) and (b) the minimum and maximum particle size diameters were used respectfully. From these two figures it is clear to see that different models perform better with different representative particle sizes. The Ergun equation [4] and the modified Hill-Koch-Ladd drag correlation [3] performed better with large value of the representative particle diameter. The Syamlal and O'Brien drag model [2] performed very well with a low representative particle diameter.

Because of the accurate prediction of the Hill-Koch-Ladd drag correlation [3] with a representative particle diameter equal to $400\mu m$, it will be used to illustrate the usefulness of the powered addition principle [1]. In Figure 3 different correlations are given with several values of the shifting parameter, *s*. It is clear to see that the higher the value of *s* the more the powered addition correlation shifts towards the asymptotes. At a value of $15$ a satisfactory correlation is produced.
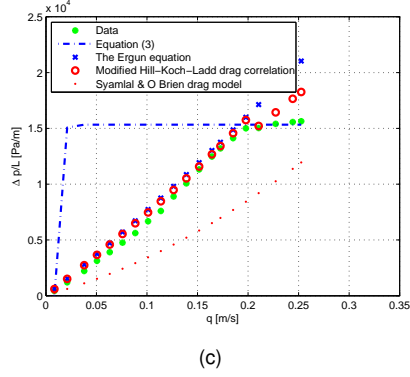


(a)　　　　　　　　　　　　　　(b)

(c)
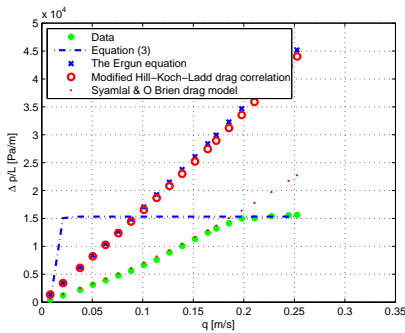
Figure 2: The prediction of different drag models using (a) the minimum particle size diameter ($400\mu m$), (b) the surface-volume mean diameter ($482.9\mu m$) and (c) the maximum particle size diameter ($600\mu m$). The experimental pressure drop data for the $400 - 600\mu m$ powder is given along side the predictions.
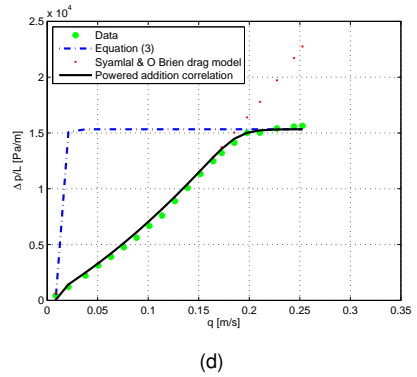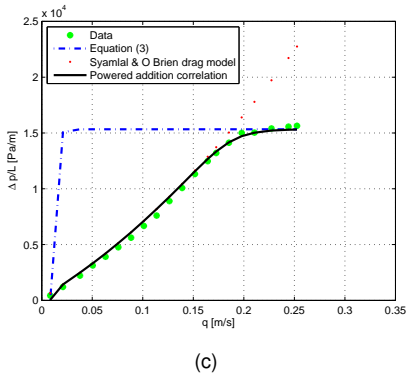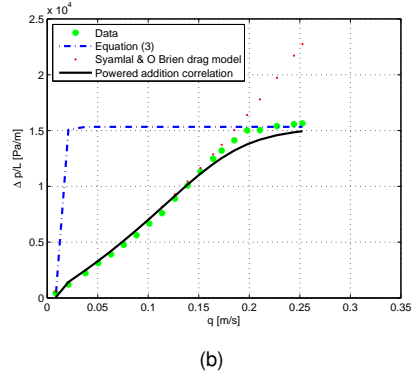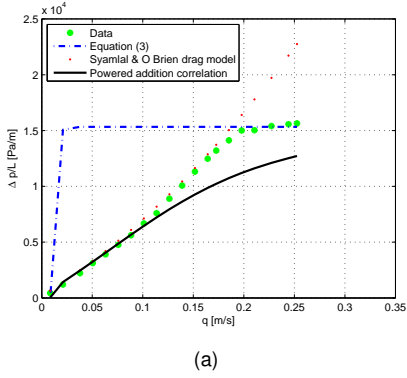


(a)



(b)



(c)



(d)

Figure 3: The powered addition correlation for a fluidized bed traversing from fixed to fluidized regime with the shifting parameter, *s*, equal to (a) 2, (b) 5, (c), 10 and (d) 15.

The accuracy of the fixed bed drag model thus plays a big role in the over all accuracy of the powered addition correlation and the drag models are very dependent on the representative particle diameter, as described earlier.

A similar analysis was done for the $100 - 200\mu m$ and $750 - 1000\mu m$ powders. Only the best results are given in Figure 4. For the $100 - 200\mu m$ powder the Syamlal and O'Brien drag model [2] was not a good representation of the data, even with a representative particle diameter of $100\mu m$. A possible explanation for this can be found in Geldarts classification of particles [4]. The $100 - 200\mu m$ powder is on the boundary between type *A* and type *B* particles whilst the $400 - 600\mu m$ powder is on the boundary between type *B* and *D* powders. The $7500 - 1000\mu m$ powder is a type *D* powder. Thus depending on the type of powder different drag models perform better. In the cases depicted in Figure 4 a particle diameter and model were chosen that best fitted the data. The reasoning was that a proper fitting in the fixed bed regime was required to produce an accurate value for the shifting parameter in each case. Using this best fitting models a value of 15 were found to give a suitable correlation in all the investigated cases.
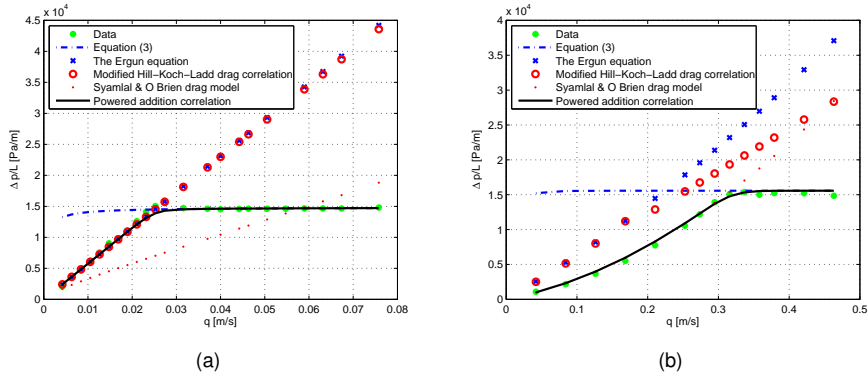


Figure 4: (a) The correlation for the $100-200\mu m$ powder using a representative particle diameter of $190\mu m$ and a $s$- value of 15, (b) the correlation for the $750-1000\mu m$ powder using a representative particle diameter of $750\mu m$ and a $s$- value of 15.

It should be mentioned that in Figure 4 (b) a very crude linear approximation was used for $F(q)$ (refer to equation (2)). The reason for this crude approximation was mainly due to the ossilations in the fluidized regime data for the $750 - 1000\mu m$ powder. Never the less, this approximation still produced an adequte asyptotic function, $H(q)$.

**CONCLUSION**

From the results obtained in the present work it appears that a value of 15 is adequate for the shifting parameter, $s$, independent of the particle size distribution. It can be concluded that the powered addition procedure [1] gives accurate correlations if the drag model used gives an accurate correlation in the fixed bed regime. Different models are suitable for different types of powders. Thus depending on the type of powder

different representative particle diameter should also be used.

It is also apparent that the asymptotic function, $H(q)$, gives stable accurate result if the correct procedure is followed. Even with relatively large fluctuations in the fully fluidized data $H(q)$ still produces an accurate approximation to equation (1).

Further research into the physical meaning of the shifting parameter, *s*, is still needed and can prove very usefully in accurate prediction of different phenomena in a fluidized bed as illustrated in the present work

**NOTATION**

| | |
|---|---|
| $d_i$ | nominal diameter |
| $\bar{d}_{sv}$ | surface-volume mean diameter |
| $F(q)$ | function suggested to be used to produce a linear relationship on a *log-log* scaling |
| $F_o$ | any point on the approximated linear curve |
| $g$ | gravitational acceleration |
| $H$ | asymptotic function for large values of the independent variable |
| $m$ | gradient of $F(q)$ on a *log-log* scaling |
| $p$ | pressure |
| $s$ | shifting parameter |
| $x$ | independent variable |
| $x_i$ | mass fraction |
| $y$ | canonical dependent variable |

**Greek letters**

| | |
|---|---|
| $\epsilon$ | porosity |
| $\rho$ | density |

**Subscripts**

| | |
|---|---|
| $p$ | particle property |
| $f$ | fluid property |
| $o$ | limiting condition for small values of the independent variable |
| $\infty$ | limiting condition for large values of the independent variable |

# References

[1] S. W. Churchill and R. Usagi. A standardized procedure for the production of correlations in the form of a common empirical equation. *Ind. Eng. Chem., Fundam*, 13(1):39–44, 1974.

[2] W. Rogers M. Syamlal and T. J. O'Brien. *MFIX Documentation theory guide*. U.S. Department of energy, Office of fossil energy, Morgantown energy technology center, Morgantown, West Virginia, December 1993.

[3] M. Syamlal S. Benyahia and T. J. O'Brien. Extension of the hill-koch-ladd drag correlation over all ranges of reynolds numbers and solids volume fraction. *Power Technology*, 162:166–174, 2006.

[4] D. Kunii and O. Levenspiel. *Fluidization Engineering*. Butterworth-Heinemann, 1991.

[5] G. Gibilaro Z. Chen and P. U. Foscolo. Fluid pressure loss in slugging fluidized beds. *Chemical Engineering Science*, 52(1):55–62, 1997.

# Paper B

# Investigation of the shifting-parameter as a function of density in the fluidization of a packed bed.

# Investigation of the shifting-parameter as a function of density in the fluidization of a packed bed.

## C. Rautenbach,* M.C. Melaaen* and B.M. Halvorsen*

* Institute for Process, Energy and Environmental Technology, Telemark University College, Norway

christo.rautenbach@hit.no, morten.melaaen@hit.no and britt.halvorsen@hit.no

**Keywords**: Fluidization, power-addition, regime transition, drag models

## Abstract

Accurate predictions of pressure drops in fluidized beds are of great importance in the industry. Up to date no satisfactory correlation exists to predict the pressure drop in a fluidized bed as the bed is traversing from one regime to another.

In the present study experiments have been performed in an experimental fluidized bed reactor. The experimental tower has been equipped with a set of nine pressure sensors located at different positions along the height of the tower. The tower has a diameter of 7.2 *cm* and a height of 1.5 *m*.

A procedure providing a correlation for data in the transition region between asymptotic solutions or limiting correlations have been described by Churchill & Usagi (1947). This correlation can generally be expressed as $y^s\{x\} = y_o^s\{x\} + y_\infty^s\{x\}$, where $y_o\{x\}$ and $y_\infty\{x\}$ represents the asymptotic solutions for large and small values of the independent variable $x$ and $s$ is the shifting parameter. Changing the value of $s$ shifts the correlation given by $y\{x\}$ closer to or away from the asymptotic solutions. This procedure has been proven to give good correlations in a wide range of applications.

A series of different powders have been used to investigate the influence of a particular parameters on the shifting parameter, *s*. Up to date no expression has been stated for this shifting parameter to govern the transition from fixed to fluidized bed. Two powders have been used in the present study and they are Zirconium Oxide (*ZrO*) and spherical glass particles. The powders have the same size distributions but very different densities. The effect of different densities on the shifting parameter was investigated. Several different drag models were used to serve as a control for investigating the shifting parameter. The results are given in the form of pressure drop data versus superficial velocity data. Experimental data are presented with the drag model correlations and the investigated values of the shifting parameter, *s*. Some of the drag models that were used were the Syamlal O' Brien drag model (Syamlal, Rogers & O'Brien (1993)) and the extended Hill-Koch-Ladd drag correlation (Benyahia, Syamlal & O'Brien (2006)). The results are evaluated and discussed.

## Nomenclature

*Roman symbols*

| | |
|---|---|
| $d_{p\,mean}$ | surface-volume mean diameter (m) |
| g | gravitational constant (ms$^{-2}$) |
| L | bed height (m) |
| p | pressure (Nm$^{-2}$) |
| q | superficial velocity (ms$^{-1}$) |
| Re | Reynolds number (-) |
| y | canonical dependent variable (Nm$^{-3}$) |

*Greek symbols*

| | |
|---|---|
| $\epsilon$ | porosity (-) |
| $\rho$ | density (kg m$^{-3}$) |

*Subscripts*

| | |
|---|---|
| c | critical point |
| f | fluid |
| mf | point of minimum fluidization |
| p | particle |
| o | limiting condition for small values of the independent variable |
| $\infty$ | limiting condition for large values of the independent variable |

*Superscipts*

| | |
|---|---|
| s | shifting parameter |

## Introduction

Fluidized bed reactors are widely employed in the chemical, petrochemical, metallurgical and pharmaceutical industries (Stein, Ding, Seville & Parker (2000)). Better understanding of the complex multiphase fluid and solid movement are essential for optimal reactor design. The powered addition technique serves as a method to correlated data in the transition region between two limiting conditions. This technique has got the possibility of a wide range of applications as described in the work by Churchill & Usagi (1947). Applying the technique to a fluidized bed traversing from a fixed to fluidize bed proved very useful. In general the shifting parameter, $s$, can be defined as follows

$$y^s\{q\} = y_o^s\{q\} + y_\infty^s\{q\}, \qquad (1)$$

where $y_o\{q\}$ and $y_\infty\{q\}$ represents the asymptotic solutions for large and small values of the superficial velocity, $q$, and $s$ is the shifting parameter. In fluidized beds the lower bound, $y_o\{q\}$, is described by drag models. Over the years numerous drag models have been proposed. In general two types of experimental data can be used to create a fluid-solid drag model (Syamlal, Rogers & O'Brien (1993)). The first type is with packed-bed pressure drop data expressed in the form of a correlation and the second is provided in the form of correlations for the terminal velocity in a fluidized or settling bed, expressed as a function of porosity and Reynolds number (Syamlal, Rogers & O'Brien (1993)). A well known example of a drag model based on the packed bed pressure drop data is the Ergun equation (Kunii & Levenspiel (1991)) and an example of a drag model using the terminal velocity correlation is the Syamlal O'Brien drag model (Syamlal, Rogers & O'Brien (1993)). It will be discussed later in the present study how these to basic formulations of drag models may influence the pressure drop predicted by these models in the fixed bed regime of a fluidized-bed reactor.

At minimum fluidization the total weight of the packed bed is supported by the upward force created by the gas moving upward through the porous structure. As the superficial velocity is increased above minimum fluidization velocity, the pressure drop remains practically the same (Kunii & Levenspiel (1991)). In some cases the pressure drop does not remain constant in the fully fluidized regime but actually increases. The explanation for the slight increase of pressure drop with an increase of superficial velocity may be attributed to wall effects which occurred due to the physical dimensions of the experimental tower used. More specifically, some slugging can occur and due to the formation of slugs additional potential energy is required to move the slug vertically. The result is an approximate linear increase in pressure drop across the fluidized bed (Chen, Gibilaro & Foscolo (1997)). In the present study the pressure drop in the fluidized regime will be assumed constant. This constant pressure drop will be assumed as the upper bound, $y_\infty\{q\}$, in our powered-addition correlation given in equation (1). At minimum fluidization velocity the pressure-drop is given by

$$\Delta p = (1 - \epsilon)(\rho_p - \rho_f)Lg, \qquad (2)$$

with $\rho_p$ the particle's density, $\rho_f$ the fluid density and $L$ the bed height.

In previous studies it has been found that the shifting parameter $s$ was relatively independent of the particle sizes that were investigated (Rautenbach, Melaaen & Halvorsen (2010)). The three particle size distributions that were used were 100-200 $\mu m$, 400-600 $\mu m$ and 750-1000 $\mu m$. It was found that a shifting parameter value greater than about 12 but smaller than about 20 produced an acceptable correlation in the transition region between the fixed to fluidized regime.

## Experimental set-up

The experiments that were carried out in the present study were performed at the TUC (Telemark University College) in Porssgrun Norway. A 1.5 $m$ long experimental fluidized bed reactor were used. The pressure drop data were acquired using a set of nine pressure probes located at different height along the bed. This set-up is presented in Figure 1. A porous plate distributor was used in this study to produce an uniform entry profile to the bed.
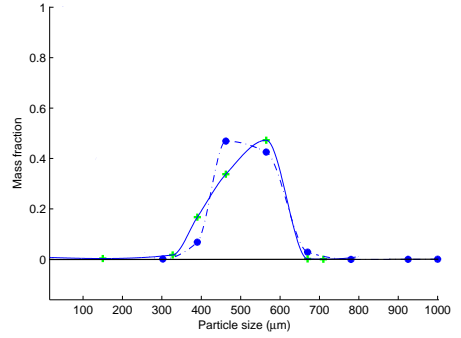
In the present study the influence of the particle density on this shifting parameter, $s$, was investigated. The two powders used were Zirconium Oxide (ZrO) and glass particles. Both were spherical particles with a size distribution of 400-600 $\mu m$. The particle size distributions are given in Figure 2. The void fraction of the beds as well as the minimum fluidization velocities and the particle densities are presented in Table 1. The void fractions refer to the void fractions after the bed has been fluidized. This void fraction will be used in calculating the predictions of the drag models in the fixed bed regime. Two mixtures of the ZrO-powder and glass powder were used to create a powder mixture with a different effective density than the two original powders. One mixtures consisted of one third ZrO-powder and two thirds glass powder. The other mixture was half-half ZrO-powder and glass-powder. The mean particle diameters presented in Table 1 are the *surface-volume mean* diameter and can be expressed as
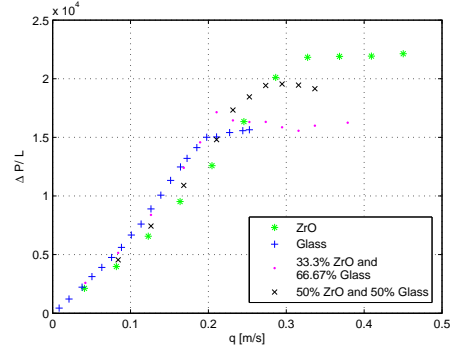
$$d_{p\ mean} = \frac{1}{\sum_i x_i/d_i}, \qquad (3)$$

2
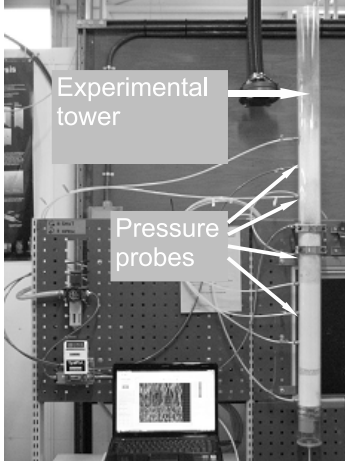
**Figure 1:** Experimental fluidization reactor equipped with nine pressure probes and fed through a porous plate distributer.



**Figure 2:** Particle size distributions for the *ZrO*-powder (-··-) and the glass powder (−).



**Figure 3:** Pressure-gradient against superficial velocity data for all the powders investigated.

where $x_i$ is the mass fraction of the particles with a diameter $d_i$. An estimation of the minimum fluidization velocity, $U_{mf}$, was determined by equating equation (2) with the pressure drop prediction of the Ergun equation (Kunii & Levenspiel (1991)). The intersection between these two predictions gives a fairly good correlation for $U_{mf}$. For the *ZrO*-powder the surface-volume mean diameter were used and for the glass particles the larges particle size (600 $\mu m$) were used as this gives the best correlation to experimental data using this particular intersection method. For both the *ZrO*-powder and the glass powder only the first term of the Ergun equation were used as this produced a good estimation of the minimum fluidization velocity. This approximation with the Ergun equation is usually only used with low superficial velocities or very small particles ($Re_{p,mf} < 20$) (Kunii & Levenspiel (1991)). This one term approximation of the Ergun equation did not give good enough correlations for the two mixture powders' minimum fluidization velocities and thus the total Ergun equation were used. The results are given in Table 1. For the mixture consisting of one third *ZrO*-powder a porosity of 0.38 were used and not the measured porosity of 0.42. This value is just the average value of the porosities of the original powders. This value of 0.38 was assumed to compensate for the suspected incapability of the drag models to compensate for the drag effect associated with segregation. This topic will be discussed later in the present work. In both of the mixtures' calculations of the minimum fluidization velocities an effective particle

size of 600 $\mu m$ were assumed as this produced an adequate result.

## Results

The pressure-drop data retrieved for the powders investigated are given in Figure 3. It is very clear to see that the higher density Zirconium Oxide (*ZrO*) produces a much larger pressure drop across the bed and also fluidizes at a higher value for the superficial velocity, $q$.

In the present study several drag model have been used to provide a pressure drop correlation in the fixed bed regime. Some of these models differ in the way that they have been derived but most of them make use of some sort of empirical basis. The models used in the present study was the well know Ergun equation (Kunii & Levenspiel (1991)), the Syamlal O' Brien drag model (Syamlal, Rogers & O'Brien (1993)) and the extended
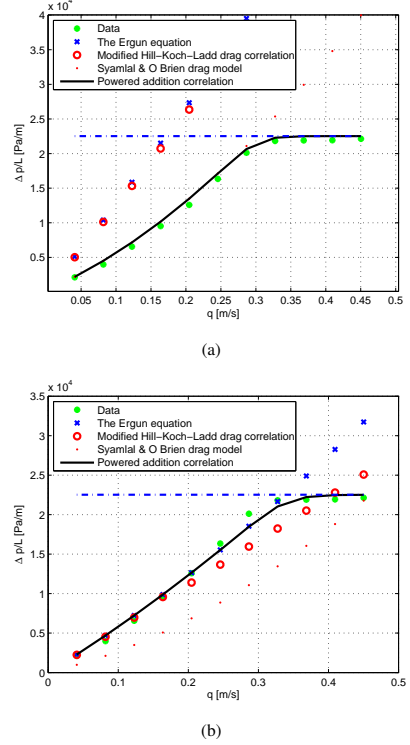
**Table 1:** Summary of particle- and bed properties.

| Variable | Value | Units |
|---|---|---|
| Zirconium Oxide | | |
| $\epsilon$ | 0.39 | - |
| $\rho_p$ | 3800.0 | kg/m$^3$ |
| $U_{mf}$ | 0.3 | m/s |
| $d_{p\,mean}$ | 503.29 | $\mu$m |
| Glass | | |
| $\epsilon$ | 0.37 | - |
| $\rho_p$ | 2500.0 | kg/m$^3$ |
| $U_{mf}$ | 0.21 | m/s |
| $d_{p\,mean}$ | 482.93 | $\mu$m |
| 33.3% Zirconium Oxide and 66.7% glass | | |
| $\epsilon$ | 0.42 | - |
| $\rho_p$ | 2933.33 | kg/m$^3$ |
| $U_{mf}$ | 0.24 | m/s |
| $d_{p\,mean}$ | 489.53 | $\mu$m |
| 50% Zirconium Oxide and 50% glass | | |
| $\epsilon$ | 0.38 | - |
| $\rho_p$ | 3150.0 | kg/m$^3$ |
| $U_{mf}$ | 0.25 | m/s |
| $d_{p\,mean}$ | 492.9 | $\mu$m |



(a)



(b)

**Figure 4:** Investigation of effective particle diameter on the different drag-model predictions with the *ZrO*-powder. Drag models with an effective particle diameter of (a) 400 $\mu$m and (b) 600 $\mu$m respectively.

Hill-Koch-Ladd drag correlation (Benyahia, Syamlal & O'Brien (2006)). In all of the Figures the limiting condition for large values of $q$ are represented by the dash-dot line (equation (2) is represented by (-·-)). These different drag models are represented in Figure 4 and 5 along side the pressure drop data acquired by using the *ZrO*-powder and glass-powder. For conciseness the models predictions are shown using the largest and smallest particle size of the distributions used. The mean value of the particle distributions were not used because it did not give good correlations in any of the cases investigated in the present study.

It is clear that the different models have varying accuracy with different values of the effective particle diameter. Previous research has found that in a fluidized bed, consisting of a particle size distribution, it is the smaller particle sizes that have the largest contribution (Jayarathna & Halvorsen (2009)). This followed from data that were collected by using different mixtures of particles. In the work by Jayarathna & Halvorsen (2009) it was found that only after about 40% of the mixture consisted of the larger particles did the minimum fluidization velocity differ considerably from the value for $U_{mf}$ found with just the smaller particles. Even after 40% of the bed consisted of large particles the minimum fluidization velocity was closer to the smaller par-

ticles minimum fluidization velocity than to the value for the larger particles (Jayarathna & Halvorsen (2009)). Given the data as represented in Figure 4 it seems that the Syamlal O' Brien drag model (Syamlal, Rogers & O'Brien (1993)) produces the best correlation at a particle diameter close to the smallest particle diameter in the range. This is in agreement with previous research (Jayarathna & Halvorsen (2009)) and from Figure 2 it is clear that there were some particles with a diameter even smaller than 400 $\mu$m. This fact makes the good correlation found with the Syamlal O' Brien drag model (Syamlal, Rogers & O'Brien (1993)) even more feasible as 400 $\mu$m is not necessarily the smallest particle size in the distribution.

In all the cases investigated the Ergun equation (Kunii & Levenspiel (1991)) and the extended Hill-Koch-Ladd
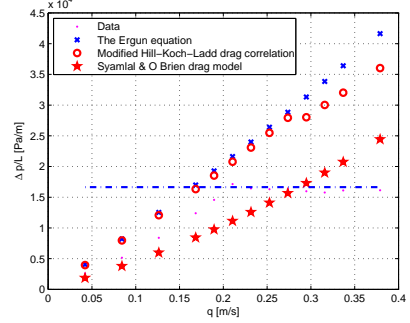
(a)



(a)



(b)
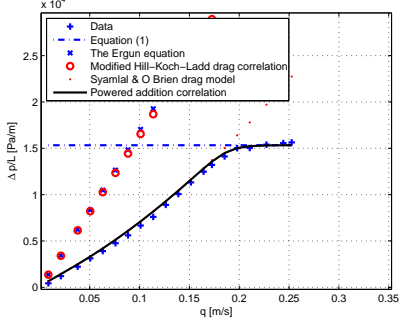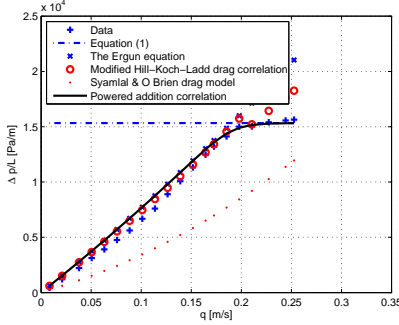


(b)

**Figure 5:** Investigation of effective particle diameter on the different drag-model predictions with just the glass powder. Drag models with an effective particle diameter of (a) 400 $\mu m$ and (b) 600 $\mu m$ respectively.

**Figure 6:** A mixture powder consisting of one third *ZrO*-powder and two thirds glass powder. Drag model comparisons to data assuming a particle size of (a) 400 $\mu m$ and (b) 600 $\mu m$.

drag correlation (Benyahia, Syamlal & O'Brien (2006)) corresponded to the larger particle size in the distribution. This result agrees with previous findings by de Wet, Halvorsen & du Plessis (2009). The results for the glass particles and mixtures are similar to that given in Figure 4 for the *ZrO* and are given in Figure 5 to 7.
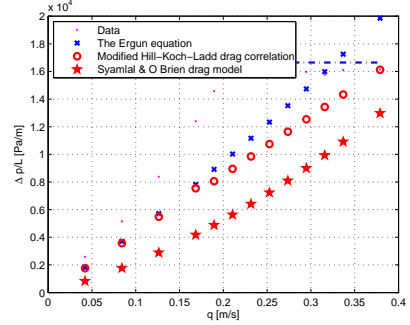
Results using powered addition. If we assume that the fully fluidized regime can be given by equation (2) then the following equation is produce using the powered addition technique

$$\frac{\Delta p}{L} = \left( Drag\ model^{-s} + equation\ (2)^{-s} \right)^{-\frac{1}{s}}, \quad (4)$$

were any adequate drag model can be used. The negative powers of $s$ is because the data is a decreasing power of $q$. The powered additioned results are depicted in Figure

4, 5 and 8. First the correlation is given when the Syamlal O' Brien drag model (Syamlal, Rogers & O'Brien (1993)) is used and a particle diameter equal to 400 $\mu m$ (Figure 4 and 5 (a)). Secondly the powered addition correlations are given using the Ergun equation and a particle diameter of 600 $\mu m$ (Figure 4 and 5 (b)). In all the cases a value of 15 was used as the shifting parameter although values with in a range from 12 to about 20 would have serviced. These results seem to indicate that the shifting parameter $s$ is insensitive to the density of the particles. In an attempt to confirm this suspicion the same correlations were made but now with the powder mixtures. In Figure 6 and 7 the correlation with the data are given with the larges and smallest particle sizes, namely 400 $\mu m$ and 600 $\mu m$ respectively. In both cases poor agreement were found between the drag models and the experimental data. In the case of the mixture

5

(a)



(b)
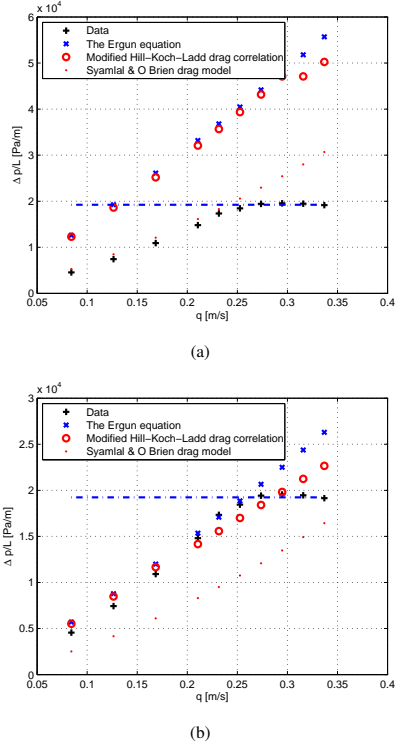
**Figure 7:** A mixture powder consisting of fifty percent
*ZrO*-powder and fifty percent glass powder.
Drag model comparisons to data assuming a
particle size of (a) 400 $\mu m$ and (b) 600 $\mu m$.

consisting of one third *ZrO* particles a relatively high
void fraction value is obtained as presented in Table 1.
This is considered a high value because the powders that
this mixture is made up of has void fractions below 0.4.
The main suspicion for this high value is due to segrega-
tion. The heaver *ZrO* particles can move to the bottom
of the tower while the lighter glass particles can move to
the top of the bed. As all of the drag models investigated
has got some sort of assumption of only one particle size
it is not a bad assumption that segregation could be the
cause of this discrepancy. Although most of the inves-
tigated models should cover all porosities they still did
not take into account the effect of particle size distribu-
tions and segregation. When a void fraction of about
0.38 was used (average void fraction of the base pow-
ders) for the powder consisting of one third *ZrO*, very
good correlations were found with the data as presented

in Figure 8. Much the same result as depicted in Figures
4 and 5. Thus the drag models predicted a more accurate
drag with a lower void fraction supporting the suspicion
that the drag models do not take into account the influ-
ence of segregation. The possible reason why the one
powder mixture formed some segregated effects and the
other powder mixture (50/50 mixture of glass and *ZrO*)
did not is explainable in light of initial fluidization. If
the superficial gas velocity, $q$, is slowly decreased af-
ter fluidization the heavy particles have time to settle to
the bottom while the lighter particles are force upwards.
Precaution was taken to avoid this, for example to close
the gas inlet quickly after fluidization, but this approach
is not guaranteed to always work equal effectively.

The aim of the present study is to investigate the shift-
ing parameter, *s*. To be able to do so a fairly accurate
prediction of the pressure drop in the fixed bed regime
is required. Thus a porosity of 0.38 will be assumed for
the mixture powder having a volume that consist of one
third *ZrO*. In Figure 8 the correlation using the powered
addition technique is given with the mixture powders'
pressure drop data. In both cases the Syamlal O' Brien
drag model (Syamlal, Rogers & O'Brien (1993)) were
used with a particle diameter of 400 $\mu m$. In both cases
a value of 15 were used for the shifting parameter, *s*. A
possible explanation for the discrepancy of the Syam-
lal O' Brien drag model (Syamlal, Rogers & O'Brien
(1993)) in the fixed bed regime of Figure 8 (b) be can
be because the smallest particle size in the distribution
range were used in the drag correlations and this particle
size is just an assumption. The characteristics of a par-
ticle bed seems to be mainly determined by the smaller
particles (Jayarathna & Halvorsen (2009)) but of course
the larger particles will also still have an effect on the
over all pressure drop. It is also possible that the mix-
ture's particle size distribution did not consist out of an
approximate bell-shaped curve but that there were more
of the bigger particles than in the other powders that
were investigated. A sieve analysis has to be performed
to confirm or disconfirm this hypothesis.

**Discussion**

Effective particle size is of great importance when work-
ing with a particle size distribution. In a lot of practical
applications fluidized beds consist of such powders. It is
clear from the results produced in the present study and
from results in previous work (Jayarathna & Halvorsen
(2009)) that the smaller particle sizes in the distribu-
tion plays a bigger role in the estimation of the drag.
More research is needed to find a better way of estimat-
ing the representative particle diameter for particle size
distributions. I seems clear from the present study and
from previous research done by de Wet, Halvorsen & du

(a)



(b)
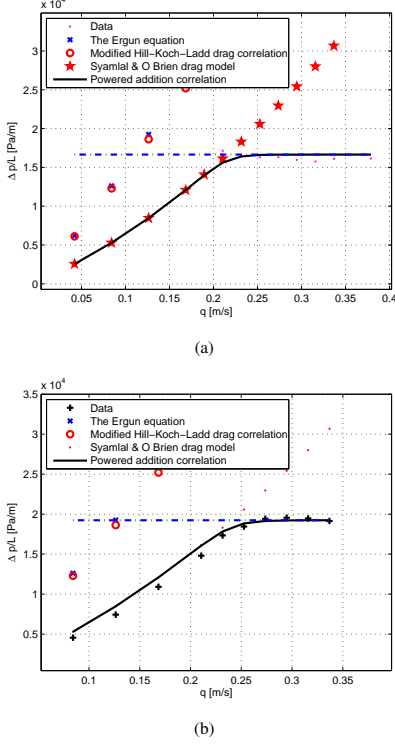
**Figure 8:** Powered addition correlation using the Syam-
lal O' Brien drag model (Syamlal, Rogers &
O'Brien (1993)) and a particle size of 400 $\mu m$
compared to (a) the mixture powder consist-
ing of one third *ZrO* and two third glass and
(b) the mixture powder consisting of fifty per-
cent *ZrO* and fifty percent glass.

Plessis (2009) that a normal average representative value
for the particle diameter is not appropriate. Using a par-
ticle size equal to 400 $\mu m$ together with the Syamlal O'
Brien drag model (Syamlal, Rogers & O'Brien (1993))
did however produce acceptable results.

In a case where data in the transition region is know a
different approach can be taken to calculate the shifting
parameter. At the point where the two asymptotes in-
tersect a critical value is obtained (de Wet, Halvorsen &
du Plessis (2009)). In the present study this point forms
an estimation for the minimum fluidization velocity with
the lower bound being a drag model and the upper bound
equation (2). This can also be expressed as

$$y_o\{q\} = y_\infty\{q\}. \qquad (5)$$

At this point equation (1) simply becomes

$$y_c^s = y_o^s + y_\infty^s = 2y_o^s = 2y_\infty^s, \qquad (6)$$

with $y_c$ the functional value at the critical point (de Wet,
Halvorsen & du Plessis (2009)). Solving for *s* produces
the following equation

$$s = \frac{ln\,2}{ln\,y_c - ln\,y_\infty} = \frac{ln\,2}{ln\,y_c - ln\,y_o}. \qquad (7)$$

Thus if the functional value $y_c$ is known a suitable value
for the shifting parameter, *s*, can be calculated.

The problem with this procedure is that in the indus-
try one usually wants to determine this transition regime
not prescribe it. As the physical meaning of the shift-
ing parameter is not known further research is needed to
describe the value for *s* more precisely.

A possible explanation for the high pressures pre-
dicted by the Ergun equation could be found in the man-
ner in which it was derived. It was derived on a fixed bed
model and then later adapted empirically using fixed bed
pressure drop data.

The inaccuracies of the Hill-Koch-Ladd drag correla-
tion (Benyahia, Syamlal & O'Brien (2006)) could prob-
able be based on the empirical way in which it was de-
rived. Singling out the exact cause for the over estima-
tion of the drag is not a trivial task.

It must be noted though that equation (2) did produce
a reasonable result with a particulated bed void fraction
equal to 0.42 in the case of the mixture consisting of a
third *ZrO*. This actually leads to the same suspicion that
the problem is mainly with the drag models in the case
of a segregated bed.

**Conclusions**

In fitting an appropriate curve the shifting parameter is
relatively insensitive as found by previous research (de
Wet, Halvorsen & du Plessis (2009)). A range of val-
ues produce an appropriate result. This range can be
anywhere between 12 and 20 but 15 was chosen in the
present study. The shifting parameter, *s*, seems to be in-
sensitive to changes in density. With all four powders
investigated a value of 15 serviced. Further research is
needed to determine the physical meaning of *s*, but it
seems that a value of 15 is a good estimation for the
shifting parameter in most practical application.

Thus an effective correlation is produced to give an
adequate prediction of pressure drop data for a fluidized
beds traversing from fixed to fluidized regime

**References**

Benyahia S., Syamlal M. and O'Brien T.J., Extension
of the Hill-Koch-Ladd drag correlation over all ranges

of Reynolds number and solids volume fraction, Powder Technology, Vol. 162, pp. 166-174, 2006

Chen Z., Gibilaro L.G. and Foscolo P.U., Fluid pressure loss in slugging fluidized beds, Chemical Engineering Science, Vol. 52, No. 1, pp. 55-62, 1997

Churchill S.W. and Usagi R., A Standardized procedure for the production of correlations in the form of a common empirical equation, Ind. Eng. Chem. Fundamen., Vol. 13(1), pp. 39-44, 1947

de Wet P.D., Halvorsen B.M. and du Plessis J.P., Powered addition applied to the fluidization of a packed bed, Computational methods in Multiphase flow V Paper 431-441, WITPress (UK), 2009

Jayarathna C. and Halvorsen B.M., Experimental and computational study of particle minimum fluidization velocity and bed expansion in a bubbling fluidized bed., SIMS 50 conference, Fredericia, Denmark, October 2009

Kunii D. and Levenspiel O., Fluidization Engineering, Second edition, Butterworth-Heinemann (USA), 1991

Rautenbach C., Melaaen M.C. and Halvorsen B.M., Investigation of the shifting-parameter as a function of particle size distribution in a fluidized bed traversing from a fixed to fluidized bed., Fluidization XIII: New Paradigm in Fluidization Engineering conference, Hotel Hyundai, Gyeong-ju, Korea, May 2010

Stein M., Ding Y.L., Seville J.P.K. and Parker D.J., Solids motion in bubbling gas fluidized beds, Chemical Engineering Science, Vol. 55, pp. 5291-5300, 2000

Syamlal M., Rogers W. and O'Brien T.J, MFIX Documentation theory guide, Technical note, U.S. Department of Energy, Office of Fossil Energy, Morgantown Energy Technology Center, Morgantown, West Virginia, December 1993

# Paper E

# The influence of the experimental span of Time-resolved X-ray tomography on dynamic parameters in a fluidized bed.

# The influence of the experimental span of Time-resolved X-ray tomography on dynamic parameters in a fluidized bed

**C. Rautenbach[1], R. F. Mudde[3], M. C. Melaaen[1,2], B. M. Halvorsen[1,2]**
[1]Department of Process, Energy and Environmental Technology, Telemark University College, Porsgrunn, Norway.
[2]Telemark R & D Centre (Tel-Tek), Porsgrunn, Norway.
[3]Kramers Laboratorium voor Fysische Technologie, Delft University of Technology, Delft, The Netherlands

*Keywords:* Fluidization, X-ray tomography, Experimental-span, Bubbles size, velocity and frequency

**Abstract —** Fluidized beds have presented some problems to experimentalists in the past due to their opaque nature [1]. This problem has however been overcome by non-intrusive nor invasive measurement techniques. X-rays or Gamma rays can move through such systems where light (low energy radiation) cannot. Tomographic techniques can thus also be used with nuclear methods and is generally referred to as nuclear densitometry [1].

Using Time-resolved X-ray tomography on a fluidized bed is a state of the art technique. The first data of such a system has been presented by [1]. With this technique being novel, a thorough investigation of the measurement scenarios has not been performed thus far. The current study will focus on the influence of the experimental span on the average bubble velocity, bubble frequency and bubble volume. The influence of thresholding was investigated and the accuracy of the obtained results will be determined by existing empirical equations. In all of the experiments, glass particles were used with a particle size distribution of 79-149 μm.

In the present study the bed was fluidized using a single central jet and a porous plate distributer. This experimental set-up was chosen to make the study of the dynamic parameters more reliable and to include the uncertainties associated with a freely bubbling bed. The measurement technique is briefly discussed and it is concluded that at least 45 s is required to obtained a reliable result for the bubble velocity in a freely bubbling bed while at least 25 s are required to obtain reliable results for the bubble volume and frequency.

## INTRODUCTION

Fluidized bed reactors are currently being used in a wide range of industrial applications. Some applications are still in development (like Chemical Looping Combustion (CLC)) and others have been used successfully for decades (for example catalytic reactors). The development of state of the art measuring techniques helps researchers to understand the complex multiphase flow behaviour of fluidized beds and thus enables the research community to better design and utilize fluidized bed technology. One such state of the art measuring technique is Time-resolved X-ray tomography.

Currently there are several tomographic systems being used in process technological research. These systems include Electrical Capacitance Tomography (ECT), Electrical Resistance Tomography (ERT) and X-ray Tomography. Using these measuring techniques an opaque

system, like a fluidized bed, can become transparent [1]. X-rays, Gamma rays, Electrical fields and current can move through such systems where light (low energy radiation) cannot. Tomographic techniques can thus also be used with nuclear methods and is generally referred to as nuclear densitometry [1]. Techniques like ECT and Electrical Impedance Tomography (EIT) operates with soft fields. These soft field techniques operates on the principal that a change in the electromagnetic field at one location influences the entire field [1]. The draw back of such techniques is typically that the size of the experimental tower is limited.

Nuclear tomographic techniques or nuclear densitometry relies on hard fields and does not have the same sort of constraints the soft field measuring systems have. An example of a hard field measuring technique is X-ray tomography. Thus larger tower diameters can be studied without the loss of resolution in the center of the tower. These nuclear measuring techniques have the added disadvantage of being dangerous and expensive compared to other techniques. Special lead insulated room or facilities are required together with advance safety protocols and regulations. There is always some inherent noise associated with nuclear techniques and because of this the temporal resolution is relatively low compare to some of the other tomographic modalities [1].

The time-resolved X-ray tomography system used in the present study is located at the Technical University of Delft (TU Delft) in the Netherlands. The measurements obtained using this system together with Digital Image Processing (DIP) package produced by the Quantitative Imaging Group from TU Delft, made it possible to create 3D images of bubbles encountered in a fluidized bed. These 3D images also provide information about the recorded bubbles, such as the bubble volume, frequency and location. In Figure 1 (a) a typical 3D image is provided collected over a 1.6 s time interval. In Figure 1 (b) an image is provided before it was processed into a three dimensional form. These 2D images are staked to create the 3D image shown in Figure 1 (a).



| (a) | (b) |
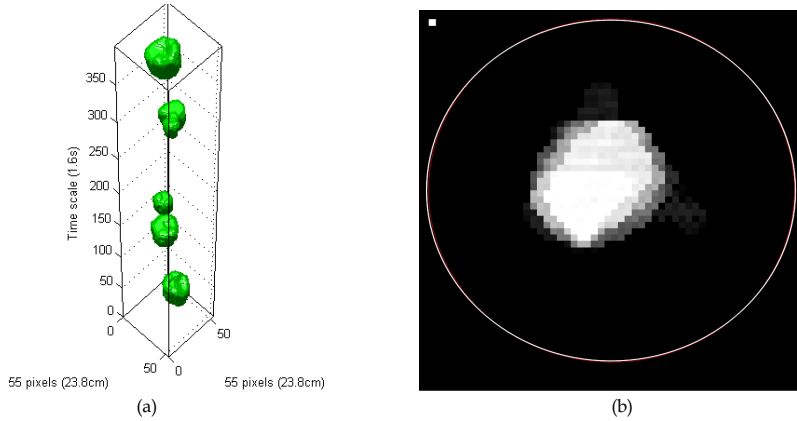
**Figure 1**: (a) 3D-image of bubbles rising in a fluidized bed with a 55×55 pixel resolution. (b) A typical 2D grayscale 'slice' image of a bubble rising in a fluidized bed. The white line indicates the experimental tower and at the top left corner the size of a single pixel is illustrated.

To be confident in the results obtained from the time-resolved X-ray tomography system it is important to investigate several measuring scenarios and the reliability of the results under typical operating conditions [3]. This was done in the present study with the focus on the experimental span and its influence on the dynamic parameters of a fluidized bed.

## EXPERIMENTAL PROCEDURE

### Experimental Setup

In the measurement system used in the present study three X-ray sources were used that each created a fan beam through the fluidized bed. Each fan beam fell onto two array detector

consisting of 32 CdWO$_4$ detectors [1]. The set-up used in the present study is illustrated in Figure 2. The red lines represent the path of radiation detected by each detector respectively. The fluidized bed is located in the middle of the set-up, surrounded by the detectors and sources and its diameter was 23.8 cm. Figure 2 was created by a simulation program developed by Mudde and co-workers at TU Delft.
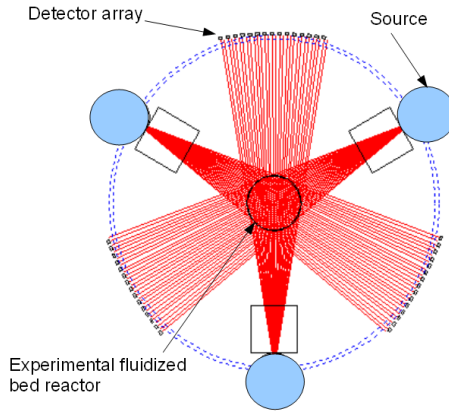


**Figure 2**: Three X-ray sources that simultaneously radiate an X-ray fan beam through the experimental fluidized bed tower or reactor.  Two sets of 32 detectors have been allocated to each source.

The X-ray system can have a sampling frequency of 2500 frames/s but due to some inherent noise in the X-ray sources the obtained data had to be averaged. This was done by averaging over ten measurements which in turn lowered the sampling frequency to 250 frames/s. This averaged data can be converted to a line-averaged solid fraction value by using calibration curves [1].

The TU Delft X-ray tomography system consists of two arrays of detectors 4 cm apart and both consisting of 32 detectors for each of the 3 sources.  The distance from the center of the bed to the detector arrays was 85.8 cm and the distance from the center of the bed to the sources was 71.6 cm. All of the X-ray beams originate from an approximate point source and diverges from there. Thus the effective distance between the measuring planes can be shown to be equal to 1.86 cm . With these two measuring planes it was possible to determine the bubble rise velocity. Bubble size and velocity are crucial in determining factor such as the particle residence time, particle entrainment and heat and mass transfer in a fluidized bed [2].  Thus to be able to determine the bubble shape, size and velocity is of paramount importance and the X-ray tomographic system allows researchers to do exactly that.

All the experiments were carried out with a 79-149 µm glass powder that produced a solid fraction value of 0.66 in the packed bed (non-fluidized) state. The experimental tower was made from plexi-glass and ambient air was fed into the bed by either a single jet or via a porous plate distributor. The jet was used as a validation method together with hollow plastic cylinders of different sizes. Measurements of these two scenarios produce predictable results and are a good way to test the system before dealing with the uncertainties associated with freely bubbling beds.

In Figure 3 the experimental tower used in the present study is illustrated. For the experiments done with the single jet the air was not fed through the porous plate and vice versa. During the investigation two different sizes of plastic cylinders (we shall call the phantoms) were inserted at several locations within the fluidized bed. It was found that the resolution in the center of the bed was worse than at the area close to the walls. The explanation for this

phenomena lies within the high attenuation of the glass particles. Because the center beams have to pass through a lot of material close to the center of the bed, more radiation is attenuated, compared to the short path length attenuation close to the tower walls.
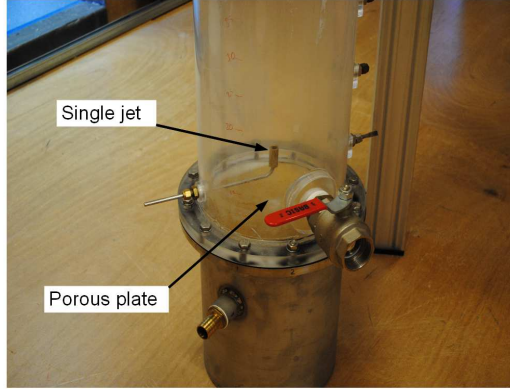


**Figure 3**: Experimental tower used in the present study equipped with a single jet and a porous plat distributer.

The radiation levels can readily be increased to 'see' more in the center of the bed but this will lead to the very real possibility of over exposing the detectors aligned with the short path lengths. The solution could be to place copper plates in front of the side detector in unison with increasing X-ray energy. Unfortunately this solution has not yet been applied for the present work and thus the spatial resolution at the center of the tower is just above 2.5 cm.

**Calibration**

Each detector measures the attenuation of a small cone shaped beam coming from the X-ray source located on the opposite side of the fluidized bed. This small cone is approximated as a line and treated as such in the reconstruction [1]. For mono-energetic gamma- or X-rays passing through a fluidized bed, the number of photons registered per second in a single approximated line will follow the Lambert-Beer law which states that

$$R = R_0 \exp\bigl(1\bigl(\phi_s \mu_p + (1 - \phi_s)\mu_g \bigr)d_t \bigr),$$  (1)

where $R_o$ is the number of photons detected per second in a vacuum including the fluidized bed wall, $\phi_s$ is the solid fraction and $\mu_p$ and $\mu_g$ is the linear absorption coefficient for the solid and gas phase respectively. $d_t$ is the inner diameter of the fluidized bed tower [1].

For a mono-energetic source a two point calibration would be sufficient. This would be calibration much like that of an ECT system with an empty tower and a full tower of particles. Most X-ray sources produce a wide spectrum of X-ray energies and thus a two point calibration is not adequate [1]. This implies that $\mu$ is a function of the photon energy $E$. Non-linearity is also obtained due to the fact that the low energy photos are absorbed much faster than high energy photons. Hence, $R$ (measured number of photons) does not follow the Lambert-Beer law [1]. During calibration the effect of 'beam hardening' has to be accounted for. Beam hardening occurs as an increasing amount of powder is present on a particular X-ray beam and the relative number of high-energy photos increases [1]. To account for this effect each detector is calibrated individually with several amounts of powder. Seven calibration points are usually used in total including an empty and full tower as the two extreme values [1]. In the current study a five point calibration has been used due to the high attenuation of glass particles in comparison to that of polystyrene particles. If seven points were used, including an empty bed, the radiation

would have been to low to get meaningful measurements. Our calibration thus entailed the center beams passing through 1/3, 1/2, 2/3, 5/6 of a full bed and a full bed. Using these calibration points the radiation level could be set high enough as to obtain meaningful measurements but also low enough as to not over expose the detector and thus avoid the detector from clipping. These criteria were chosen under the assumption that there won't be any bubbles, during the course of the experiments, with an effective diameter much greater than 2/3 of the tower diameter.

In Figure 4 (a) an example of a calibration curve is provided. A calibration curve was produced for each detector of all three double plane detector arrays. For each calibration curve three constants were determined, namely: $A_{cal}$, $B_{cal}$ and $C_{cal}$. These constants determined the calibration curve of the form

$$A_{cal} + B_{cal} \times \exp\left(- x/C_{cal}\right),$$ (2)

where $x$ is the path length of a particular beam through the particles aligned with a particular detector [1]. This exponential curve is also illustrated in Figure 4 (a) and its only purpose is to provide a relationship between particle path length and measured attenuation. It is important to remember that the attenuation of the radiation is only a function of the amount of powder on its path [1]. In calculating these calibration values 5 s of measured attenuation values were collected for each detector array. Then these 1250 values were averaged for each detector to produce the representative measured attenuation values for each detector and for each calibration point.

Before the actual measurements were made a segment of data were taken where no bubbles were present and it was then compared to the full undisturbed bed data obtained from calibration. In theory the ratio of these averaged detectors measured attenuations should be equal to 1 if the calibration is working properly. In Figure 4 (b) it is clear that this was not the case.
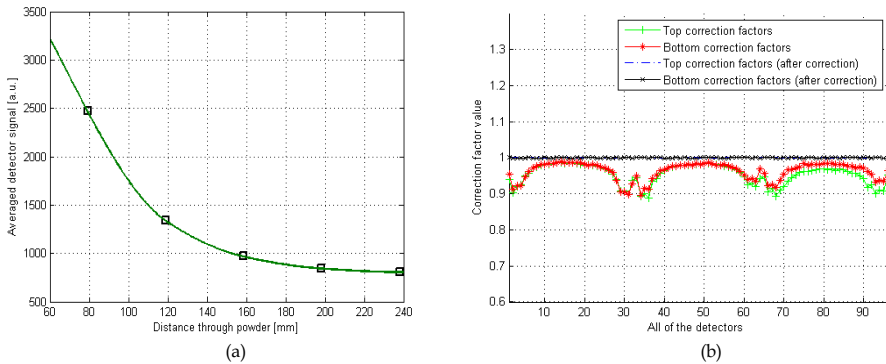


**Figure 4**: (a) An example of 5 calibration points for the 16th detector of one of the three top detector arrays. (b) Correction factors for all of the detectors (3×32 detectors) before and after applying the correction factor.

From Figure 4 (b) it is clear that for each of the three detector arrays a near parabolic-shaped discrepancy is obtained. This might be due to the motion of particles in the fluidized bed after fluidization and the consequent redistribution of particles. The powder used in the present study has a large particle size distribution and thus a non-uniform particle distribution can be expected and was observed in the actual experiments. The correction factors obtained in Figure 4 (b) were used to correct all the collected data to account for these effects associated with the fluidization of the bed. In Figure 4 (b) the same ratios are also shown after it has been corrected with the correction factors.

# RESULTS AND DISCUSSION

## Thresholding

As part of the measurement scenario of most tomographic measurements in fluidized beds, a threshold has to be assigned to define the bubble size. The threshold value can range from 0 to 1 and the closer the value is to 0 the bigger the measured bubble will be (refer to Figure 1 (b) where a typical greyscale image was illustrated with 1 indicating white and 0 black). To get a reliable value of the threshold value the phantoms could be used as these cylindrical objects had a known diameter and thus the threshold could be adjusted accordingly. Although this should be quite reliable the plastic wall of the phantom might create a situation that is not representative of the actual fluidized bed bubbles.

Thus instead of using the phantoms, a predictive correlation was used to estimate the average bubble size. According to a literature review done by Karimipour and Pugsley [2] the most reliable correlation for bubble size prediction of Geldart **B** particles are given by Choi et al. and the trivial correlation of Mori and Wen [2]. The performance of the correlations investigated by Karimipour and Pugsley were quantified by calculating the squared difference between the correlation prediction and experimental values collected from several published results [2]. The equation by Mori and Wen was used in the present study due to its simplicity and prediction accuracy and is given as

$$\frac{d_{bm} - d_b}{d_{bm} - d_{b0}} = e^{-0.3z/d_t} \quad [\text{cm}], \tag{3}$$

where $d_{b0}$ is the initial bubble size formed near the bottom of a bed supported by a porous or perforated plate distributer [2, 4]. $d_b$ is the equivalent diameter calculated from a sphere with the same volume as the average bubble volume of a particular experiment, $z$ is the bed height at which the measurements are taken and $d_t$ is the experimental tower diameter. $d_{bm}$ is known as the limiting bubble size in a very deep bed and is expressed as

$$d_{bm} = 0.65\left(\frac{\pi}{4} d_t^2 \left(u_0 - u_{mf}\right)\right)^{0.4} \quad [\text{cm}], \tag{4}$$

with $u_0$ the superficial velocity and $u_{mf}$ the minimum fluidization velocity [4]. The range of conditions from which equation (4) was formulated contains the present study. According to Karimipour and Pugsley [2] the equation most researcher use to estimate the initial bubble size, $d_{b0}$, formed near a porous plate distributer is given by Miwa et al. and is expressed as

$$d_{b0} = 0.00376\left(u_0 - u_{mf}\right)^2 \quad [\text{cm}]. \tag{5}$$

Given that the measurements were taken at a height of 46.2 cm in the fluidized bed and that $u_0 - u_{mf} = 5.1$ cm/s, a bubble size of 6.4 cm was predicted. Using 50 s of data collected with an experiment conducted under the same operating conditions and using a porous plate distributer the average bubble volume could be calculated. Then the threshold value was changed until an average bubble volume was obtained that produce an equivalent diameter approximately equal to 6.4 cm. A threshold value of 0.465 was found to accomplish this and was then used as the threshold value for the remainder of the experiments.

**Experimental span**

Previous research performed with other tomography modalities suggests a strong dependence on the experimental span [3]. Makkawi and Wright investigated the experimental span over a whole range of different operating condition using an ECT system [3]. According to their literature study there was no thorough investigation into a measurement scenario for an ECT system prior to their research. Because of this reported strong dependence of the dynamic parameters on the experimental span for the ECT system, a thorough investigation regarding the dependence of the bubble velocity, volume and frequency on the experimental span for the time-resolved X-ray tomography system was performed in the present study. The present study will provide future researchers a guide for planning and designing a reliable experimental measuring scenario using the time-resolved X-ray tomography system.

**Influence of the experimental span on the average bubble velocity**

The bubble velocities were determined by using the two planes of the X-ray system. Using the two planes, with a known distance between them, it was possible to trace the bubbles from one plane to the next and thus measure the time it took for a particular bubble to ascend from the lower plane to the top plane. An example of the range of bubble velocities recorded in a single experiment is provided in Figure 5. This data was obtained with a freely bubbling bed using a porous plate distributer. The data was recorded over a 50 s period and this time limit will form the maximum experimental time span in the present study.
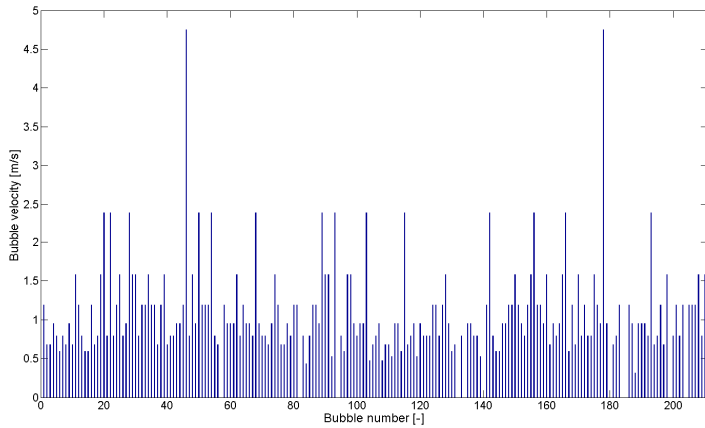


**Figure 5**: Example of bubbles recorded during a 50 s experimental run together with their measured bubble velocities. For this experimental scenario $u_0 - u_{mf} = 5$ cm/s.

The average bubble velocity over the particular experimental span will be used to investigate the influence of the experimental span on the bubble velocity. In Figure 6 the bubble rise velocity is given as a function of the experimental span for both fluidization via a single jet and via a porous plate distributer.

From Figure 6 (a) it is clear that the bubble rise velocity for a single jet remains nearly constant after 40 s with an error less than 5 %. Thus it seems safe to conclude that the bubble rise velocity of a single jet can be reliably determined after an experimental span of only 40 s. The same could not be concluded from Figure 6 (b) where the bed was fluidized via a porous plate distributor. With this freely bubbling bed at least 45 s was required to obtain a reliable result with an error less than 8 %. Although the bubble velocities in Figure 6 (b) stabilized after 45 s the values obtained for the excess velocity equal to 3.6 cm/s were higher than the values obtained with the 4.3 cm/s.

(a) (b)
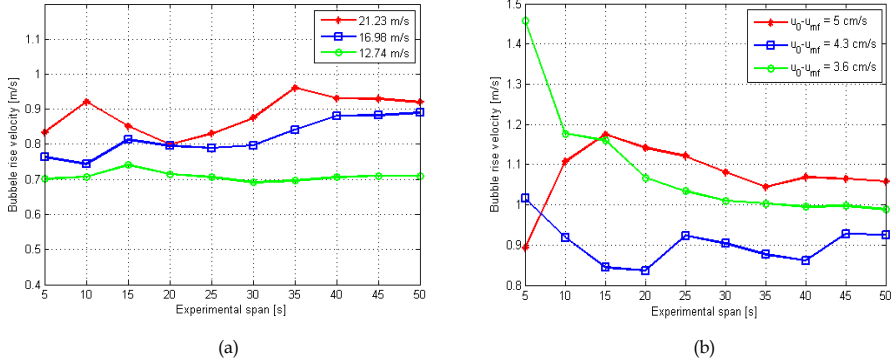
**Figure 6**: (a) The average bubble rise velocity computed over each experimental span for three different superficial jet velocities through a single jet at the bottom of the fluidized bed. (b) The bubble rise velocity as a function of the experimental span for three different excess gas velocities, fluidized via a porous plate distributer.

This is a highly counter intuitive result as smaller bubbles should rise slower according to most bubble velocity correlations. The explanation for the phenomena can be explained by mean of Figure 7.

In Figure 7 (a) the location of the bubble center is given in the form of the sample number at which it was recorded. The bubble volume is represented in pixels cubed (the unit before it is transformed into SI units). From Figure 7 (a) it is observed that the bottom plane data always supersedes the top plane data. This is trivially correct as the bubble must pass the bottom plane before it passes the top plane. The encircled data points indicate bubble that has been match as being the same bubble traversing from the bottom to the top plane. The problem can be observed in the data points that were not 'matched'. From visual observation of the reconstructed data it was concluded that some of the smaller bubbles were not reconstructed correctly and were in the range below the resolution of the current time-resolved X-ray tomography system. This could have caused the bubble rise velocity measurements to be bias towards the higher velocity bubbles.



(a) (b)
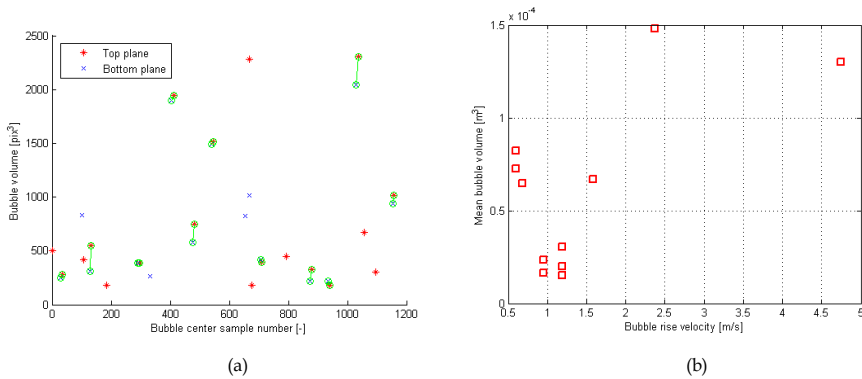
**Figure 7**: (a) Bubbles recorded during the first 5 s of the experiments done where the bed was fluidized through a porous plate with an excess gas velocity equal to 3.6 cm/s. The encircled data points indicate bubbles that matched from both the top and bottom plane. (b) Bubble volume as a function of the bubble rise velocity for the same 5 s experiment.

In Figure 7 (b) the bubble volume is given as a function of the bubble rise velocity. The bubble volume was calculated from taking the average volume between the bottom and the top plane.

From Figure 7 (b) it is clear that larger bubbles do not necessarily imply a larger bubble rise velocity although over an average this will be the expected result.

### Influence of the experimental span on the average bubble volume

In Figure 8 the average bubble volume is given as a function of the experimental span. Both a jet and a porous plate were used and the results are provided. The volume of each bubble was computed with the bubble rise velocity of that particular bubble. The results obtained for the average bubble volume had a more stable behaviour over a shorter time in comparison to that of the bubble rise velocity. For the experiments done with the single jet, Figure 8 (a), an experimental span of 45 s produces results with less than 2 % error and for an experimental span of only 20 s an error of less than 6 % is achieved. Thus if 6 % error is adequate for a particular application an experimental span of 20 s can be used with a reliable result.

For the experiments done with the porous plate distributer, Figure 8 (b), an experimental span of 25 s produces errors less than 7 % for all the investigated cases.



(a)                                         (b)
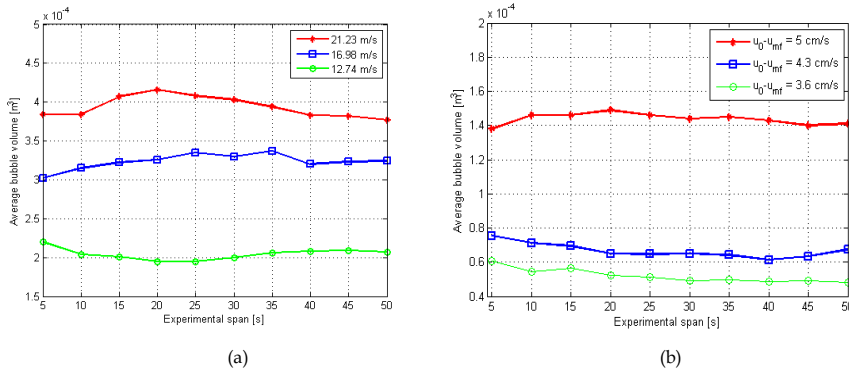
**Figure 8**: (a) The average bubble volume for three different superficial jet velocities through the single jet. (b) The average bubble volume for three different excess gas velocities through a porous plate distributer.

The data presented in Figure 6 and 8 were collected from the same experiments. Note that even though the average bubble volume in Figure 8 (b) decreased with a decreasing excess gas velocity the bubble rise velocity did not follow the same trend (as discussed previously using Figure 7).

### Influence of the experimental span on the bubble frequency

In Figure 9 the bubble frequency as a function of the experimental span is provided for using both a single jet and a porous plate distributer. In the single jet experiment an experimental span of 20 s produced an error of only 4 % and with the porous plate distributer a 25 s run produced an error of 5 %.

Similar to the average bubble volume results the bubble frequency requires less time per experiment to reach a reliable result. In Figure 9 (a) the bubble frequencies with a 21.23 m/s superficial jet velocity were lower than the 16.98 m/s superficial jet velocity data. It is known that slug flow behaviour will have the effect of lower bubble rise velocities [4]. Thus it is not that surprising that the 21.23 m/s superficial jet velocity could have caused near slug flow conditions and thus had the effect of larger, less frequent, bubbles or slugs.
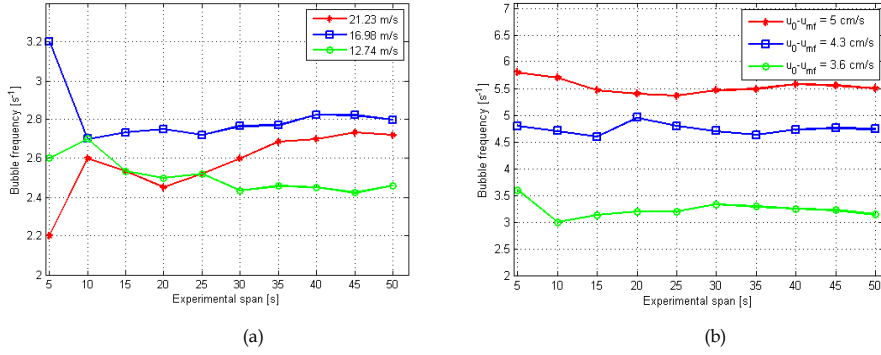
**Figure 9**: (a) The bubble frequency for three different superficial jet velocities using a single jet. (b) The bubble frequency for three different excess gas velocities using a porous plat distributer.

The largest bubble in the 21.23 m/s superficial jet velocity experiments reached a size of approximately 40 % of the tower diameter. The accepted size for a bubble to be classified as a slug is usually 50 % of the tower diameter [4].

## CONCLUSIONS

Some dynamic parameters of a fluidized bed have been investigated as a function of the experimental span. These parameters were the bubble rise velocity, the average bubble volume and the bubble frequency. Several different superficial gas velocities were also used to investigate the effect of the experimental span on these particular dynamic parameters. In previous research done on this topic, but with an Electrical Capacitance Tomography system (ECT system), it was found that a minimum experimental span of 60 s must be used to obtain reliable results [3]. The dynamic parameters that [3] investigated were the bubble rise velocity and frequency. For measuring the solid fraction [3] found that 20 s will produce a reliable result.

For the time–resolved X-ray tomography system investigated in the present study different results were obtained. In using a single jet it was found that a measuring span of 40 s produced reliable results for the bubble rise velocity. In the case of the average bubble volume and bubble frequency a 20 s experiment produced reliable results with using the single jet. In using the porous plate distributor a measuring span of 45 s were adequate for determining the bubble rise velocity while 25 s were reliable enough for the average bubble volume and bubble frequency. From using empirical equations it was also estimated that a threshold value of 0.465 will produce result that most agree with previously estimated correlations.

The present study forms part of exploring the capabilities of the time-resolved X-ray tomography system and functions as a user manual for future researchers [3].

## ACKNOWLEDGMENTS

**REFERENCES**

1.  Mudde, R.F.  2010.  Time-resolved X-ray tomography of a fluidized bed.  *Powder Technology*. **199**:55–59.

2.  Karimipour, S. & Pugsley, T.  2011.  A critical evaluation of literature correlations for predicting bubble size and velocity in gas-solid fluidized beds.  *Powder Technology.* **205**:1-14.

3.  Makkawi, Y.T. & Wright, P.C.  2004.  Electrical capacitance tomography for conventional fluidized bed measurements-remarks on the measuring technique.  *Powder Technology.* **148**:142-157.

4.  Kunii, D. & Levenspiel, O.  1977.  *Fluidization Engineering*.  Huntington, NY: Robert E. Krieger Publishing Company.

# Errata

In Paper E there was a typo. Equation (1) should have been expressed as

$$R = R_0 \exp\left(-\left(\phi_s \mu_p + (1 - \phi_s)\mu_g\right) d_t\right). \tag{E.1}$$

The minus in the exponent was miss typed as a 1 in equation (1).

It might be useful to express the jet flow in terms of the superficial velocity. The single central jet had a diameter of $1cm$. Using this information the superficial velocity can be calculated if desired.

# Paper F

# A comparative study between Electrical Capacitance Tomography and Time-resolved X-ray tomography.

# A comparative study between Electrical Capacitance Tomography and Time-resolved X-ray tomography.

C. Rautenbach[a,*], R. F. Mudde[b], X. Yang[b], M. C. Melaaen[a], B. M. Halvorsen[a]

[a]*Department of Process, Energy and Environmental Technology, Telemark University College, Porsgrunn, Norway.*
[b]*Kramers Laboratorium voor Fysische Technologie, Delft University of Technology, Delft, The Netherlands.*

## Abstract

Modern day tomographs enable the research community to investigate the internal flow behaviour of a fluidized bed by non invasive methods that partially overcome the opaque nature of a dense bubbling bed. Each tomographic modality has its own limitations and advantages and in the present study two modern day tomographic systems were evaluated with respect to their performance on a cold dense fluidized bed. The two tomographs investigated are an Electrical Capacitance Tomography (ECT) tomograph and a time-resolved X-ray tomography tomograph. The study was performed on spherical glass particles with various particle size distributions that could mainly be classified as Geldart B or D particles. Two experimental towers were employed, one with a diameter of $10.4 cm$ and the other $23.8 cm$ while compressed air was used as fluidizing fluid during all of the experiments.

Results obtained with both systems are provided in comprehensive figures and tables and some first results are obtained with the time-resolved X-ray tomography system. The bubble size measurements of both tomographs are compared with several theoretical correlations via the root mean square error of the predictions (RMSEP). With the results it was also concluded that a small amount of small particles can noticeably alter the fluidization hydrodynamics of a powder. The bubble frequencies are also presented to aid in understanding the hydrodynamic behaviour of the powders investigated. A comprehensive summary of the two tomographic modalities is also provided.

*Keywords:* Bubble size, Fluidization, Comparative study, Electrical Capacitance Tomography (ECT), X-ray Tomography

## 1. Introduction

Fluidization engineering has the potential to play an important role in a sustainable future with applications in chemical looping combustion (carbon capture), recovery of valuable materials from waste streams and biomass gasification [1]. Being such a promising technology for a greener tomorrow it is important to understand these reactors with the highest possible degree of accuracy. With this aim, different measurement systems have been utilised during the history of fluidized beds [2, 3]. Positive features of fluidized beds include temperature uniformity, moderate pressure drops and the possibility of continuously adding and removing particles [1].

The main challenge faced with measuring flow behaviour in dense fluidized beds, is their opaque nature. Measurement techniques related to fluidized beds can be divided in two general categories according to Karimipour and Pugsley [4], namely: probes and photography/imaging. Probes have received criticism because they tend to interfere with the internal flow behaviour of the bed. This interference decreases with a decreasing probe size [4].

Bubbles behave differently in 2D and 3D beds according to Geldart [4] and thus 3D measurement techniques are needed. For accurate measurements, 3D information is important to fully and accurately describe the flow behaviour (such as bubble coalescence) of the bed [4]. The development of Computational Fluid Dynamics (CFD) over the last century has aided significantly in understanding the complex flow behaviour of fluidized bed reactors but these simulations still requires verification via reliable experimental methods.

A measurement technique that is probably better known for its medical applications is the use of tomography. Some of the tomography systems (tomographs) currently available are $\gamma$-ray transmission tomography [3], Electrical Capacitance Tomography (ECT) [5], Electrical Resistance Tomography (ERT) [6], Magnetic Resonance Imaging (MRI) [7] and X-ray tomography [8]. A tomographic image (tomogram) can be generated via a variety of methods and they all produce some form of two dimensional sliced image through the investigated object. The slices can then be placed together to form a three dimensional temporal or spatial image. In Figure 1 an example is illustrated where a 3D spatial image is produced. This data were obtained using a Magnetic Resonance Imaging (MRI) system.

An example of temporal tomographic images is given in Figure 2 where several measurements taken with an Electrical Capacitance Tomography (ECT) tomograph are illustrated. These images are separated by time and if they are stacked they will form a temporal 3D image. Such images can be converted into spatial images with the use of velocity information.

Three dimensional information can also be obtain from the viewpoint of a single particle using techniques such as Positron

*T: +47 3557 5222
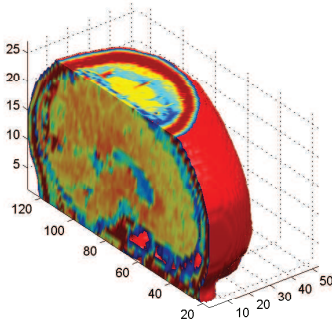*Email address:* `christo.rautenbach@hit.no` (C. Rautenbach)

Figure 1: Spatial 3D MRI image of the human brain. This image was produced using the commercial software MATLAB and the MRI data was obtained from the MATLAB-examples data base.

Emission Particle Tracing (PEPT) systems [9, 10]. The present study will only focus on tomographs. The two tomographs investigated in the present study are the ECT and the time-resolved X-ray tomography system.

The aim of the study is to present these two tomographic modalities in such a way that researchers can make an informed choice when it comes to choosing a tomograph. The bubble size data from both tomographs are also compared to existing correlations to evaluate which correlations agree most with the obtained data.
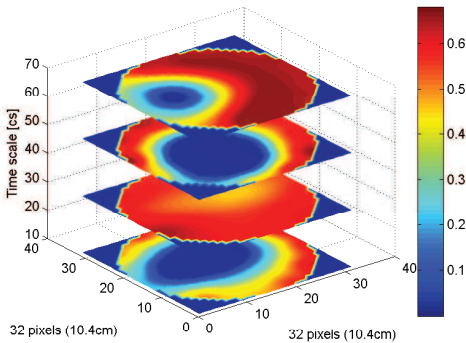


Figure 2: Four tomograms capture with a 12 electrode Electrical Capacitance Tomography (ECT) system. The images indicate a bubble rising in a gas-solid fluidized bed with the scale indicating solid fraction.

## 2. Overview of the ECT system

A two plane ECT tomograph was used in the present study. It consists of two arrays of electrodes, each array containing 12 electrodes. In Figure 3 a schematic drawing of the ECT sensor

is given. The location and size of the electrodes were designed by Process Tomography Ltd. [11]. As the sensor works with a soft field, it is very susceptible to external interference and thus the sensor is covered by a grounded screen to protect the electrodes from external noise. The non-intrusive design of the sensor can be observed in Figure 3. The electrodes are placed on the circumference of the $10.4cm$ diameter experimental tower and do not influence the flow behaviour.

The ECT tomograph produces a cross-sectional image showing the distribution of electrical permitivities of the content of the experimental tower from measurements taken at the boundary of the vessel [5]. The capacitance reading is taken between each set of electrodes and produces $E(E-1)/2$ different readings for one image that is reconstructed. $E$ represents the number of electrodes used in the ECT sensor [11]. These readings are interpreted and illustrated as a colourful image using a Linear Back Projection (LBP) reconstruction algorithm. An example of such an image is provided in Figure 3 via a virtual magnification of the computer screen. The resolution of the image is usually relatively low (due to soft field distortions) but can be sampled at high sample rates (low spacial resolution but high temporal resolution [2]). The quality of the image can be improved by off-line iterative LBP image reconstruction algorithms [12].

By comparing the diameter of known phantom objects with the diameter reconstructed via ECT of the same objects, McKeen and Pugsley [13] found errors between 4% and 10%, depending on the amount of iterations used in the off-line algorithm. In the present study only on-line measurements were used and the obtained data should approximately be valid as semi-quantitative results [12]. These semi-quantitative results have been confirmed by fibre optic probes in a study done by Pugsley et al. [12] by using off-line reconstruction iterations of the data collected from an 8 electrode ECT tomograph.

Both of the systems require thresholding in their obtained data. A threshold defines the void fraction that will indicate the boundary of a bubble. Each tomograph produces results using different measurements and also different reconstruction techniques. Hence each system will have a different threshold that will produce the most reliable results. In the work done by Gidaspow [20] they defined a bubble as a region where their computational simulations produced a solid fraction less than 0.2. It is a non-trivial task to decide exactly what void fraction values should be defined as a bubble as some bubbles might have a cloud surrounding it (as described by the Davidson model [21]). This cloud is associated with fast bubbles $(u_{br} > u_f = u_{mf}/\epsilon_{mf})$ and some researchers have even defined it as an independent phase since mixing across a cloud can only occur via slow molecular diffusion [20].

In another study the ECT tomograph used in the present work was utilised to measure the diameter of a standard ping-pong ball falling through the measuring planes [14]. The ball was filled with glass particles and was dropped through the empty bed. The ping-pong ball had a diameter of $2cm$ and after averaging the results from 7 runs and adjusting the threshold value, the ECT system measured a diameter of $2.12cm$ [14]. Adjusting the threshold value in the obtained data may improve
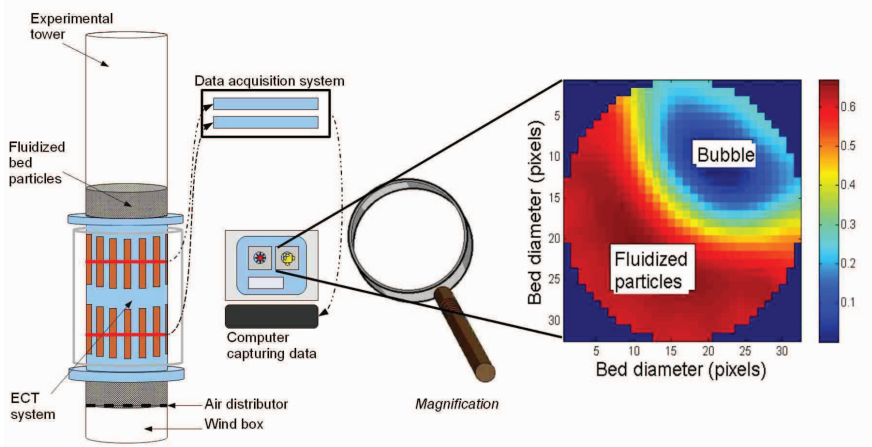
Figure 3: A schematical drawing of the 12 electrode ECT tomograph utilised in the present study together with and example of a typical cross-sectional 2D image (tomogram) obtained at a particular time instance.

the measurement accuracy of a single object passing through the ECT tomograph but will not aid in distinguishing multiple objects passing through the measuring planes. To effectively improve the measurement accuracy off-line reconstructions must be employed [12].

Nevertheless, in the present study a cylindrical hollow paperboard tube (known as a phantom object) with a diameter of 4.5$cm$ was used to estimate the threshold value. With the threshold equal to 10% that of the unfluidized bed solid fraction the diameter of the phantom object was reconstructed with near 99% accuracy. This does however not imply that the bubble sizes will be obtained with the same degree of accuracy as the paperboard wall of the phantom object might produce distortions in the recorded permitivity values.

High-performance ECT tomographs are also being developed with a 500$frame/s$ sample frequency with both image reconstruction and visualisation [15]. With this system direct reconstruction algorithms like the LBP, filtered LBP (FLBP) and Tikhonov regularization can be employed for on-line measurements. These images are usually blurred due to the soft field and the number of independent measurements [15]. Iterative methods are generally slow but much more accurate [15]

The obtained image consists of pixels and each represents an average solid fraction value. The average is taken over a rectangular volume equal to 1.1$cm^3$ [5] and is directly associated with the physical dimensions of the electrodes used in the ECT sensor. The bigger the electrodes are the bigger this averaging volume will become and the image resolution produced by the ECT system will go down. A 32×32 pixel image is produced and the pixels that fall outside the circular tower will assume zero solid fraction values (refer to Figure 2 and 3). Theoretically, the more electrodes used, the smaller the electrodes become and the more dominant the background noise can become. Thus a balance has to be kept so that the electrodes are

not too small but also not too big. The system used, with the twelve electrodes, can capture up to a hundred 32×32 matrix maps of solid fractions per second and increasing to two hundred frames per second for an 8 electrode sensor [5]. Practically between 6 and 16 electrodes are normally used [11].

This system also requires calibration. First the tower is left empty so that just air is present. The ECT software then calibrates this as the low permitivity material (the blue colour in the images used, as illustrated in Figure 2 and 3). Then the tower is filled with the particular particles and the ECT software calibrates this as the high permitivity material (the red colour in the images used as illustrated in Figure 2 and 3) [11]. This provides the reconstruction algorithm the necessary data points to represent the permitivities in-between these two extreme values.

The measuring planes are located at two different locations. One at a height of 15.65$cm$ and the other at a height of 28.65$cm$ above the porous plate distributor. The lower plane will be called *plane one* and the upper plane, *plane two*. Even though the ECT tomograph calculates average solid fraction values the data that are obtained are viewed as a slice through the bed at the center of each electrode. Due to the reconstruction program the measurements are also most accurate close to the center plane of the electrodes. Plane one and plane two are thus located at the center position of the electrodes (refer to Figure 3).

The two plane ECT tomograph is typically employed to measure the speed of bubbles in fluidized beds. If one bubble can be traced from one plane to the next, the time it takes for the bubble to traverse from one plane to the other, can be obtained. Using the distance between the two sensing planes the speed of a particular bubble can be determined.

Research done by Makkawi *et al* revealed that using ECT to measure dynamic parameters such as the standard deviation of the average solid fraction fluctuation and the bubble veloc-

ity or frequency, a minimum measuring span of $60s$ must be implemented [5]. Thus using a sampling rate of $100Hz$ and an experimental span of $60s$, 6000 images can be produced. Up to 8000 images can be produced in one experimental span (depending on the number of electrodes, computing power and speed of the reconstruction algorithm) [5]. For the rest of this study a measuring span of $60s$ was implemented.

## 3. Overview of the time-resolved X-ray tomography system

In the X-ray measurement system used in the present study three X-ray sources were used that each created a fan beam through the fluidized bed. Each fan beam fell onto two array detector consisting of 32 $CdWO_4$ detectors [8]. The set-up used in the present study is illustrated in Figure 4.

The red lines represent the path of radiation detected by each detector respectively. The fluidized bed is located in the middle of the set-up, surrounded by the detectors and sources. The diameter of the bed was $23.8cm$. The X-ray system can have a sampling frequency of $2500 frames/s$ but due to some inherent noise in the X-ray sources the obtained data had to be averaged. This was done by averaging over ten measurements which in turn lowered the sampling frequency to $250 frames/s$. The averaged data can be converted to a line-averaged solid fraction value by using calibration curves [8].
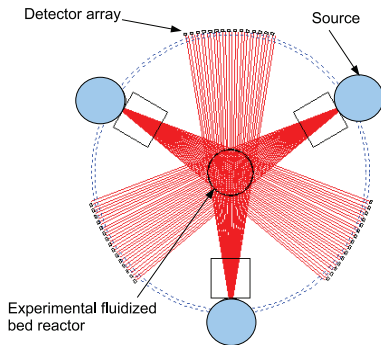


Figure 4: Three X-ray sources that simultaneously radiate an X-ray fan beam through the experimental fluidized bed tower or reactor. Two sets of 32 detectors have been allocated to each source.

The TU Delft X-ray tomography system consists of two arrays of detectors $4cm$ apart and both consisting of 32 detectors for each of the 3 sources. The distance from the center of the bed to the detector arrays was $85.8cm$ and the distance from the center of the bed to the sources was $71.6cm$. All of the X-ray beams originate from an approximate point source and diverges from there. Thus the effective distance between the measuring planes in the bed, can be shown to be equal to $1.86cm$. With the two measuring planes it was possible to determine the bubble rise velocity. Bubble size and velocity are crucial in determining factor such as the particle residence time, particle entrainment and heat and mass transfer in a fluidized bed [4]. Thus to

be able to determine the bubble shape, size and velocity is important and the X-ray tomographic system allows researchers to do exactly that.

Each detector measures the attenuation of a small cone shaped beam coming from the X-ray source located on the opposite side of the fluidized bed. This small cone is approximated as a line and treated as such in the reconstruction [8]. For a mono-energetic source a two point calibration would be sufficient. This would be calibration much like that of an ECT system with an empty tower and a full tower of particles. Most X-ray sources produce a wide spectrum of X-ray energies and thus a two point calibration is not adequate [8]. This implies that the absorption coefficient is a function of the photon energy. Non-linearity is also obtained due to the fact that the low energy photos are absorbed much faster than high energy photons. Hence, $R$ (measured number of photons) does not follow the Lambert-Beer law [8]. During calibration the effect of 'beam hardening' has to be accounted for. Beam hardening occurs as an increasing amount of powder is present on a particular X-ray beam and the relative number of high-energy photos increases [8]. To account for this effect each detector is calibrated individually with several quantities of powder. Seven calibration points are usually used in total including an empty and full tower as the two extreme values [8]. In the current study a five point calibration has been used due to the high attenuation of glass particles in comparison to that of polystyrene particles. If seven points were used, including an empty bed, the radiation would have been to low to get meaningful measurements. In the present study calibration thus entailed the center beams passing through 1/3, 1/2, 2/3, 5/6 of a full bed and a full bed. Using these calibration points the radiation level could be set high enough as to obtain meaningful measurements but also low enough as to not over expose the detector and thus avoid the detector from clipping. These criteria were chosen under the assumption that there won't be any bubbles with an effective diameter much greater than 2/3 of the tower diameter.

Before the actual measurements were made a segment of data were taken where no bubbles were present and it was then compared to the full undisturbed bed data obtained from calibration. In theory the ratio of these averaged detectors measured attenuations should be equal to 1 if the calibration is working properly. In Figure 5 (a) it is clear that this was not the case.

From Figure 5 (a) it is clear that for each of the three detector arrays a near parabolic-shaped discrepancy is obtained. This might be due to the motion of particles in the fluidized bed after fluidization and the consequent redistribution of particles. The powder used in the present study has a large range of particle sizes and thus a heterogeneous solid fraction distribution can be expected and was observed in the actual experiments. The correction factors obtained in Figure 5 (a) were used to correct all the collected data to account for these effects associated with the fluidization of the bed. These corrections were done twice to account for drift that can possibly occur within the experimental set-up. The second set of corrections were made from data captured 5 days later. In Figure 5 (a) it can be observed that one of the top detector arrays drifted the most. In Figure 5 (a)
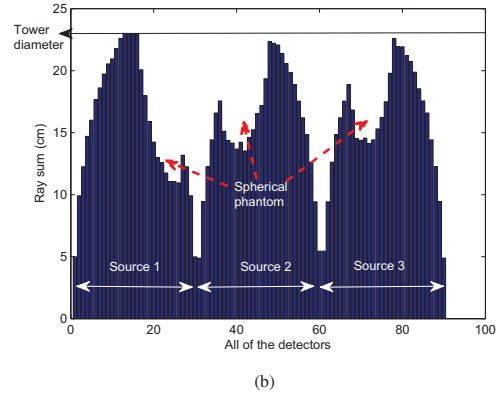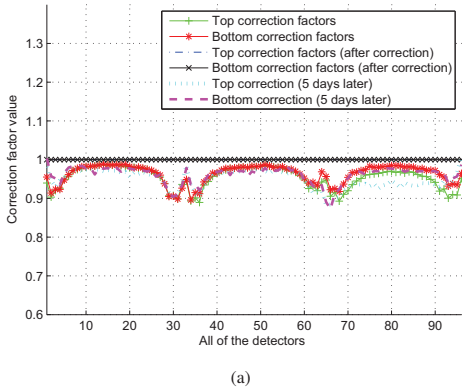
Figure 5: (a) Two sets of correction factors calculated from data captured at separate times for all of the detectors (3×32 detectors) before and after applying the correction factor. (b) The ray-sum of the path lengths of the X-ray beams travelling through the particulate phase in a fluidized bed containing a spherical phantom.

the same ratios are also shown after it has been corrected with the correction factors and thus the drift have been accounted for in all the data collected during the current experiments.
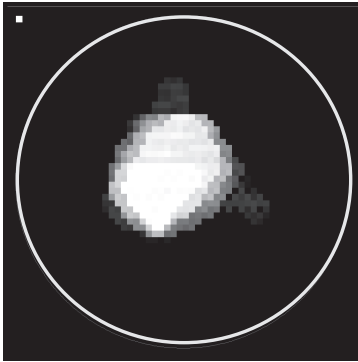


Figure 6: Typical image produced with the time-resolved X-ray tomography system illustrated in grey-scale. In the top left corner the size of a single pixel is illustrated.

A calibration curve was produced for each detector of all three double plane detector arrays. The calibration effectively produced a relationship between the measured attenuation and the distance the X-ray beam has to travel though the particulate phase. This concept is illustrated in Figure 5 (b) where the ray-sum (effective length of powder on the path of the beam) is provided for each detector. This image was created using the simulation program developed by Mudde and co-workers and simulates measurements taken with a spherical phantom (plastic rod) inserted into the bed. Each parabola represent one of the source-detector array pair and the disruption in the parabolic shape is due to the phantom. Hence the effect of a phantom or a bubble will be equivalent to having less powder in the path

of particular beams. With this path length information tomographic images can be created. For more detailed information about the calibration of a X-ray tomography system refer to work done by Mudde [8] and Rautenbach et al. [16]. In Figure 6 an example is provided of a typical time-resolved X-ray tomogram.

The images reconstructed with the time-resolved X-ray tomography system in the present study consisted of 3025 pixels (55×55 pixel image). The number of pixels used is an independent parameter and can be selected [8]. The Simultaneous Algebraic Reconstruction Technique (SART) is used that simultaneously applies the average of the corrections generated by all rays to a pixel instead of sequentially updating the pixel on a ray-by-ray basis [8]. The reconstructions are off-line, iterative and belongs to the algebraic technique class [8]. Some other reconstruction techniques that exist is the Back Projection algorithms, like those used with the ECT system, and they are significantly faster. Though these techniques are faster, they do present some limitations with regards to limited data sets [8].

A 5cm phantom object (plastic rod) was used to investigate the quantitative nature of the images produced by the system. Similar to the work done by McKeen and Pugsley [13] the actual diameter of the phantom was compared to the diameter given by the reconstructed X-ray tomograms. Errors between 6% and 25% was obtained depending on the location of the phantom. Nuclear based techniques are know for medium to high spacial resolution and the relatively high error obtained with the quantitative phantom study might be caused by the plastic walls of the phantom as the attenuation of plastic will be different to that of glass [12]. With this in mind the time-resolved X-ray tomography system should also be able to produce semi-quantitative results. In previous research done by Rautenbach et al. [16] they used the most accurate correlations, a literature study presented by S. Karimipour and T. Pugsley [4], to determine a threshold value for the presently obtained data. Therefore a threshold value of 0.465 was used for the

5

X-ray experiments in the present study in accordance with previous research [16].

Similar to the work done by Makkawi and Wright [5] the influence of the experimental span of time resolved X-ray tomography on the dynamic parameters in a fluidized bed was investigated by Rautenbach et al. [16]. For the time-resolved X-ray tomography system investigated, different results were obtained for various dynamic parameters. By using a single jet it was found that a measuring span of 40$s$ produced reliable results for the bubble rise velocity. In the case of the average bubble volume and bubble frequency a 20$s$ experiment produced reliable results when using the single jet. In using the porous plate distributor a measuring span of 45$s$ was adequate for determining the bubble rise velocity while 25$s$ was accurate enough for the average bubble volume and bubble frequency. In the present study an experimental span of 50$s$ were used for all the dynamic parameters recorded with the X-ray tomography system and according to Rautenbach et al. [16] this should present reliable results when using the current X-ray system.

## 4. Summary of the advantages and limitations of the two tomographic modalities

These tomographic measurement system clearly hold some advantages but they also present some disadvantages or limitations (as with most measurement techniques). These strengths and weaknesses have to be considered for each particular application to find the measurement technique that is most suited for the application. For convenience these advantages and disadvantages associated with each measurement technique are summarised and presented in Table 1.

## 5. Experimental set-up

Glass particles with an approximate density of 2485$kg/m^3$ are used in the experiments. Most of the powders utilised in the present study are classified as Geldart B or D particles. Only the powder utilised in the X-ray experiments were on the boarder between Geldart A and B and might thus exhibit characteristics from both groups. These powders all consisted of spherical particles and were chosen because of their ability to produce a bubbling bed without phenomena like spouts or channelling. Doing experiments with this 'well behaved' powders enabled the present study to focus on bubbling behaviour and illustrated the use of the two tomographic modalities without being distracted with complex phenomena like channelling.

The parameters of the two experimental set-ups are presented in Table 2 with $\overline{d}_{sv}$ the surface-volume mean diameter, $\overline{d}$ the arithmetic mean and $u_{mf}$ the minimum fluidization velocity. Various particle size distributions were used during the ECT experiments. These different particle size distributions formed part of previous studies performed by Rautenbach et al. [19] and will be used in the present study to evaluate the performance of the ECT tomograph compared to that of the X-ray tomograph. The particle mixtures will be referred to as *mix 1* and *mix 2*, as indicated in Table 2. In both sets of experiments

plexiglass towers were used and compressed air at room temperature was used as fluidizing gas. The experimental tower had a diameter of 10.4$cm$ in the ECT experiments and a diameter of 23.8$cm$ in the time-resolved X-ray tomography experiments.

With the ECT tomograph the sensor was fixed in one location for the duration of the experiments. The sensor has two measuring planes, as depicted in Figure 3, and thus data was obtained at two distinct heights, 15.7$cm$ and 28.7$cm$ above the air distributor. With the time-resolved X-ray tomography tomograph measurements were taken at 24.0$cm$, 34.0$cm$ and 46.2$cm$ from the air distributor to the height where the X-ray beams left the source. This system also has 2 measuring planes but much closer together than those of the ECT tomograph and the information from these two planes are usually averaged (for example, the average bubble volume is the average of the bubble volume at the first and second plane). The averaging of the information from the two planes was not done with the ECT experiments as the sensors were too far apart.

## 6. Comparison between ECT and time-resolved X-ray tomography results

In Figure 7 the average bubble volume measured with the two tomographs are given as functions of the superficial velocity, $u_0$. In the case of the ECT measurements bubble rise velocities could not be measured. The centers of the electrodes were 13$cm$ apart and thus bubbles will coalesce as the bubbles traverse from one measuring plane to the next. Thus bubble velocity correlations were used to create a spatial 3D image from the collected temporal tomographic data [19].

The dependence of the minimum fluidization velocity on the particle size distribution is clearly illustrated in Figure 7. To be able to compare the results in a more direct manner Figure 8 is provided where the average bubble volume were plotted against a dimensionless coefficient (DC) expressed as

$$DC = \frac{u_0 - u_{mf}}{\sqrt{g\overline{d}}}, \tag{1}$$

where $g$ is gravitational acceleration and $\overline{d}$ is the particular mean particle size presented in Table 2. The dimensionless coefficient takes into account most of the effects of the mean particle size and thus allows the data to be viewed together in a more comparative way. From both Figure 7 and 8 it is clear that the bubbles become larger as they move upward through the bed. Interesting result are given by the mixed particle size distributions. In Figure 7 and 8 the $100 - 200\mu m$ powder behaves similar to the *mix 1* powder at both plane 1 and plane 2. The most interesting result is obtained with the *mix 2* powder. For the same values of the dimensionless coefficient in Figure 8, the *mix 2* powder reviled much smaller bubbles compared to the other powders. With the *mix 2* powder the measurements at plane 2 suggest that a maximum bubble size has been reached as the bubble volume does not increase monotonously. This is an interesting result as the powder can still be classified as a Geldart D powder but exhibits behaviour that is typical for Geldart A particles [21]. Thus a small amount of small particles

Table 1: Properties of the two tomographic systems investigated in the present study.

| Property | ECT | Time-resolved X-ray tomography | General comments |
|---|---|---|---|
| **Spacial resolution** | $1.79cm$ for the current 12 electrode system (on-line resolution without off-line processing). According to the system manual it is not a trivial task to express the radial resolution mathematically but an indication of the radial resolution can be calculated using $M/E$. Here $M$ is the number of independent measurement that can be made and $E$ is the number of electrodes [11]. | Approximately $2.5cm$ but this resolution can be improved apon if the outer detectors are shielded to allow higher energy radiation to be used. This would improve the resolution in the center of the bed without over exposing the side detectors. (Off-line data processing) | Both systems are more sensitive close to the tower walls and thus has a higher resolution close to the walls. |
| **Size limitation** | $10.4cm$ is close to the maximum tower diameter that the ECT system can handle up to date. This limitation is due to the soft field the ECT system employs to capture solid fraction distributions. | This system has no tower size limits as it works with a hard field. With the appropriate calibration and detector installations measurements can be made in large set-ups. | The larger the experimental tower the higher energy X-rays has to be used. |
| **Tower content (powders used)** | Must be non-conductive | Material may be conductive but must not attenuate too much X-ray radiation. The denser the substance the more radiation is attenuated. | |
| **Measurement frequency** | $100Hz$ but when working with the average solid fraction values obtained from each measurement, every 5 values are usually averaged to lower the noise. | $250Hz$, after a average over every 10 images has been made to lower the inherent noise associated with the X-ray source. | Due to the current reconstruction algorithm of the ECT system it can give an on-line image of the content of the tower with a frequency of $100Hz$. This makes it viable for process control applications. At the present the reconstruction of X-ray tomography data is not on-line. |
| **Invasiveness** | Neither invasive nor intrusive | Neither invasive nor intrusive | Both systems does not interfere with the internal flow behaviour of the bed. |

7

| Property | ECT | Time-resolved X-ray tomography | General comments |
|---|---|---|---|
| 3D representation | It is possible to view the data in a variety of ways including 3D images and solid fraction profiles [5]. | 3D images and information can readily be obtained [16, 8]. | |
| Solid fraction representation | Solid fraction maps can be recorded for each measurement taken. This makes it possible to obtain information about the solid fraction distribution within the bed at any given time. The average solid fraction value of the tower at each time step can also be calculated that can be used for statistical analyses of the bed behaviour [17, 18]. | The information obtained can mainly be used to identify and illustrate bubbles and solid fraction distributions are not obtained. | |
| Technical skill required | System is easy to operate and does not require a high degree of technical skill. | System requires a significant amount of technical skills including nuclear safety education and training. | Both systems require additional off-line data processing (depending on the data required). |
| Bubble rise velocity | Can not be determined for each particular bubble as the measurement planes were to far apart. Various sensor designs can be utilised that can measure bubble rise velocity [12]. | Can readily be calculated for each particular bubble. | Bubble velocities can be calculated with the ECT system used in the present study, if the bubbles does not undergo to much transformations from one measuring plane to the next. |
| Safety risks | Very safe and can be used in an ordinary laboratory or industrial environment without any major safety protocols. | Very safe but a safety protocol has to be followed. The system also requires to be insulated within a lead room to prevent radiation escaping into the surrounding environment. Numerous installations have to be made to make the system run safely and effectively and thus it can not readily be used in a normal laboratory or industrial environment. | |

Table 2: Relevant parameters of the powders and experimental towers used in the present study.

**ECT**

| Particle size distribution | Mean particle size ($\bar{d}_{sv}$) [$\mu m$] | Solid fraction ($\epsilon_s$) [-] | Tower diameter [$m$] | $u_{mf}$ [$m/s$] | Distributor | Geldart classification |
|---|---|---|---|---|---|---|
| $100 - 200\mu m$ | 153 | 0.68 | 0.104 | 0.02 | porous plate | B |
| $400 - 600\mu m$ | 482.9 | 0.68 | 0.104 | 0.21 | porous plate | B |
| $750 - 1000\mu m$ | 899.15 | 0.67 | 0.104 | 0.45 | porous plate | D |
| *mix 1*: 50% $100 - 200\mu m$ 50% $400 - 600\mu m$ | 265.58 | 0.66 | 0.104 | 0.04 | porous plate | B |
| *mix 2*: 8.5% $100 - 200\mu m$, 8.5% $400 - 600\mu m$, 83% $750 - 1000\mu m$ | 800.35 | 0.7 | 0.104 | 0.27 | porous plate | D |

**Time-resolved X-ray tomography**

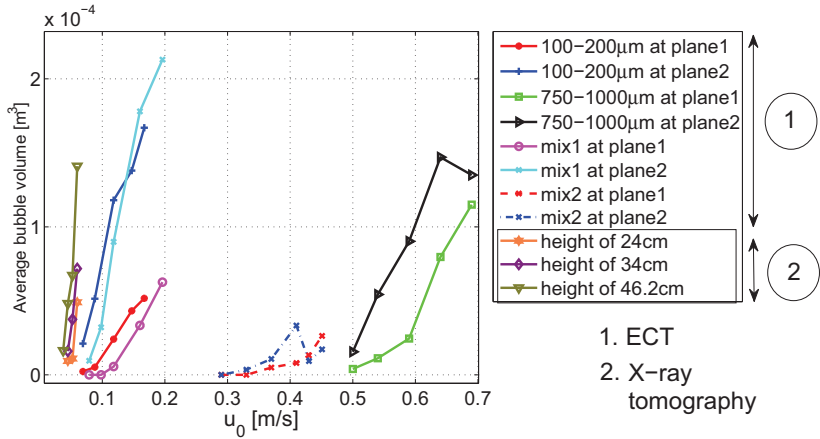| Particle size distribution | Mean particle size ($\bar{d}$) [$\mu m$] | Solid fraction ($\epsilon_s$) [-] | Tower diameter [$m$] | $u_{mf}$ [$m/s$] | Distributor | Geldart classification |
|---|---|---|---|---|---|---|
| $79 - 149\mu m$ | 114 | 0.66 | 0.238 | 0.009 | porous plate | A/B |



Figure 7: Comparison of the ECT- and Time resolved X-ray tomography average bubble volume data as a function of the superficial velocity, $u_0$.
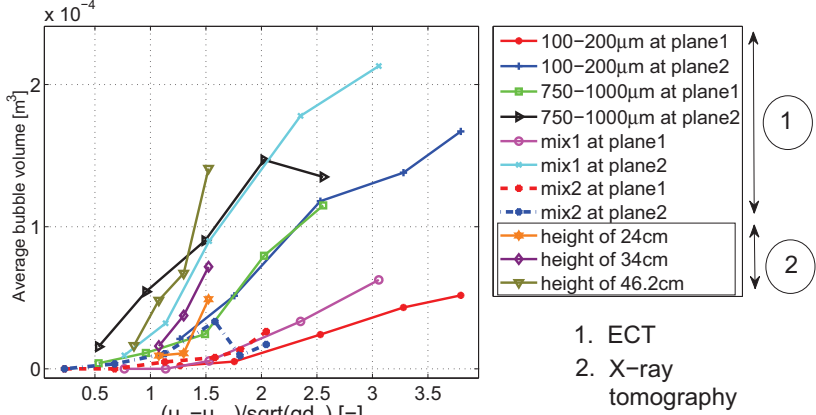
Figure 8: Comparison of the ECT- and Time resolved X-ray tomography average bubble volume data as a function of the dimentionalless coefficient described in equation (1).

can change the hydrodynamic of a powder in a fluidized bed, as noted before in literature [19, 22].

The $750 - 1000\mu m$ powder also indicates a maximum bubble volume but this is probably an indication of the onset of the slugging regime as the equivalent bubble diameter at the maximum is 63% of the tower diameter [21]. The powder used in the Time-resolved X-ray tomography experiments indicated that the bubbles kept growing as they traversed up through the bed.

In Table 3 the obtained data from both tomographs are compared to some theoretical correlations. The correlations were chosen based on the recommendation of Karimipour and Pugsley [4]. They evaluated 25 different bubble size correlations with data available from the open literature [4]. These correlations were all empirical and different measurement techniques and powders were used in creating the correlations [4]. Nevertheless they found that the correlation by Cai et al. gave the best predictions for bubble sizes especially for Geldart A and D particles [4]. The simple correlation of Mori and Wen [21] provided the best results for Geldart B particles and the correlation by Agarwal [4] provided the best correlation for measurements take with $u_0 < 10u_{mf}$. In Table 3 the condition under which each model is claimed to perform best is also provided.

In the present study the comparison between the theory and experiments will be made via the root mean square error of prediction (RMSEP) [23]. The RMSEP is a way to evaluate the prediction performance of each correlation and can be expressed as

$$RMSEP = \sqrt{\frac{\sum_{i=1}^{n}(\widehat{y_i} - y_i)^2}{n}}, \qquad (2)$$

where $\widehat{y_i}$ is the predicted values from the correlation, $y_i$ is the experimental data obtained from the tomographs and $n$ in the number of experimental data points. The RMSEP values are given in the same unites as $\widehat{y_i}$ and $y_i$. All of the correlations presented in Table 3 are expressed in centimetres and thus the comparisons were done in, and expressed in centimetres [$cm$].

The correlations gave predictions of the bubble size in terms of bubble diameter. To be able to compare the average bubble volume data obtained with the tomographs with the correlations, the equivalent diameters of the average bubble volumes were employed. The equivalent bubble diameter is the diameter of a sphere which will produce the same volume as a particular measured bubble.

In Table 3 it is evident that the mixed powders generally produce the largest discrepancy from the correlations especially the *mix* 2 powder at plane 2. The reason for this discrepancy can be explained via Figure 7 and 8 where it is clear that the *mix* 2 powder reaches a maximum bubble volume. These correlations does however not take into account all of the phenomena associated with wide particle size distributions and thus fail in accurately predicting the bubble size.

In Figure 9 the bubble frequency of each set of experiments are provided as a function of the superficial velocity. With the powders investigated with the ECT tomograph it is interesting to note that all of the powders, except the *mix* 2 powder, had frequency values that increased with a low gradient at plane 2. This is a clear indication of some slugging characteristics as slugs are characterised as big periodic bubbles. All of the powders investigated with the ECT tomograph produced sharply increasing frequency values at plane 1 except the $750 - 1000\mu m$ powder that also has a decreasing frequency at high superficial velocities (thus indicating the onset of slugs at plane 1). The *mix* 2 powder was the only powder that produced sharply increasing frequency values at plane 2 that again point to the splitting and coalescence of bubbles in the powders much like a Geldart A powder. A small amount of small particles can thus be added to a slug prone powder, like the $750 - 1000\mu m$ powder, to make the powder less prone to slugging and to lower the

Table 3: Comparison between equivalent bubble diameter data and well established correlations. The prediction performance is done via the root mean square error of prediction (RMSEP) [23].

**RMSEP values for the ECT experiments [cm]**

| Particle size distribution | Mori and Wen [21, 4] (*Gekdart B and D*) | Werther [21, 4] (*Geldart A, B and D*) | Agarwal [4] ($u_0 < 10u_{mf}$) | Cai et al. [4] (*Geldart A and D*) |
|---|---|---|---|---|
| **Plane 1** | | | | |
| $100 - 200\mu m$ | 0.65 | 0.91 | 0.51 | 0.71 |
| $750 - 1000\mu m$ | 0.64 | 1.33 | 0.39 | 0.88 |
| *mix 1*: 50% $100 - 200\mu m$, | | | | |
| 50% $400 - 600\mu m$. | 1.77 | 1.88 | 1.39 | 1.64 |
| *mix 2*: 8.5% $100 - 200\mu m$, | | | | |
| 8.5% $400 - 600\mu m$, | | | | |
| 83% $750 - 1000\mu m$. | 2.03 | 2.86 | 1.61 | 1.5 |
| **Plane 2** | | | | |
| $100 - 200\mu m$ | 0.41 | 1.05 | 1.28 | 0.62 |
| $750 - 1000\mu m$ | 1.33 | 2.39 | 1.02 | 0.65 |
| *mix 1*: 50% $100 - 200\mu m$, | | | | |
| 50% $400 - 600\mu m$. | 0.76 | 1.41 | 1.48 | 0.97 |
| *mix 2*: 8.5% $100 - 200\mu m$, | | | | |
| 8.5% $400 - 600\mu m$, | | | | |
| 83% $750 - 1000\mu m$. | 3.33 | 4.75 | 2.43 | 2.86 |

**RMSEP values for the Time-resolved X-ray tomography experiments [cm]**

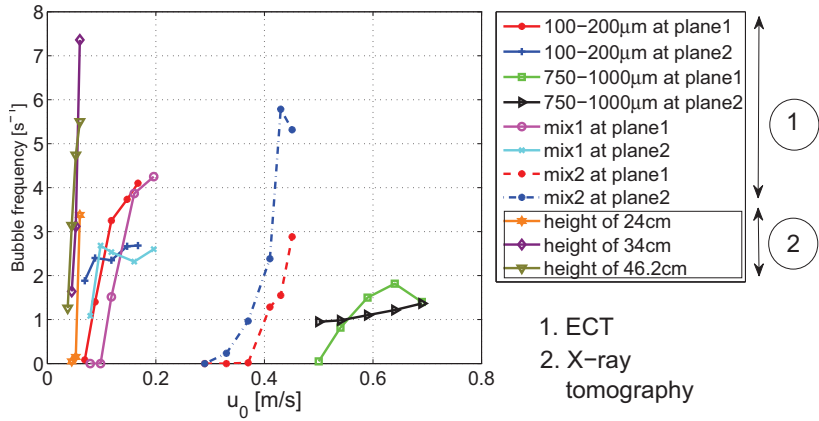| Particle size distribution | Mori and Wen [21, 4] (*Gekdart B and D*) | Werther [21, 4] (*Geldart A, B and D*) | Agarwal [4] ($u_0 < 10u_{mf}$) | Cai et al. [4] (*Geldart A and D*) |
|---|---|---|---|---|
| **Measuring plane height = 24cm** | | | | |
| $79 - 149\mu m$ | 0.73 | 0.84 | 0.99 | 0.72 |
| **Measuring plane height = 34cm** | | | | |
| $79 - 149\mu m$ | 0.79 | 0.92 | 1.02 | 0.59 |
| **Measuring plane height = 46.2cm** | | | | |
| $79 - 149\mu m$ | 1.15 | 1.63 | 1.2 | 0.85 |



Figure 9: Bubble frequency as a function of the superficial velocity for all the experiments conducted in the present study.

minimum fluidization velocity.

The powder used in the Time resolved X-ray tomography experiments indicated that the highest frequency was observed at the second highest measuring height. The $79-149\mu m$ powder is on the boarder between Geldart A and B particles and this high frequency at the second highest measuring plane might indicate that the bubbles split and re-coalesce in this powder as well.

## 7. Conclusion

The present study compared two tomographic measurement systems. The two systems used were a Electrical Capacitance Tomography (ECT) and time-resolved X-ray tomography tomograph. Both tomographs record relevant data on a non-intrusive manner and provided 3D data that could readily be employed to studying hydrodynamic effects in a fluidized bed. Each system has advantages and limitations and depending on the application a choice should be made which system is most fitting.

The results obtained from both tomographs were compared with some established bubble size correlations from the open literature. Relatively good agreement was found between the theory and experiments. The powder with the widest particle size distribution (*mix* 2) had the largest discrepancy with the theory. The conclusion was that the correlations could not account for all of the hydrodynamic effects associated with a wide particle size distribution. These conclusions were also supported by the bubble frequency data presented in the present study.

## References

[1] J. Grace, A perspective on development of novel fluidized bed processes for a more sustainable global future., in: S. Kim, Y. Kang, J. Lee, Y. Seo (Eds.), Fluidization XIII, ECI, South Korea, 2010, pp. 1–8.

[2] J. R. van Ommen, R. F. Mudde, Measuring the gas-solids distribution in fluidized beds – a review, International Journal of Chemical Reactor Engineering 6 (R3) (2008) 1–29.

[3] J. Werther, Measurement techniques in fluidized beds, Powder Technology 102 (1999) 15–36.

[4] S. Karimipour, T. Pugsley, A critical evaluation of literature correlations for predicting bubble size and velocity in gas-solid fluidized beds, Powder Technology 205 (2011) 1–14.

[5] Y. Makkawi, P. Wright, Electrical capacitance tomography for conventional fluidized bed measurements-remarks on the measuring technique, Powder Technology 148 (2004) 142–157.

[6] C. Qiu, B. Hoyle, F. Podd, Engineering and application of a duel-modality process tomography system, Flow Measurement and Instrumentation 18 (2007) 247–254.

[7] C. Muller, D. Holland, A. Sederman, M. Mantle, L. Gladden, J. Davidson, Magnetic resonance imaging of fluidized beds, Powder Technology 183 (2008) 53–62.

[8] R. Mudde, Time-resolved x-ray tomography of a fluidized bed, Powder Technology 199 (2010) 55–59.

[9] M. Stein, Y. Ding, J. Seville, D. Parker, Solid motion in bubbling gas fluidized beds, Chemical Engineering Science 55 (2000) 5291–5300.

[10] X. Fan, D. Parker, Z. Yang, J. Seville, J. Baeyens, The effect of bed materials on the solid/bubble motion in a fluidized bed, Chemical Engineering Science 63 (2008) 943–950.

[11] Process tomography Ltd., 86 Water Lane, Wilmslow, Cheshire. SK9 5BB, UK, PTL300-TP-G ECT system, Operation manual (07 2003).

[12] T. Pugsley, H. Tanfara, S. Malcus, H. Cui, J. Chaouki, C. Winters, Verification of fluidized bed electrical capacitance tomography measurements with a fibre probe, Chemical Engineering Science 58 (2003) 3923–3934.

[13] T. R. McKeen, T. S. Pugsley, The influence of permittivity models on the phantom images obtained from electrical capacitance tomography, Measurement Science and technology 13 (2002) 1822–1830.

[14] R. Sharma, S. Karki, N. Masoudi, Electrical capacitance tomography for characterising bubbles in fluidized beds, Master's thesis, Telemark University College, Porsgrunn, Norway (2010).

[15] Z. Cui, H. Wang, Z. Chen, Y. Xu, W. Yang, A high-performance digital system for electrical capacitance tomography, Measurement Science and Technology 22, 055503.

[16] C. Rautenbach, R. Mudde, M. Melaaen, B. Halvorsen, The influence of the experimental span of time-resolved x-ray tomography on the dynamic parameters in a fluidized bed., in: G. Washington, T. Jefferson (Eds.), IFSA, Industrial Fluidization South Africa, Johannesburg, South Africa, 2011.

[17] J. Halow, G. Fasching, P. Nicoletti, J. Spenik, Observations of a fluidized bed usig capacitance imaging, Chemical Engineering Science 48 (1993) 643–659.

[18] Y. T. Makkawi, P. C. Wright, Fluidization regimes in a conventional fluidized bed characterised by means of electrical capacitance tomography, Chemical Engineering Science 57 (2002) 2411–2437.

[19] C. Rautenbach, M. C. Melaaen, B. M. Halvorsen, Investigating the influence of fines in fluidized bed reactors using 3d ect images, in: A. A. Mammoli, C. A. Brebbia (Eds.), Computational Methods in Multiphase flow VI, Wessex Institute of Technology, WIT-Press, Ashurst Lodge, Ashurst, Southampton SO40 7AA, UK, 2011, pp. 141–151.

[20] D. Gidaspow, Multiphase Flow and Fluidization, Continuum and Kinetic Theory Descriptions, Academic Press, Harcourt Brace & Company, 525 B Street, Suite 1900, San Diego, California 92101-4495, 1994.

[21] D. Kunii, O. Levenspiel, Fluidization Engineering, Butterworth-Heinemann, 1991.

[22] C. van Biljon, E. du Toit, W. Nicol, Effect of fines on the bubble properties in a two-dimensional fluidized bed by digital image analysis, in: A. Luckos, P. den Hoed (Eds.), Industrial Fluidization South Africa, Supporting sustainable strategies, Southern African Institute of Mining and Metallurgy, Chamber of Mines Building, 5 Hollard Street, Johannesburg 2017, South Africa, 2011, pp. 267–275.

[23] K. H. Esbensen, L. P. Julius, Representative sampling, data quality, validation - a necessary trinity in chemometrics, Comprehensive Chemometrics 4 (2009) 1–20.

# Paper G

# Statistical diagnosis of a gas-solid fluidized bed using Electrical Capacitance Tomography.

# Statistical diagnosis of a gas-solid fluidized bed using Electrical Capacitance Tomography.

Christo Rautenbach, Morten C. Melaaen and Britt M. Halvorsen

*Institute for Process, Energy and Environmental Technology*
*Telemark University College*
*Norway*
*T: +47 3557 5222; E: christo.rautenbach@hit.no*

## Abstract

Fluidization experiments were performed using several particle size distributions of spherical glass particles, ranging from Geldart B to D. An Electrical Capacitance Tomography (ECT) tomograph was utilised in the present study and its usefulness as a diagnostic tool is illustrated. During the experiments a $10.4cm$ diameter tower was utilised and the tower was operated at atmospheric pressure and room temperature (cold fluidized bed). Statistical analysis were performed on the average solid fraction data obtained using the ECT tomograph. Using the time domain skewness and kurtosis the time series could be characterised and the quality of fluidization is determined at different superficial gas velocities (Azizpour, H., Sotudeh-Gharebagh, R., Zarghami, R., Abbasi, M., Mostoufi, N., and Mahjoob, M. (2011). Characterization of gas-solid fluidized bed hydrodynamics by vibration signal analysis. *International Journal of Multiphase Flow*, 37:788-793). Statistical analysis is also used to characterise the influence of small particles on the bed hydrodynamics.

*Keywords:* ECT, Gas-solid fluidization, particle size distribution, fluidization quality, skewness, excess kurtosis

## 1. Introduction

Fluidized bed reactors are used in a variety of industrial applications including Chemical Looping Combustion (CLC) and Biomass gasification. The efficiency of gas-solid fluidized bed reactors depends on the mixing of the gas and solids and even though these reactors are very successful they do present some limitations (Azizpour et al. 2011, Saxena et al. 1993). De-fluidization is one of the problems that may occur in fluidized beds due to changes in the hydrodynamics of the bed during operation (Azizpour et al. 2011). Therefore it is important to understand the complex hydrodynamics of fluidized beds and to be able to monitor the quality of fluidization under various operating conditions.

The quality of fluidization can be described in terms of the uniformity of distribution of the fluidizing gas (Patel et al. 2008). Several measurement techniques have been utilised in the past to investigate the quality of fluidization or the gas maldistribution in a fluidized bed. These techniques include pressure probe measurements (Saxena et al. 1993, Lin and Wey 2004), temperature probe measurements (Saxena et al. 1993), $\gamma$-ray tomog-

raphy and acoustic measurements (Azizpour et al. 2011, Salehi-Nik et al. 2009). The different measurements techniques have different advantages and disadvantages and can be used to diagnose the quality of fluidization. In the work done by Lin et al. (2004) the quality of fluidization was described using the fluidization index. The fluidization index used by Lin et al. (2004) is modified from its original form and was used to describe good or bad bed behaviour in terms of the pressure fluctuations in the bed. The fluidization index can also be related to the maldistribution factor, $\chi$, used in the work done by Patel et al. (2008) and Loser (1999). The maldistribution factor can be defined for pixilated solid fraction images and is defined as

$$\chi = \frac{1}{n} \sum_{i=1}^{n} \left( \frac{\alpha_i - \overline{\alpha}}{\overline{\alpha}} \right), \tag{1}$$

where $n$ denotes the number of pixels in the particular image (tomogram), $\alpha_i$ is the solid fraction of a particular pixel and $\overline{\alpha}$ is the solid fraction of the entire image or reactor cross-section (Patel et al. 2008). Alternatively pressure frequency and magnitude have been used to
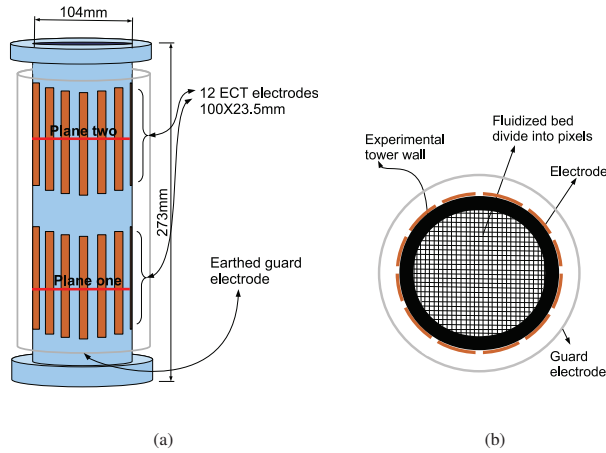
Figure 1: A schematic drawing of the two plane ECT tomograph utilised in the present study. (a) The two measuring planes of the system are indicated together with the electrodes and earthed guard screen. (b) A cross-sectional view of the ECT sensor together with the 1024 pixels created by the reconstruction program.

access the quality of fluidization (Lin and Wey 2004). Good quality fluidization can be obtained by keeping pressure fluctuation as small and frequent as possible as this will indicate numerous small bubbles (Lin and Wey 2004). Statistical methods in combination with the fluidization index and the maldistribution factor, $\chi$, have been successfully used to diagnose the fluidization quality in fluidized beds (Saxena et al. 1993, Lin and Wey 2004, Salehi-Nik et al. 2009). Since these methods have successfully been used with pressure fluctuation measurements it appears feasible to do the same analysis with solid fraction fluctuation measurements obtained with the ECT tomograph. Pressure fluctuations are an indirect indication of the solid fraction fluctuation in the bed and by using the ECT tomograph the entire cross-section of the bed is taken into account as oppose to only a probe volume (Makkawi and Wright 2002). A pressure probe is usually located at the bed wall and according to Saxena et al. (1993) the probe will only register damped pressure fluctuations that reaches the bed wall. By using the ECT tomograph the entire cross-section of the bed is taken into account. Viewing the entire cross-section of the experimental reactor will give a better representation of the dynamic behaviour of the bed. The data obtained with the ECT tomograph can also be viewed as images which can be used to confirm the behaviour deduced from the statistical analysis.

The importance of particle size distributions is well described in literature (Lin and Wey 2004, Jayarathna and Halvorsen 2009) and more recent studies investigated the influence of small particles on the overall bed behaviour in a 2D bed using photographic methods (van Biljon et al. 2011). To examine the effect of small particles on the overall bed behaviour in a 3D bed, various amounts of small particles were mixed into the powder of larger particles used in the experiments.

The aim of the present study was to use statistical methods to diagnose the quality of fluidization for four different mixtures of spherical glass particles and to illustrate the usefulness of the ECT tomograph for this purpose. The influence of small particles on the overall bed hydrodynamics, were also investigated. The analysis was performed on cross-sectional solid fraction data obtained with a ECT tomograph at two bed heights.

## 2. Experimental

### 2.1. Measurement apparatus, ECT tomograph

A two plane ECT tomograph was utilised in the present study. It consists of two arrays of electrodes each array containing twelve electrodes. In Figure 1 a schematic drawing of the ECT sensor is given. The location and size of the electrodes were designed by Process Tomography Ltd. (2003). As the sensor works with a soft field, it is very susceptible to external interference and thus the sensor is covered by a grounded screen to

2

protect the electrodes from external noise. The non intrusive design of the sensor can be observed in Figure 1. The electrodes are placed on the circumference of the experimental tower and does not influence the flow behaviour.

The ECT tomograph produces a cross-sectional image showing the distribution of electrical permittivities of the content of the experimental tower (Makkawi and Wright 2004). The capacitance reading is taken between each set of electrodes and produces $E(E-1)/2$ different measurements for one image that is reconstructed. $E$ represents the number of electrodes used in the ECT sensor. These measurements are interpreted and illustrated as a colourful image using the Linear Back Projection (LBP) reconstruction algorithm. An example of such an image is provided in Figure 2. The resolution of the image is usually relatively low but can be sampled at high sample rates (low spatial resolution but high temporal resolution). Off-line image processing can also improve the quality of the image (Makkawi and Wright 2002) but the present study investigated the use of only on-line measurements. The measuring
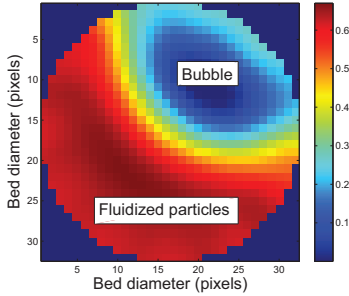


Figure 2: A cross-sectional image of the experimental tower indicating the solid fraction values inside the tower at a particular plane. Red indicates particles at minimum fluidization conditions and blue indicates air.

planes are located at two different locations. The heights in the fluidized bed will be denoted by $H_m$, the tower diameter by $D$ and the static bed height by $H$. The first plane is located at a height of $15.65cm$ ($H_m/D = 1.5$) and the other at a height of $28.65cm$ ($H_m/D = 2.8$) above the porous plate distributor. The lower plane will be called *plane one* and the upper plane, *plane two* (refer to Figure 1 (a)). Even though the ECT tomograph calculates average solid fraction values the data that are obtained are viewed as a slice through the bed at the center of each electrode. Due to the reconstruction program

the measurements are most accurate close to the center plane of the electrodes. Plane one and plane two are thus located at the center position of the electrodes (refer to Figure 1 (a)). Some validation of the ECT tomograph has been done and it was shown that the ECT tomograph gives relatively accurate results when a known volume of a dielectric object could be measured with the ECT tomograph (Warsito and Fan 2005, Sharma et al. 2010, McKeen and Pugsley 2002, Pugsley et al. 2003).

Research done by Makkawi et al. (2004) revealed that using ECT to measure dynamic parameters such as the standard deviation of the average solid fraction fluctuation and the bubble velocity or frequency, a minimum measuring span of $60s$ must be implemented. Thus using a sampling rate of $100Hz$ and an experimental span of $60s$, 6000 images can be produced. Up to 8000 images can be produced in one experimental span (depending on the number of electrodes, computing power and speed of the reconstruction algorithm) (Makkawi and Wright 2004). For the remainder of this study a measuring span of $60s$ were implemented.

### 2.2. Experimental configuration and parameters

To investigate the influence of small particles on the hydrodynamics of a fluidized bed a range of different particle sizes were mixed. During the course of the present study the $100 - 200\mu m$ particles will be the smallest particle size distribution used and was mixed with powders of larger size distributions. The mixtures that were investigated are presented in Table 1. Each of the mixtures had different percentages of small particles. Investigating these mixtures provided valuable results related to the influence of small particles on fluidized bed hydrodynamics. The mean particle diameter was calculated using the *surface-volume mean* diameter and is defined as

$$\overline{d}_{sv} = \frac{1}{\sum_i x_i/d_i}, \tag{2}$$

with $x_i$ the mass fraction of the particular particle size, $d_i$. The particles were spherical glass particles with an approximate density of $2485kg/m^3$. Compressed air was used as fluidizing fluid. The experimental tower had a diameter of $D = 10.4cm$ and a height of $1.5m$. The $100 - 200\mu m$ particles and *mix 1* (refer to Table 1) was classified as Geldart B particles while the $750 - 1000\mu m$ particles and *mix 2* were classified as Geldart D particles. The difference in behaviour of these particles will be made clear in the statistical diagnosis of the different particle size distributions.

3

Table 1: Relevant parameters of the powders and experimental tower used in the present study.

| Particle size distribution | Mean particle size $(\bar{d}_{sv})$ [$\mu m$] | Solid fraction $(\epsilon_s)$ [-] | $H/D$ [-] | $u_{mf}$ [$m/s$] | Distributor |
|---|---|---|---|---|---|
| $100 - 200\mu m$ | 153 | 0.68 | 4.6 | 0.02 | porous plate |
| $400 - 600\mu m$ | 482.9 | 0.68 | — | 0.21 | porous plate |
| $750 - 1000\mu m$ | 899.15 | 0.67 | 4.4 | 0.45 | porous plate |
| *mix 1*: 50% $100 - 200\mu m$, 50% $400 - 600\mu m$ | 265.58 | 0.66 | 4.6 | 0.04 | porous plate |
| *mix 2*: 8.5% $100 - 200\mu m$, 8.5% $400 - 600\mu m$, 83% $750 - 1000\mu m$ | 800.35 | 0.7 | 4.7 | 0.27 | porous plate |

## 3. Theory; Sample skewness and sample excess kurtosis

For a sample of $N$ measurements the **sample skewness** ($SS$) can generally be defined as

$$SS = \frac{\frac{1}{N}\sum_{i=1}^{N}\left(\phi_{si} - \overline{\phi_s}\right)^3}{\left(\frac{1}{N}\sum_{i=1}^{N}\left(\phi_{si} - \overline{\phi_s}\right)^2\right)^{3/2}}, \qquad (3)$$

where $\phi_{si}$ represents the average solid fraction across the bed at a certain height and at a given time interval ($i$), $\overline{\phi_s}$ represents the average of all the cross-sectional average solid fraction values and $N$ is the total number of measurements taken. Thus $\overline{\phi_s}$ can be expressed as

$$\overline{\phi_s} = \left(\sum_{i=1}^{N}\phi_{si}\right)/N. \qquad (4)$$

The skewness of a sample is a measure of the asymmetry of the sample. The skewness of a sample can be positive, negative or undefined. If the skewness of a sample is negative it indicates that the sample distribution had a longer 'tail' on the left side of the distribution. This kind of distribution is also called *left*-skewed (Scheffé 1959). This implies that the bulk of the values in the probability density function lies to the right of the distribution, including the median. The concept of skewness is illustrated in Figure 3 with two schematic probability density functions. The median is the midpoint of a distribution separating the low and high values of the distribution and will be indicated by $\overline{\tilde{\phi}_s}$. For a positive skewness value the opposite is true and the sample distribution will have a longer 'tail' on the right side of the median and thus the bulk of the values in the distribution

will be on the left side of the distribution. This distribution is called *right*-skewed and the mean will be on the right side of the median.
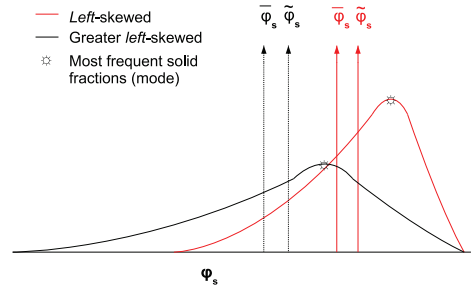


Figure 3: Schematic figure depicting two left-skewed distributions with different degrees of skewness. The mean of the distribution is represented by $\overline{\phi_s}$ and the median is indicated by $\overline{\tilde{\phi}_s}$.

Another useful tool in data analysis is the kurtosis of a sample. For a sample of $N$ values the **sample excess kurtosis** ($SEK$) can be defined as

$$SEK = \frac{\frac{1}{N}\sum_{i=1}^{N}\left(\phi_{si} - \overline{\phi_s}\right)^4}{\left(\frac{1}{N}\sum_{i=1}^{N}\left(\phi_{si} - \overline{\phi_s}\right)^2\right)^2} - 3, \qquad (5)$$

with the same variable definitions described in equation (3). This definition of the kurtosis is known as the *excess kurtosis* where the '*minus 3*' is added to make the kurtosis of a normal distribution equal to zero. One of the best ways to describe the kurtosis of a distribution is probably to refer to it as the '*peakedness*' or inversely

4

the '*flatness*' about the mean of a distribution (Lin and Wey 2004).

Distributions that has a excess kurtosis value of zero is called **mesokurtic**. A trivial example of such a distribution is the normal distribution. Next a distribution with a positive excess kurtosis value is called **leptokurtic**. This would typically be a distribution with more extreme peaks and thus not a generally 'flat' distribution. A distribution with a negative excess kurtosis is called **platykurtic** and is typical of a visually 'flat' distribution with almost no extreme deviations in the distribution (Scheffé 1959). In Figure 4 a schematic illustration is given to explain the concept of kurtosis.
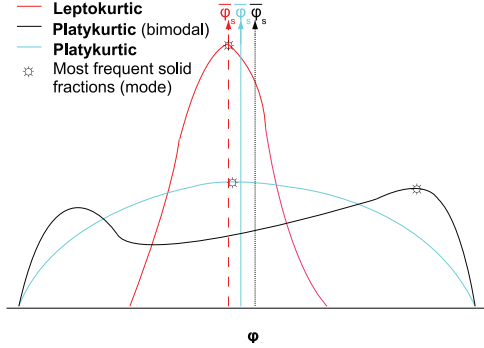


Figure 4: Schematic figure depicting the concept of kurtosis via three different probability density functions. The average of the distribution is represented by $\bar{\phi}_s$.

## 4. Results and discussion

To investigate the fluidization quality, the skewness and excess kurtosis of the four particle mixtures were investigated. The measurements were taken at two different bed heights, the one measuring plan was at a height of $H_m/D = 1.5$ and the other at $H_m/D = 2.8$, as mentioned in Section 2.1. In Figure 5 the skewness values are given for each of the four particle size distributions at $H_m/D = 1.5$. All of the powders had decreasing skewness values as the superficial velocity increased. The different particle groups are also easy to distinguish (as illustrated in Figure 5). The Geldart B particles had approximately linear decreasing skewness values while the Geldart D particles had more of a quadratic behaviour. Lin and Wey (2004) also used statistical methods to analyse pressure measurements in a
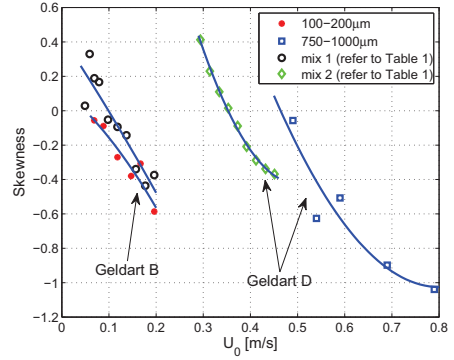


Figure 5: Skewness values as a function of the superficial velocity, $U_0$, at $H_m/D = 1.5$. Based on the probability density function of average solid fraction values recorded with a ECT tomograph.

fluidized bed. According to Lin and Wey (2004) an increasing skewness indicates that multiple small bubbles are present at the particular measuring height. Numerous small bubbles are desirable in a bubbling fluidized bed as it cause more efficient mixing of solids and better mass transfer properties than too larger bubbles (Saxena et al. 1993). The decreasing skewness with increasing superficial velocity (given in Figure 5) thus indicates that the bubbles has a long enough residence time in the bed to coalesce into larger bubbles at $H_m/D = 1.5$ (Lin and Wey 2004). In both particle groups the powders with the widest particle size distributions produced generally higher skewness values (*mix 1* and *mix 2* produced the widest particle size distributions). At a height of $H_m/D = 1.5$ the wide particle size distribution thus creates a bed that can be characterised by smaller bubbles compared to that of the narrower particle size distributions. When the skewness values go from positive to negative it indicates that the bubbling bed has transferred from micro- to macro-structures (Azizpour et al. 2011). This also explains why the powders containing the smaller particles have higher skewness values. The finer structures are more important in the finer powders leading to higher skewness values (Azizpour et al. 2011).

Generally Lin and Wey (2004) stated that the fluidization index increases with an increase in superficial velocity and therefore the quality of fluidization decreases with an increase of the superficial velocity. When the fluidization index becomes too large it is an indication of the onset of the slugging regime (Lin and Wey

2004). Hence a decreasing skewness is an indication of a progressively decreasing fluidization quality and the introduction of small particles (and thus wide particle size distribution) increases the fluidization quality. The positive attributes of small particles in a particle size distribution was also noted by Kunii and Levenspiel (1991). They stated that the quality of fluidization can be spectacularly improved by adding a small amount of small particles to act as lubricant (Kunii and Levenspiel 1991).

In Figure 6 the same data is presented as in Figure 5 but as a function of a dimensionless coefficient. The di-
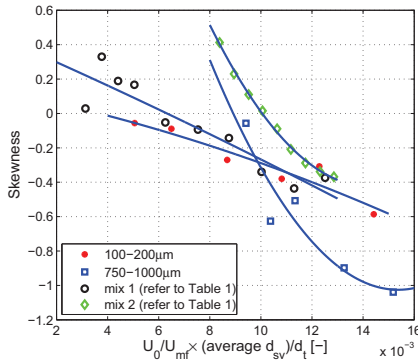


Figure 6: Skewness values as a function of the dimensionless coefficient, $U_0/U_{mf} \times \overline{d}_{sv}/d_t$, at $H_m/D = 1.5$. Based on the probability density function of average solid fraction values recorded with a ECT tomograph.

mensionless coefficient used in the present study is the product of the fluidization number, $U_0/U_{mf}$, and the ratio of the surface-volume mean diameter and the tower diameter, $\overline{d}_{sv}/d_t$. The dimensionless coefficient takes into account the mean particle size as small particles with a wide size distribution can be fluidized in a wider range of gas flow rates (Kunii and Levenspiel 1991). Thus to account for this phenomena and to view the statistical values on a more convenient way, this coefficient will be used in the remainder of the study. From Figure 6 it can also be observed that the $750 - 1000\mu m$ powder produced the lowest skewness values as the superficial velocity was increased. This powder was therefore clearly prone to slugging and spouting and thus bad fluidization quality. This could be expected for large particles of a narrow size distribution (Kunii and Levenspiel 1991). The influence of the small particles in the *mix 2* powder can also be observe in Figure 6 as it produced larger skewness values than when just the $750 - 1000\mu m$

powder was used. Azizpour et al. (2011) did experiments with acoustic signals and pressure measurements in fluidized beds filled with sand. They stated that the skewness will decrease as the average particle size is increased (Azizpour et al. 2011). This is also confirmed for the Geldart D particles size distributions in Figure 6. Generally, adding small particles seems to increase the skewness values.

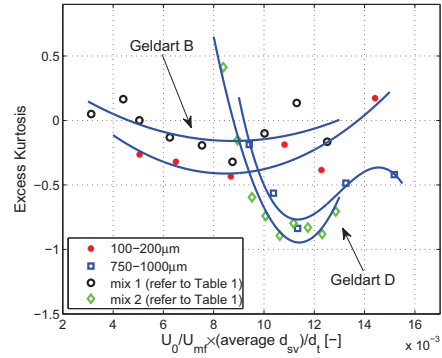In Figure 7 the excess kurtosis values are given at $H_m/D = 1.5$. Azizpour et al. (2011) stated that the



Figure 7: Excess kurtosis values as a function of the dimensionless coefficient, $U_0/U_{mf} \times \overline{d}_{sv}/d_t$, at $H_m/D = 1.5$. Based on the probability density function of average solid fraction values recorded with a ECT tomograph.

kurtosis of pressure fluctuation measurements reached a minimum against the superficial gas velocity and that this minimum occurs at higher superficial velocities for larger particles. Generally this behaviour is also observed in Figure 7 as the difference between Geldart B and D particles can clearly be noticed. The different Geldart groups behave differently. The Geldart B powders had a flat curve while the Geldart D particles had a clear minimum point. According to Azizpour et al. (2011) this minimum point in the kurtosis values is an indication of the change of the meso-structure of the bed and is not necessarily an indication of regime transition.

As mentioned before, Lin and Wey (2004) stated that decreasing skewness values mainly occurs higher up in a fluidized bed when the bubbles have a long enough residence time in the bed to coalesce and form larger bubbles and thus large pressure fluctuations. With the ECT average solid fraction measurements, large average solid fraction fluctuations are also an indication of large bubbles. Because of the decreasing skewness behaviour (shown in Figure 5 and 6) the minimum kurtosis

values observed in Figure 7 might indicate the onset of the slugging regime.

In Figure 8 the skewness values of the probability density function at $H_m/D = 2.8$ is provided. At
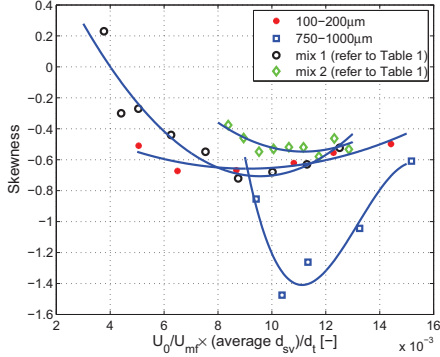


Figure 8: Skewness values as a function of the dimensionless coefficient, $U_0/U_{mf} \times \overline{d}_{sv}/d_t$, at $H_m/D = 2.8$. Based on the probability density function of average solid fraction values recorded with a ECT tomograph.

$H_m/D = 2.8$ the bubbles have had sufficient residence time in the bed to coalesce and form large bubbles. All of the investigated particle size distributions indicated a minimum skewness value at different superficial velocities. When the skewness values go from decreasing to increasing the bed must have reached the maximum bubble size as the variety of bubbles are increasing (Lin and Wey 2004). The coalescence and break down of bubbles are occurring simultaneously according Lin and Wey (2004), causing the skewness to increase again.

The influence of small particles are once again illustrated by the Geldart D particles in Figure 8. The skewness values of *mix 2* is much larger than just the $750 - 1000\mu m$ size distribution indicating better quality fluidization in the powder mixed with small particles.

In Figure 9 the excess kurtosis values at $H_m/D = 2.8$ is given. Figure 8 and 9 show that the values of skewness and kurtosis change inversely for three of the powders. The results given by Lin and Wey (2004), obtained with a Gaussian distribution with $\overline{d}_{sv} = 719\mu m$, also indicated that the kurtosis and skewness values (of pressure measurements) changed inversely. The excess kurtosis values of the *mix 2* powder was the only powder that had nearly the same trend as its skewness values. The gradient at which the $750 - 1000\mu m$ powder decreases in kurtosis values with increasing superficial velocity values is the greatest of all the powders and might
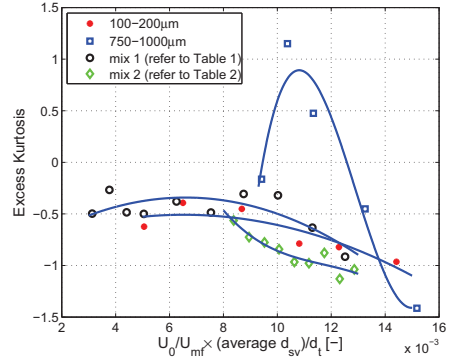


Figure 9: Excess kurtosis as a function of the dimensionless coefficient, $U_0/U_{mf} \times \overline{d}_{sv}/d_t$, at $H_m/D = 2.8$. Based on the probability density function of average solid fraction values recorded with a ECT tomograph.

indicate this Geldart D powder tends to slugging conditions. Again the *mix 2* and other finer powders indicate a less drastic variation in kurtosis values. These smooth changing kurtosis values might be an indication that the bed is still in the same regime. Saxena et al. (1993) stated that abrupt changes in skewness or kurtosis values indicate a regime change in the fluidized bed. Thus the small particles and the powders containing small particles perform better and are prone to better quality fluidization. This effect of small particles have been noted in literature before, where the introduction of small particles had the general effect of smaller bubbles in a bubbling fluidized bed (Rautenbach et al. 2011, van Biljon et al. 2011).

### 4.1. Visual diagnosis and confirmation of fluidized bed hydrodynamics

In the present study the usefulness of the ECT tomograph as a diagnostic tool in fluidized bed has been illustrated. It was show that the ECT tomograph could produce the same statistical diagnosis other popular measuring techniques can deliver. One of the advantages of the ECT tomograph is the possibility to produce solid fraction maps of the content of the reactor in a non intrusive manner. These images aids in diagnosing a fluidized bed alongside other diagnostic techniques.

In Figure 10 and 12 an example is presented of possible ECT tomograms. These images are time stacked tomograms indicating the solid fraction variation through the center of the bed for the firsts 5 seconds of the particular experiments. In these tomograms the difference

in bubble activity of plane one and two is also illustrated for three superficial velocities.

In Figure 10 the tomograms of the $750 - 1000\mu m$ powder is provided. As the superficial velocity is increased the clear slugging behaviour can be noticed in both plans. These slugs had a tendency to collapse and in Figure 11 this is illustrated by viewing the cross-section of the tower through a collapsing slug. In Figure 11 the solid particles in the center of the slug indicate the roof of the slug collapsing through the gas slug. These collapsing slugs also provide a possible explanation for the increase of bubble variety noted in Figure 6.
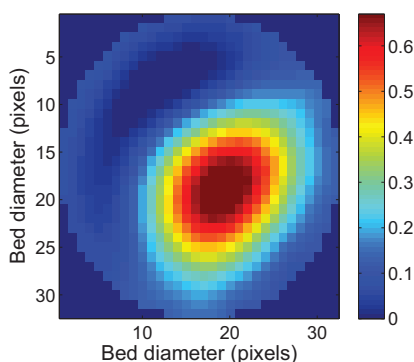


Figure 11: This is a cross-sectional image of the experimental tower at a superficial velocity of $0.79m/s$ at time $150cs$ of the $750$-$1000\mu m$ powder at plane one. Refer to Figure 10.

In Figure 12 the tomograms of the *mix 2* powder is presented. The *mix 2* powder was selected as it clearly illustrated the influence of small particles when compared with the bubble behaviour in Figure 10. The small particles cause the bed to be characterise by smaller bubbles as the superficial velocity is increased together with a lowering of the minimum fluidization velocity. Previous studies also indicated that the small particles, in a particle size distribution, have the dominant effect on the minimum fluidization velocity (Jayarathna and Halvorsen 2009). From these results it is clear that small particles has a important influence on the overall bed hydrodynamics.

## 5. Conclusion

In the present study the usefulness of an ECT tomograph as a diagnostic tool in a fluidized bed was illustrated. Using statistical methods the quality of fluidization of a fluidized bed was assessed. Using these statistical methods the ECT tomograph proved to be equally effective at diagnosing the quality of fluidization compared to other popular measurement techniques used in industry. These methods include temperature probes, pressure probes and acoustic or vibration measurements.

The ECT tomograph together with the statistical analysis was employed to investigate the influence of small particles on the hydrodynamics of a fluidized bed. It was found that small particles had the general effect of smaller bubbles and better quality fluidization. These observations were also confirmed when compare with tomograms created from the ECT data. ECT thus provides an added advantage, above some other measurement techniques, by providing a non intrusive view of the flow behaviour alongside the other diagnostic techniques.

## References

(2003). *PTL300-TP-G ECT system, Operation manual*. Process tomography Ltd., 86 Water Lane, Wilmslow, Cheshire. SK9 5BB, UK.

Azizpour, H., Sotudeh-Gharebagh, R., Zarghami, R., Abbasi, M., Mostoufi, N., and Mahjoob, M. (2011). Characterization of gas-solid fluidized bed hydrodynamics by vibration signal analysis. *International Journal of Multiphase Flow*, 37:788–793.

Jayarathna, C. and Halvorsen, B. M. (2009). Experimental and computational study of particle minimum fluidization velocity and bed expansion in a bubbling fluidized bed. Copenhagen, Denmark. International Conference of Scandinavian Simulation Society.

Kunii, D. and Levenspiel, O. (1991). *Fluidization Engineering*. Butterworth-Heinemann.

Lin, C. and Wey, M. Y. (2004). Statistical and power spectral analysis of quality of fluidization for different particle size distributions at high temperature. *Advanced Powder Technology*, 15(1):79–96.

Loser, T., Petritsch, G., and Mewes, D. (1999). Investigation of the two-phase countercurrent flow in structured packings using capacitance tomography. In *1st World Congress on Industrial Process Tomography*, pages 354–361, Greater Manchester.

Makkawi, Y. T. and Wright, P. C. (2002). Fluidization regimes in a conventional fluidized bed characterized by means of electrical capacitance tomography. *Chemical Engineering Science*, 57:2411–2437.

Makkawi, Y. T. and Wright, P. C. (2004). Electrical capacitance tomography for conventional fluidized bed measurements-remarks on the measuring technique. *Powder Technology*, 148:142–157.

McKeen, T. R. and Pugsley, T. S. (2002). The influence of permittivity models on the phantom images obtained from electrical capacitance tomography. *Measurement Science and technology*, 13:1822–1830.

Patel, A., Waje, S., Thorat, B., and Mujumdar, A. (2008). Tomographic diagnosis of gas maldistribution in gas-solid fluidized beds. *Powder Technology*, 185:239–250.

Pugsley, T., Tanfara, H., Malcus, S., Cui, H., Chaouki, J., and Winters, C. (2003). Verification of fluidized bed electrical capacitance tomography measurements with a fibre probe. *Chemical Engineering Science*, 58:3923–3934.

Rautenbach, C., Melaaen, M. C., and Halvorsen, B. M. (2011). Investigating the influence of fines in fluidized bed reactors using 3d ect
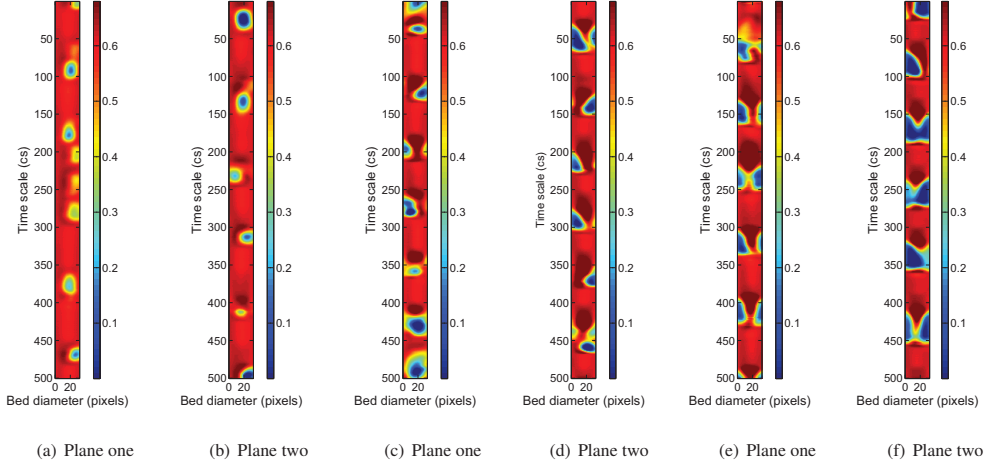
(a) Plane one     (b) Plane two     (c) Plane one     (d) Plane two     (e) Plane one     (f) Plane two

Figure 10: The time staked images are given for the first $5s$ of each velocity using the 750-1000$\mu m$ powder. The samples were at (a),(b) 0.5$m/s$, (c),(d) 0.64$m/s$ and (e),(f) 0.79$m/s$ respectively.
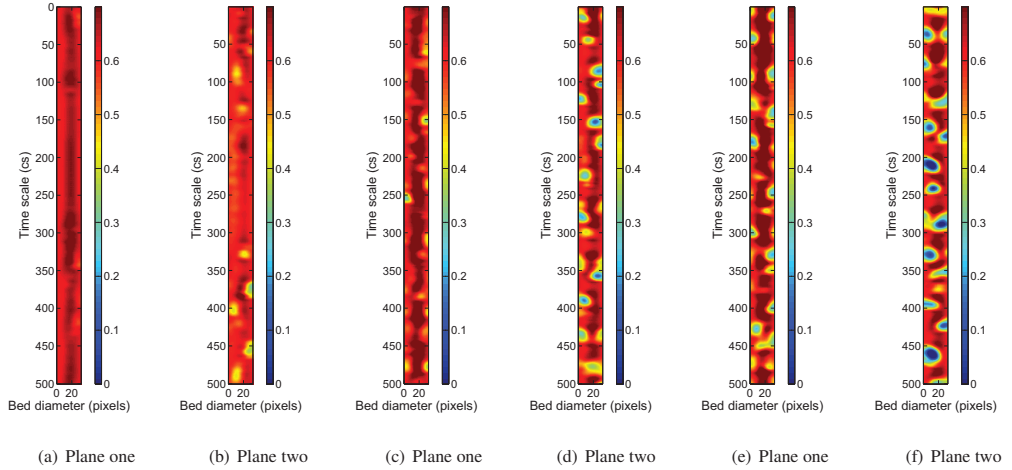


(a) Plane one     (b) Plane two     (c) Plane one     (d) Plane two     (e) Plane one     (f) Plane two

Figure 12: The time staked images are given for the first 5 seconds of each velocity using the mixture of the 100-200 $\mu m$, 400-600 $\mu m$ and 750-1000$\mu m$ powder (*mix 2*). In these experiments the superficial velocity was reduced for each measurement instead of increasing steps in the superficial velocity. The samples were at (a),(b) 0.29 m/s, (c),(d) 0.31 m/s and (e),(f) 0.35 m/s respectively.

9

images. In Mammoli, A. A. and Brebbia, C. A., editors, *Computational Methods in Multiphase flow VI*, pages 141–151, Ashurst Lodge, Ashurst, Southampton SO40 7AA, UK. Wessex Institute of Technology, WIT-Press.

Salehi-Nik, N., Sotudeh-Gharebagh, R., Mostoufi, N., Zarghami, R., and Mahjoob, M. (2009). Determination of hydrodynamic behaviour of gas-solid fluidized beds using statistical analysis of acoustic emissions. *International Journal of Multiphase flow*, 35:1011–1016.

Saxena, S., Rao, N., and Tanjore, V. (1993). Diagnostic procedures for establishing the quality of fluidization of gas-solid systems. *Experimental Thermal and Fluid Science*, 6:56–73.

Scheffé, H. (1959). *The analysis of variance*. John Wiley and Sons, Inc., New York.

Sharma, R., Karki, S., and Masoudi, N. (2010). Electrical capacitance tomography for characterising bubbles in fluidized beds. Master's thesis, Telemark University College, Porsgrunn, Norway.

van Biljon, C., du Toit, E., and Nicol, W. (2011). Effect of fines on the bubble properties in a two-dimensional fluidized bed by digital image analysis. In Luckos, A. and den Hoed, P., editors, *Industrial Fluidization South Africa, Supporting sustainable strategies*, pages 267–275, Chamber of Mines Building, 5 Hollard Street, Johannesburg 2017, South Africa. Southern African Institute of Mining and Metallurgy.

Warsito, W. and Fan, L.-S. (2005). Dynamics of spiral bubble plume motion in the entrance region of bubble columns and three-phase fluidized beds using 3d ect. *Chemical Engineering Science*, 60:6073–6084.

# Paper I

# Investigation of flow behaviour in biomass gasifier using Electrical Capacitance Tomography (ECT) and pressure sensors.

# Investigation of flow behaviour in biomass gasifier using Electrical Capacitance Tomography (ECT) and pressure sensors

R.K.Thapa[1], C.Rautenbach[1] and B.M.Halvorsen[1]

1. Department of Process, Energy and Environmental Technology, Telemark University College, Norway.

**Abstract:**

The particles in a biomass gasifier are mainly a mixture of wood chips, char particles and bed material. The char-wood particles have a significant lower density than the bed material, and also a wider range of particle sizes and larger mean particle diameter. The difference in particle properties may cause segregation and thereby influence on the fluidization properties and the flow behavior in the bed. The aim of this work is to study the fluidization properties in cold fluidized bed with different mixtures of particles. ZrO and plastic particles with a density ratio of 6, are used in the experiments to simulate the bed material and the char-wood particles in a biomass gasifier. Experiments are performed in cylindrical beds with uniform air distribution. The fluidization properties are studied using pressure sensors and Electrical Capacitance Tomography (ECT). The ECT system is a non-intrusive measurement system and is a suitable method for monitoring the internal flow behavior of fluidized bed. The experimental results show that the minimum fluidization velocities very much depend on the particle composition in the bed. The fluidization velocity reaches a maximum when 20% plastic particles are added to the ZrO powder and decreases again when the fraction of plastic beads are further increased. The theoretical minimum fluidization velocities for the different mixtures agree well with the experimental data. The standard deviations of the pressure and the ECT measurements showed that the fluidization velocities are higher in the lower part than in the higher part of the bed. This observation is more significant in the mixtures with high fraction of plastic particles. This indicates that the plastic particles moves upward in the bed and that mainly ZrO particles are present in the lower part of the bed. This is also visually observed during the experiments. Segregation can give low degree of particle motion in parts of the bed. Investigation of fluidization behavior of the different mixtures in this study may be useful as an initial step of analyzing the complex system of a bubbling fluidized bed gasifier.

## 1. Introduction

Production of heat and power based on biomass from forestry has during the last decade become a very important technology. Gasification of biomass is a part of the process, and researchers have studied different types of fluidized bed reactors to find an optimal design. The efficiency of a fluidized bed reactor is highly dependent on the powder properties and the flow conditions which also control the mixing of the bed. Particle density, particle sizes, range of particle sizes and superficial gas velocity are influencing on the flow behavior, mixing and segregation. The particles in a biomass gasification reactor are a mixture of wood chips, char particles and bed material. The feed to the gasifier consists of wood chips with a size of 1-5 cm and a large variety of shapes. During the gasification the size of the wood chips decreases significantly from large wood chips fed to the reactor to unreacted char particles with a wide range of particle sizes. The wood chips and the char particles have a significant lower density than the bed material. The density difference may cause segregation and thereby influence on the fluidization properties and bubble activities. In addition the wood chips, the char and the bed material have a wide range of particle sizes. When the range of particles sizes is wide, the particles will have a tendency to segregate. Good mixing in the gasifier is important to secure significant heat transfer in the bed.

## 2. Concept and methodology

The aim of this work is to study the fluidization properties in a gasification reactor and to investigate how mixtures of different particle sizes and density influence on the fluidization properties. In a gasifier a typical temperature of the inlet steam is 400°C and the density is about 0.32 kg/m$^3$. The density of the bed material and the char/wood particles are about 2500 and 400-500 kg/m$^3$ respectively. In this study air with density 1.18 kg/m$^3$ is used as the fluidization gas. The density ratio air/steam is about 4, and the particle ratio should be about the same to be able to simulate the actual gasification reactor. ZrO with density 5850 kg/m$^3$ and plastic beads with density 964 kg/m$^3$ are used to simulate the bed material and the char/wood particles respectively. The density ratio of the particles used in the experiments is about the same as the density ratio of the bed material and the char/wood particles in a gasification reactor. The experiments are performed in fluidized beds with diameter 0.084 and 0.104 m. The experimental set up is presented in Fig. 1. Pressure sensors are used to measure flow behavior in the 0.084m bed, whereas Electrical Capacitance Tomography (ECT) is the measurement system used in the 0.104 m bed. Fig. 2 shows a sketch of the bed with pressure sensors. The sensors used in this study are named p2, p4, p5 and p6 and are located 0.03, 0.23, 0.33 and 0.43 m above the air distributor.

The ECT system is used to investigate the fluidization properties and the bubble activity in the bed. The ECT system is a non-intrusive measurement system and is a suitable method for monitoring the internal flow behavior of fluidized beds. The sensors are placed on the outside of the non-conductive experimental bed and the sensors are measuring flow behavior in two planes. The fluidization properties have been studied by using ECT in combination with a reconstruction program developed at Telemark University College [1]. The recon-struction program creates images of the fluidized bed reactor and the flow properties like minimum fluidization velocity and bubble activity can be studied. A sketch of the ECT system is presented in Fig. 3. The figure also shows a cross sectional view of the ECT sensor together with a cross sectional image. The sensors are located at height 0.156 m (plane1) and 0.286 m (plane2) above the air distributor. The ECT-system is described in detail in [1].
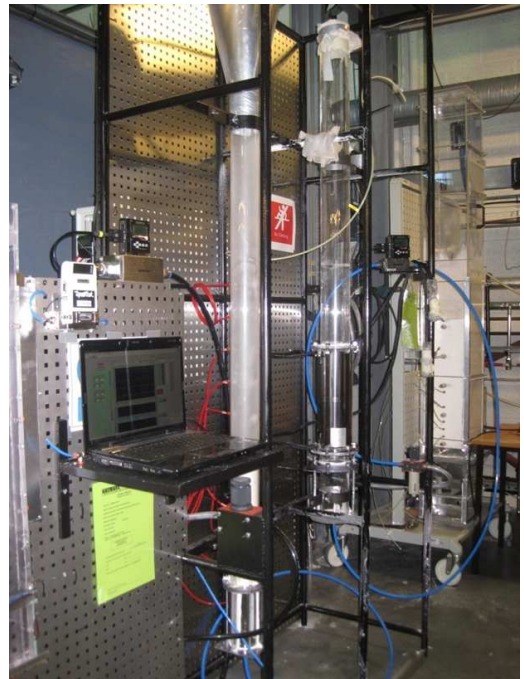


**Fig. 1: Experimental set-up. Fluidized bed with pressure reduction valve, digital flow controller, pressure sensors.**
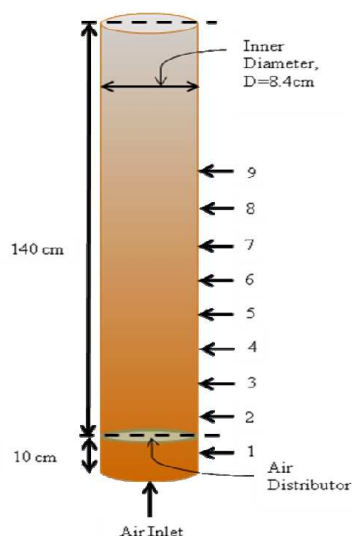
**Fig. 2: Sketch of 0.084 m bed with pressure sensors.**
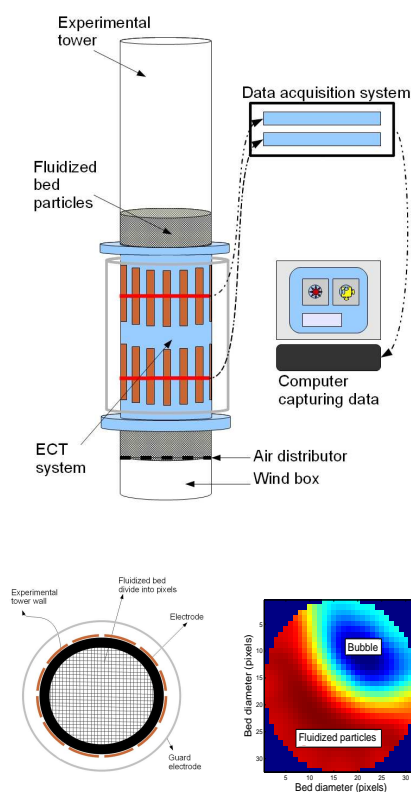




**Fig. 3: Sketch of the 0.104 m bed with ECT system.**

# 3. Results and discussion

Inside the gasifier there is simultaneous existence of unreacted wood chips, reacting wood chips, char particles and bed material having a large range of particle sizes, shape and density. Consequently the particle composition is varying along the bed height which makes it difficult to predict the fluidization behavior of the gasifier in an accurate way using a cold bed. To study the mixing and segregation tendency in a fluidized bed gasifier, ZrO and plastic beads with density ratio 6 are used. In a gasifier the particle size distribution is wide, from large wood chips (1-5 cm), all sizes of char particles and the bed material with particle size about 400-600 µm. The plastic beads with large particle sizes and wide shape distribution resemble the average particle size and shape of the char inside gasifier. ZrO has about the same particle size distribution as the bed material in a gasifier. Investigation of fluidization behavior of mixtures of the two types of particles with different particle size and shape as well as density can only be an initial step of an analysis of the complex system of a bubbling fluidized bed gasifier. Air is used as fluidization gas in the experiments whereas steam at 400ºC is used in a real gasifier. The air/steam ratio is about 4, and to get the correct picture of the fluidization conditions in the gasifier based on experiments in cold bed, the particles used in the experiments should have a density 4 times the particles in the hot reactor. Particles with this high density were not available, and lighter particles are therefore used. However the density ratio bed material/char-wood particles are maintained. The experiments are performed with pure ZrO and plastic particles, and with different mixtures of these two types of particles. The

experimental test matrix is presented in Tab. 1.

The pressure drop as a function of superficial velocity for pure ZrO and plastic beads are shown in Fig. 4 and 5 respectively. The analysis of the experimental results shows that the minimum fluidization velocities ($U_{mf}$) for ZrO and plastic beads are 0.67 m/s and 0.85 m/s respectively. The higher $U_{mf}$ for the plastic beads is due to the large particle size and high void fraction.

| Particle | Mean particle size [μm] | Initial bulk density [kg/m³] | Initial void fraction |
|---|---|---|---|
| ZrO | 709 | 3857 | 0.34 |
| ZrO+10% plastic | 709 /3500 | 3680 | 0.31 |
| ZrO+20% plastic | 709 /3500 | 3488 | 0.28 |
| ZrO+30% plastic | 709 /3500 | 3355 | 0.25 |
| ZrO+40% plastic | 709 /3500 | 3237 | 0.23 |
| Plastic beads | 3500 | 564 | 0.42 |

**Tab. 1: Test matrix**
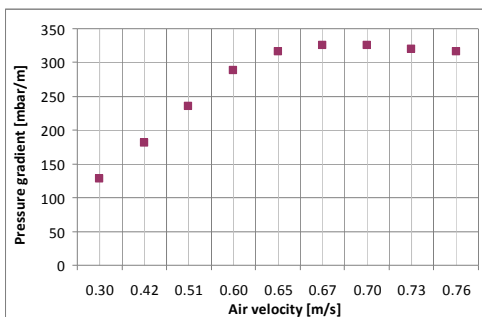


**Fig. 4: Pressure gradient as a function of superficial air velocity. ZrO**
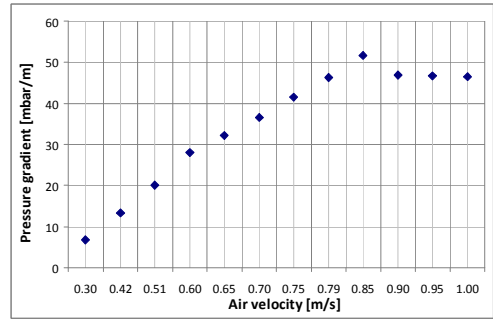


**Fig. 5: Pressure gradient as a function of superficial air velocity. Plastic particles.**

Fig. 6 show the pressure drop as a function of superficial velocity for ZrO and four different mixtures of ZrO and plastic. The pressure drop is the average pressure drop in the bed. When mixing plastic and ZrO particles the initial void fraction changes. The minimum fluidization velocity and the pressure drop (dp/dx) are strongly dependent on the void fraction in the bed. $U_{mf}$ for pure ZrO is about 0.67 m/s. As can be seen from Fig. 6, $U_{mf}$ increases to about 0.75 m/s when 10 vol% plastic particles are mixed with the ZrO, and increases further to 0.77 m/s when the vol% of plastic beads is increased to 20%. When the vol% of plastic beads are increased to 30%, $U_{mf}$ decreases to 0.70 m/s and the mixture with 40 vol% plastic gives $U_{mf}$ 0.65m/s which is lower than $U_{mf}$ for the pure ZrO. The pressure drop (dp/dx) in the bed is about 350 mbar/m for the mixtures with 10, 20 and 30 vol% plastic beads, whereas dp/dx is about 330 mbar/m for pure ZrO and the mixture with 40% plastic beads.
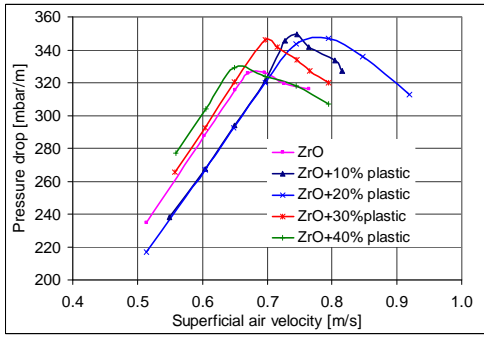
**Fig. 6: Pressure gradient as a function of superficial air velocity. ZrO and different mixtures of ZrO and plastic.**
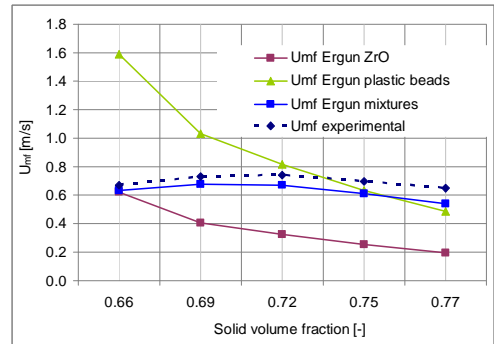
The minimum fluidization velocity is a function of particle size, particle shape, particle density and void fraction. The minimum fluidization velocity can be developed from the buoyant-equals-drag balance. Using Ergun equation, the theoretical minimum fluidization velocity is given by [2,3]:

$$U_{mf} = \frac{(\Phi \cdot d_p)^2 \Delta\rho \cdot g}{\mu} \cdot \frac{\varepsilon_{mf}^{\ 3}}{1-\varepsilon_{mf}} \qquad (1)$$

where $\Phi$ is the shape factor, $\varepsilon$ is the void fraction, $d_p$ is the particle diameter, $\Delta\rho$ is the particle-gas density difference and $\mu$ is the gas viscosity. Ergun equation is used to investigate the effect of the different parameters on the fluidization properties. The theoretical minimum fluidization velocities are calculated for the pure plastic and ZrO powders and for the different mixtures of the two types of powders. The initial void fractions in Tab. 1 are used in the calculations of the mixtures.

The comparison is shown in Fig. 7. The calculations are based on the average particle density and average particle size and shape. The pure ZrO and plastic particles show decreasing theoretical $U_{mf}$ with increasing solid volume fraction. The deviation between the two curves decreases with increasing solid volume fraction. The calculated $U_{mf}$ for mixtures

(ZrO with 0, 10, 20, 30, 40 vol% plastic beads) shows the same tendency as the experiments by having a maximum $U_{mf}$ for mixture with 10 – 20 % plastic particles. The experimental $U_{mf}$ is higher than the theoretical. The deviation between experimental and theoretical results increases from 6% to 17% with increasing vol% of plastic beads. The non-linear behavior of the $U_{mf}$ as a function of solid volume fraction may be due to the significance of the different particle properties in the mixtures. Higher fraction of plastic particles gives decreasing void fraction, particle density and average shape factor in the mixture. These three parameters contribute to decrease the $U_{mf}$ when the fraction of plastic particles is increased. The mean particle diameter increases with increasing fraction of plastic particles and contribute to increase the fluidization velocity. When the increase in $d_p$ is more dominant than the decrease of $\varepsilon$, $\Delta\rho$ and $\Phi$, the $U_{mf}$ increases. The $U_{mf}$ decreases again when the changes in $\varepsilon$, $\Delta\rho$ and $\Phi$ become more significant.



**Fig. 7: Comparison of experimental and calculated minimum fluidization velocity as a function of solid volume fraction.**

In addition to investigate the changes in minimum fluidization velocity with the changes in vol% of large particles with low density, the aim of this study is also to investigate the segregation tendencies for the different mixtures. The pure ZrO

and plastic powders have both a rather narrow particle size distribution, and segregation is not expected to occur in those experiments. The segregation tendency is checked by plotting the pressure standard deviation at different heights of the bed. The standard deviation is zero until the bed starts to fluidize, and for the pure powders it was found that the fluidization occurred at the same velocity at all levels in the bed. To investigate the fluidization velocity and the segregation tendencies of the different mixtures of particles, the pressure standard deviation at the bottom and the top of the bed is plotted. Fig. 8 and 9 show the results from the experiments with 10 and 20 vol% plastic particles. No significant deviation of fluidization velocity at different levels of the bed can be observed from the pressure standard deviation for these two cases. However picture from experiments with 10 vol% plastic, presented in Fig. 10, shows that the plastic particles move to the top of the bed when the velocity is increased above the minimum fluidization velocity. This segregation tendency was also observed at velocities below minimum fluidization.
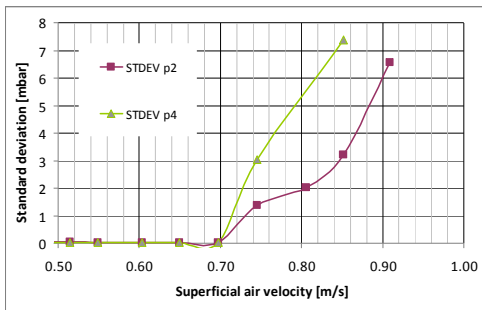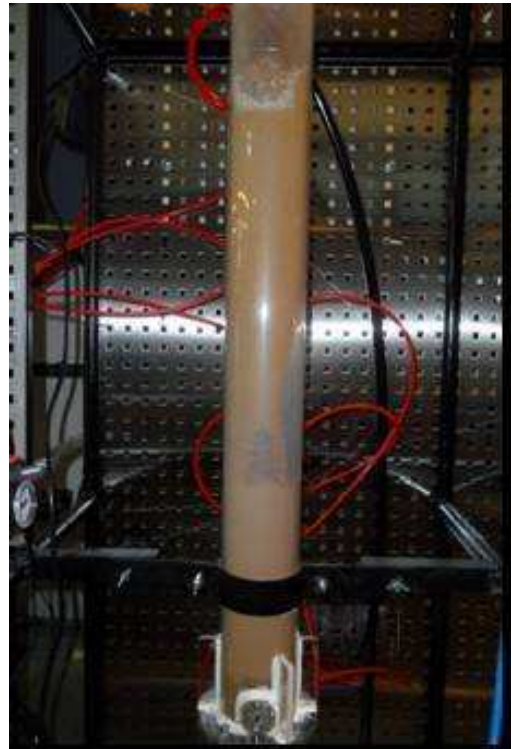


**Fig. 8: Pressure standard deviation as a function of superficial velocity at two heights. ZrO with 10% plastic.**
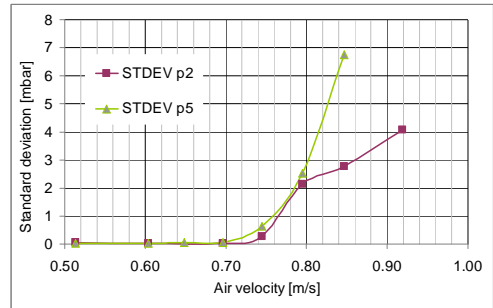


**Fig. 9: Pressure standard deviation as a function of superficial velocity at two heights. ZrO with 20% plastic.**

In the case of air velocity much higher than minimum fluidization, the mixing occurs mainly in the upper part of the bed.



**Fig. 10: Segregation. ZrO+10% plastic beads**

Fig. 11 and 12 show the pressure standard deviation for the 30 and 40 vol% mixtures respectively. For these cases the minimum fluidization velocity decreases from the bottom to the top of the bed.

According to the pressure standard deviation for the 30% mixture, the upper part of the bed starts to fluidize at superficial velocity 0.65 m/s, whereas the bottom part starts to fluidize at 0.70 m/s. This indicates that the concentration of plastic particles is highest in the upper part of the bed. The mixture with 40% plastic beads shows the same tendency. The fluidization velocities are 0.61 m/s in the upper part and 0.65 m/s in the lower part of the bed. The $U_{mf}$ in the bottom part is close to $U_{mf}$ for pure ZrO. This indicates that the concentration of ZrO is high in the lower part of the bed and that the plastic particles tend to move upwards and are well mixed with ZrO in the upper part of the bed.
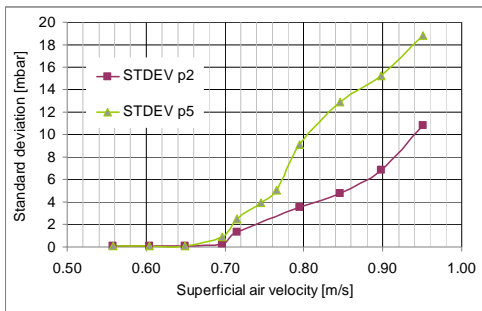


**Fig. 11: Pressure standard deviation as a function of superficial velocity at two heights. ZrO with 30% plastic.**
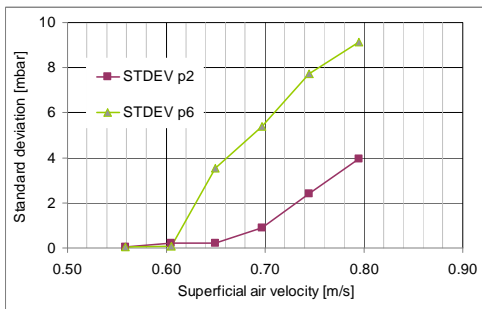


**Fig. 12: Pressure standard deviation as a function of superficial velocity at two heights. ZrO with 40% plastic.**

The experimental results from all the mixtures show a significant deviation between the pressure standard deviation in the upper and lower part of the bed at velocities above $U_{mf}$. This indicates that the bubble activity increases with height in the bed.

Experiments with 10 and 20 vol% plastic beads were also performed using ECT (Electric Capacitance Tomography). The ECT system produces signals that are converted to solid volume fraction at two levels in the bed. The measuring planes are located 0.156 m and 0.286 m above the air distributor. The solid volume fraction standard deviations for the two cases are presented in Fig. 13. For the 10% mixture ECT gives slightly higher $U_{mf}$ in the lower part than in the upper part of the bed. The velocities are about 0.75 and 0.74 m/s. According to the ECT results for the 20% mixture, the $U_{mf}$ increases from 0.80 m/s at the upper plane to 0.85 m/s in the lower plane. These results deviate from the results measured with pressure sensors. The deviations may be due to variations in segregation in the different experimental series. The different bed diameter of the ECT (0.104 m) and the pressure measurement (0.084 m) systems may also influence somewhat on the results. The fluidization properties in the smallest bed may be influenced by the wall effects. The tendency for all the mixtures is that segregation will occur when larger particles with low density are mixed with smaller particles with high density. Segregation may cause low degree of particle motion in the lower part of the bed.

Fig. 14, 15 and 16 show the bubble activity as a function of time at superficial velocity 0.8, 0.9 and 1 m/s respectively. The figures show the bubble activity for the 10% mixture at the two ECT planes. In Fig. 14 the superficial velocity is slightly above the $U_{mf}$, and it can be seen

that at plane1 no bubbles have appeared whereas at plane2 a few small bubbles are observed. Fig. 15 and 16 show that the bubble frequency and bubble sizes increase significantly with gas velocity. It is also obvious that the bubble activity changes significantly from plane1 to plane2. This tendency can be observed for all the velocities. The analysis of the pressure measurements showed a similar variation in bubble activity from the lower to the upper part of the bed.
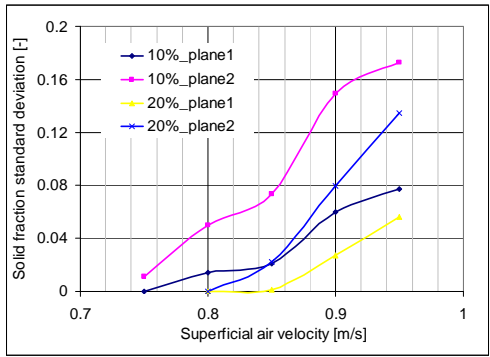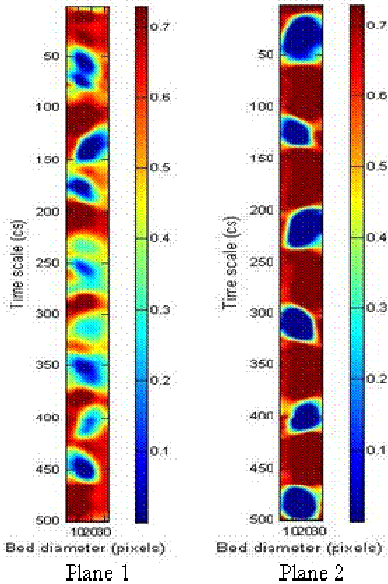


**Fig. 13: Comparison of minimum fluidization velocities for different mixtures**
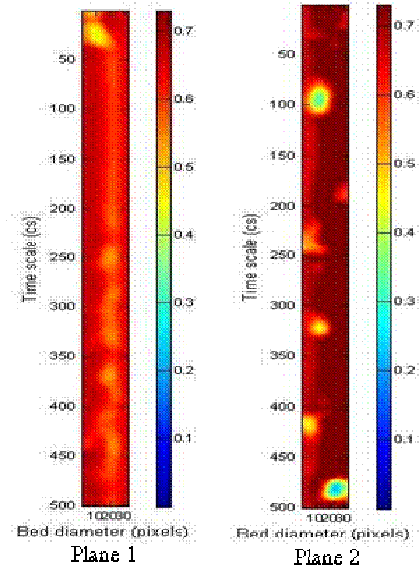


**Fig. 14: Bubble distribution. Air velocity 0.8 m/s. ZrO+10% plastic beads**
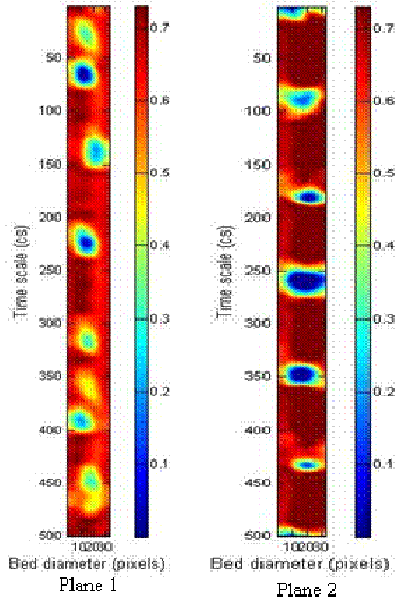


**Fig. 15: Bubble distribution. Air velocity 0.9 m/s. ZrO+10% plastic beads**



**Fig. 16: Bubble distribution. Air velocity 1 m/s. ZrO+10% plastic beads**

The experimental results obtained for ZrO and plastic beads can be used to predict the tendencies of flow behavior in a gasification process. In a bubbling

fluidized bed gasifier, the bed material is mixed continuously with char and wood particles of lower density and significantly higher mean particle size. The experimental data indicates that the mixing of char/wood with bed material depends on the fraction of char/wood particles. Char particle and wood chips have not only large range of particle size distribution but also large range of shape distribution. Experimental results show that the minimum fluidization velocity strongly depends on the sphericity of the particles as well. In order to make char and bed material well mixed inside the gasifier, the ratio of char particles to bed material should be rather high. Consequently this will give lower circulation of bed material. Good mixing promotes higher degree of heat transfer. The steam flow rate in a gasifier depends on the minimum fluidization velocity. Lower minimum fluidization velocity reduces the required steam flow rate. This secures less consumption of steam as fluidizing agent and prevents the possibility of unreacted steam in the product gas. That means that the moisture content in the product gas is reduced.

The experiments are performed in cylindrical fluidized bed with uniform diameter from bottom to top. A real bubbling fluidized bed gasifier has a coning design where the cross section area of the gasifier increases from bottom to top of the bed. The superficial gas velocity decreases with increasing diameter and consequently a suitable design of the gasifier can give uniform fluidization in the bed controlled by the inlet superficial gas velocity. According to the experimental results, bed materials with higher density remains on the bottom of the gasifier with lower cross sectional area whereas the mixture of bed material with char and wood particles with lower density are present mainly in

the upper part of the bed with higher cross section area. The different cross section area should balance fluidization behavior in the bed. Real fluidization behavior of a gasification reactor should be studied using an optimal design of the cold bed to investigate a more realistic behavior.

## 4. Conclusion

Experiments are performed with ZrO and plastic beads with density 5850 and 964 kg/m$^3$ respectively. These particles have about the same density ratio as the char/wood and bed material in a fluidized bed gasifier. The experimental results can therefore give an indication of how mixtures of particles with different densities and particle size and shape may influence on the flow behavior in an actual gasifier. The fluidization properties and segregation tendencies are investigated for the pure ZrO and plastic particles and for mixtures of ZrO and 10, 20, 30 and 40 vol% plastic particles. The flow behavior for the different cases is studied by using pressure sensors and Electrical Capacitance Tomography (ECT). Average pressure drop over the bed is used to determine the minimum fluidization velocities ($U_{mf}$) for the different cases. $U_{mf}$ is 0.85 and 0.67 m/s for pure plastic and ZrO particles respectively. Minimum fluidization velocity depends mainly on particle size, particle shape, particle density and void fraction. The plastic particles are rather large (2500-3500 µm), they have an irregular shape, low density and the initial void fraction is rather high (0.42). The ZrO powder consists of spherical particles with diameter 500-800 µm with high density and initial void fraction of 0.34. High density, high void fraction and large particles increase $U_{mf}$. The combination of the particle properties gives higher $U_{mf}$ for the plastic beads than for the ZrO

particles. The $U_{mf}$ for the mixtures with ZrO and 10, 20, 30 and 40 vol% plastic particles are 0.75 m/s, 0.77 m/s, 0.70 m/s and 0.65m/s respectively. The $U_{mf}$ has a maximum for the 20% mixture and decreases again with further increase in volume fraction of plastic. The theoretical $U_{mf}$ based on Ergun equation is calculated for the different mixtures. The theoretical $U_{mf}$ for the mixtures agrees well with the experimental results. The maximum $U_{mf}$ occurs for a mixture of about 20% plastic beads. Pressure standard deviation is calculated to investigate the segregation tendency for the different mixtures. The results show that 30 and 40% mixtures give higher fluidization velocity in the lower than in the higher part of the bed. This indicates that the plastic particles moves upward in the bed and that mainly ZrO particles are present in the lower part of the bed. This is also visually observed during the experiments. Experimental results from ECT show the same tendency of segregation also for the mixtures with lower content of plastic beads. The ECT gives somewhat higher $U_{mf}$ than the pressure sensors. All the experiments show that the bubble activity increases with height in the bed when the superficial velocity is increased above the $U_{mf.}$

## 5. References

[1] C. Rautenbach et al., Investigating the influence of fines in fluidized bed reactors using 3D ECT images, WIT Press, Multiphase Flow VI, (2011) (In Press)
[2] S. Ergun, Fluid flow through packed columns, Chemical Engineering Progress, **48** (2)**,** (1952) p 89-94
[3] S. Kunii, O. Levenspiel, Fluidization Engineering, Second Edition, (1991).